THERMODYNAMIC STUDIES IN LIQUID Fe-Nb-O, Fe-Al-O, Fe-Al-Mn-O SYSTEMS

THERMODYNAMIC STUDIES IN LIQUID Fe-Nb-O, Fe-Al-O, Fe-Al-Mn-O SYSTEMS USING SOLID ELECTROLYTES

By

Constantinos J. Stournaras, Dipl.Eng.

A Thesis

Submitted to tne School of Graduate Studies

in Partial Fulfilment of the Requirements

for the Degree

Doctor of Philosophy

McMaster University

January, 1977

©

DOCTOR OF PHILOSOPHY (1977) McMaster University

(Metallurgy) (Hamilton, Ontario)

TITLE: Thermodynamic studies in liquid Fe-Nb-O, Fe-Al-O, Fe-Al-Mn-O systems, using solid electrolytes.

AUTHOR: Constantinos J. Stournaras, Dipl.Eng.

(National Technical University of Athens, Greece)

SUPERVISOR: Professor D. A. R. Kay

NUMBER OF PAGES: (xvii), 183

ABSTRACT

A high temperature electrochemical technique has been developed, to continuously monitor the oxygen activity in iron based melts.

The electrochemical cell used, can be represented as:

$$Mo \left| Cr_{(s)}\text{-}Cr_2O_{3(s)} \right| \begin{matrix}\text{Calcia} \\ \text{stabilised} \\ \text{zirconia}\end{matrix} \left| Fe\text{-}M\text{-}O_{(\ell)} \right| \begin{matrix}Mo\text{-}ZrO_2 \\ \text{cermet}\end{matrix}, Mo$$

The electrolyte was in the form of a crucible to hold the metallic melt.

The standard free energy change for the reactions:

$$FeNb_2O_{6(s)} \rightleftarrows 2NbO_{2(s)} + Fe_{(\ell)} + \underline{2O}\ \text{lw/o}$$

$$FeAl_2O_{4(s)} \rightleftarrows Al_2O_{3(s)} + Fe_{(\ell)} + \underline{O}\ \text{lw/o}$$

and the influence of manganese content of the melt on the oxygen activity for the equilibrium:

$$(Fe_{1-x},Mn_x)O.Al_2O_{3(s)} \rightleftarrows Al_2O_{3(s)} + (1-x)Fe_{(\ell)} + x\underline{Mn}\ \text{lw/o} + \underline{O}\ \text{lw/o}$$

were determined using this technique at a temperature range of 1550 - 1600°C.

The results can be summarized as:

(a) $\Delta G^{\circ}_{T}[FeNb_2O_{6(s)} - NbO_{2(s)}] = 105870 - 42.64°T\ (\pm 600)$

cal/mole $FeNb_2O_6$

[1550°C - 1600°C]

(b) $\Delta G^{\circ}_{T}[FeAl_2O_{4(s)} - Al_2O_{3(s)}] = 49910 - 21.50\ T(\pm 300)$

cal/mole $FeAl_2O_4$

[1550°C - 1600°C]

(c) Increasing the manganese content in the melt decreases the value of $\log h_O$ in equilibrium with the transition reaction.

The nature of the deoxidation inclusions of the liquid systems Fe-Nb-O, Fe-Al-O and Fe-Al-Mn-O were studied by X-ray analysis and their morphology by scanning electron microscopy. In the Fe-Nb-O system the inclusions were identified as NbO_2 and $FeNb_2O_6$ and appeared to form agglomerates of small crystallites.

In the Fe-Al-O and Fe-Al-Mn-O the inclusions were identified as Al_2O_3 clusters along with $FeAl_2O_4$ or (Fe,Mn) Al_2O_4 respectively. The thermodynamic data obtained by the present technique are believed to be of high accuracy and the method significantly contributes in the studies of complex deoxidation systems at steelmaking temperatures.

An attempt was made to use the present electrochemical technique in studying the liquid Fe-Ti-O system at high oxygen potentials. Further research is suggested to fully resolve the results.

ACKNOWLEDGEMENTS

The author wishes to express his gratitude to Dr. D. A. R. Kay for his guidance and encouragement during the course of this study. Grateful acknowledgements are also due to Dr. A. McLean and Mr. T. Kitikawa from the University of Toronto for their help concerning the iodine etching technique used in this study.

The author would like to thank members of the staff and graduate students of McMaster Metallurgy Department who, through many discussions, contributed to the solution of various problems.

Special thanks are due to Dr. D. Ghosh and Mr. P. Apte for constructive criticism and assistance in developing the present electrochemical technique and to Mrs. M. Pope for fast and accurate typing of the thesis.

TABLE OF CONTENTS

CHAPTER		Page
I	INTRODUCTION	1
II	LITERATURE REVIEW	4
	2.1 Introduction	4
	A. Steel Deoxidation	5
	2.2 Deoxidation equilibria in Fe-M-O systems	5
	2.3 Determination of the transition points	8
	2.4 The binary Fe-O system	12
	2.5 Solubility minima of oxygen in liquid Fe-O-M alloys	14
	2.6 Inclusions in deoxidation	16
	B. Galvanic cell measurements using solid electrolytes	18
	2.7 Introduction	18
	2.8 Transport properties of solid oxide electrolytes	19
	2.9 Transference number measurements	22
	2.10 Solid electrolyte galvanic cells for thermodynamic and kinetic studies	23

CHAPTER			Page
		2.10.1 Equilibrium measurements	23
		2.10.2 Kinetic measurements	24
	2.11	The oxygen concentration cell	25
	2.12	Calcia stabilised zirconia as a solid electrolyte	29
	2.13	The Cr/Cr_2O_3 reference electrode	31
	C.	Deoxidation studies in the Fe-Nb-O, Fe-Al-O, Fe-Al-Mn-O and Fe-Ti-O systems	35
	2.14	Equilibrium in the Fe-Nb-O system	35
	2.15	The system Nb-O	40
	2.16	Equilibrium in the Fe-Al-O system	42
		2.16.1 Experimental determinations of the deoxidation "constant" $K'_{(2.64)}$	43
		2.16.2 Experimental determinations of the deoxidation constant $K_{(2.64)}$	47
		2.16.3 Experimental determinations of $K'_{(2.67)}$ and $K_{(2.67)}$	51
	2.17	The Al-O system	57
	2.18	The free energy of solution of aluminum	57
	2.19	Equilibrium in the Fe-Al-Mn-O system	61
	2.20	Equilibrium in the Fe-Ti-O system	64
	2.21	The Ti-O system	71
III		APPARATUS AND EXPERIMENTAL TECHNIQUE	75
	3.1	Introduction	75
	3.2	Apparatus	75
		3.2.1 The furnace	75
		3.2.2 The gas train	80

CHAPTER			Page
		3.2.3 The galvanic cell	80
		3.2.4 The cermet preparation	84
	3.3	Experimental technique	84
		3.3.1 EMF measurements	84
		3.3.2 Temperature measurements	88
	3.4	Oxide phase identification	88
	3.5	Testing of solid electrolyte crucibles	91
		3.5.1 Bulk density measurements	91
		3.5.2 Leak testing	92
		3.5.3 Microscopic examination	92
	3.6	Materials	94
IV	EXPERIMENTAL RESULTS		97
	4.1	Introduction	97
	4.2	$\text{Log}h_O$ from measured EMF	98
	4.3	Results in the Fe-Nb-O system	99
		a) Transition point equilibrium	99
		b) Deoxidation products	110
	4.4	Results in the Fe-Al-O system	114
		a) Transition point equilibrium	114
		b) Third law analysis of data	123
		c) Data for the reaction: $FeAl_2O_{4(s)} \rightleftarrows Fe_{(\ell)} + 2\underline{Al}_{\text{1w/o}} + 4\underline{O}_{\text{1w/o}}$	125
		d) Deoxidation products	133
	4.5	Results in the Fe-Al-Mn-O system	133

CHAPTER			Page
V	DISCUSSION		142
	5.1	Introduction	142
	5.2	The concentration cell	142
	5.3	Levels of uncertainty	147
	5.4	The Fe-Nb-O system	148
		a) Thermodynamic data	148
		b) The transition point between NbO-NbO_2	151
		c) The morphology of the reaction products	152
	5.5	The Fe-Al-O system	153
		a) Thermodynamic data	153
		b) The deoxidation products	155
	5.6	The Fe-Al-Mn-O system	156
		a) Thermodynamic and structural considerations	156
		b) Steelmaking considerations	160
VI	SUMMARY AND CONCLUSIONS		162
APPENDIX AI	Results in the Fe-Ti-O system		166
		a) Experimental	166
		b) Possible explanations	171
REFERENCES			175

LIST OF ILLUSTRATIONS

FIGURE		Page
2.1	Schematic representation of the deoxidation diagram for Fe-M-O system (From ref. 6)	7
2.2	Schematic representation of the $\log h_O$ versus time trace for Fe-M-O system, while reducing (From ref. 6)	10
2.3	Three dimensional representation of the deoxidation diagram in Fe-M-O system (From ref.6)	11
2.4	Deoxidation equilibria in liquid iron alloys at 1600°C (From ref. 21)	15
2.5	Electrolytic domain for CSZ and YDT after Patterson[44]	21
2.6	Different designs of oxygen probes	28
2.7	The Nb-O phase diagram (From ref. 105)	41
2.8	Region of spinel stability in the $FeO-MnO-Al_2O_3$ system (From ref. 1)	62
2.9	Effect of manganese at the deoxidation behavior of aluminum at 1600°C (From ref. 1)	62
2.10	Effect of manganese on the aluminum and oxygen contents of liquid iron in equilibrium with alumina and aluminate spinel at 1600°C (From ref. 1)	63

FIGURE		Page
2.11	Region of stability of Titanium oxides as reported by several authors	70
2.12	The Ti-O phase diagram[165]	72
3.1	The furnace and temperature control assembly (not to scale)	77
3.2	Temperature profile of the resistance furnace	79
3.3	Schematic representation of the gas train	81
3.4	Schematic diagram of the galvanic cell	82
3.5	A cermet mounted in an alumina tube, before and after use for 1 hr at 1600°C	85
3.6	Schematic diagram of the apparatus used for the iodine etching technique	90
3.7	Apparatus for mercury displacement, volume measurements	93
3.8	CSZ crucible micrographs	95
4.1	Experimental run in the Fe-Nb-O system	100
4.2	Experimental run in the Fe-Nb-O system	101
4.3	Experimental run in the Fe-Nb-O system	102
4.4	Experimental run in the Fe-Nb-O system	103
4.5	Experimental run in the Fe-Nb-O system	104
4.6	$\log h_O$ versus $\frac{1}{T}$ for the reaction: $FeNb_2O_{6(s)} \rightleftarrows Fe_{(\ell)} + 2NbO_{2(s)} + 2\underline{O}$ 1w/o	107
4.7	ΔG^O_T versus T for the reaction: $FeNb_2O_{6(s)} \rightleftarrows Fe_{(\ell)} + 2NbO_{2(s)} + 2\underline{O}$ 1w/o	109
4.8	Morphology of inclusions in the Fe-Nb-O system	112
4.9	Morphology of inclusions in the Fe-Nb-O system	113

FIGURE		Page
4.10	Experimental run in the Fe-Al-O system	115
4.11	Experimental run in the Fe-Al-O system	116
4.12	Experimental run in the Fe-Al-O system	117
4.13	Experimental run in the Fe-Al-O system	118
4.14	Experimental run in the Fe-Al-O system	119
4.15	$Logh_O$ versus $\frac{1}{T}$ for the reaction: $FeAl_2O_{4(s)} \rightleftharpoons Fe_{(\ell)} + Al_2O_{3(s)} + \underline{O}$ lw/o	122
4.16	ΔH^O_{298} for the reaction: $FeAl_2O_4 \rightleftharpoons Fe + Al_2O_3 + \frac{1}{2}O_2$, calculated by third law analysis	126
4.17	ΔG^O_T versus T for the reaction: $FeAl_2O_{4(s)} \rightleftharpoons Fe_{(\ell)} + Al_2O_{3(s)} + \underline{O}$ lw/o	127
4.18	ΔG^O_T versus T for the reaction: $FeAl_2O_{4(s)} \rightleftharpoons Fe_{(\ell)} + 2\underline{Al}$ lw/o $+ 4\underline{O}$ lw/o	129
4.19	Morphology of inclusions in the Fe-Al-O system	131
4.20	Morphology of inclusions in the Fe-Al-O system	132
4.21	Experimental run in the Fe-Al-Mn-O system	134
4.22	Experimental run in the Fe-Al-Mn-O system	135
4.23	Experimental run in the Fe-Al-Mn-O system	136
4.24	Experimental run in the Fe-Al-Mn-O system	137
4.25	$Logh_O$ and $logh_{Al}$ versus [%Mn] at 1550°C, for the transition Al_2O_3 - $(Fe,Mn)O.Al_2O_3$	140
4.26	Inclusion morphology in the Fe-Al-Mn-O system	141

FIGURE		Page
5.1	Logh_O versus logh_{Al} for the Fe-Al-Mn-O system	158
AI.1	Experimental run in the Fe-Ti-O system	167
AI.2	Plateaus of short duration in the Fe-Ti-O system	169
AI.3	Logh_O versus logh_{Ti} (not to scale)	173

LIST OF TABLES

TABLE		Page
2.1	Free energy of formation of Cr_2O_3	34
2.2	Studies of the Fe-Nb-O liquid system	39
2.3	Experimental values of deoxidation constant $K_{(2.64)} = [\%Al]^2[\%O]^3$	44
2.4	Experimental values of equilibrium constant $K = h_{Al}^2 . h_O^3$	48
2.5	Experimental values for hercynite formation	53
2.6	The standard free energy of formation of alumina ΔG_T° from thermochemical data	58
2.7	Free energy change for the reaction $Al_{(\ell)} \rightleftarrows Al_{1w/o}$	60
2.8	Summary of results in the Fe-Ti-O system	66
3.1	Analysis of Ferrovac E in weight percent	96
3.2	Analysis and size of chemicals used	96
4.1	Experimental results on the Fe-Nb-O system	106
4.2	X-ray diffraction pattern from Fe-Nb-O deoxidation products	111
4.3	Experimental results on the Fe-Al-O system	121
4.4	Third Law Analysis of data for reaction 4.17	124
4.5	X-ray diffraction pattern from Fe-Al-O deoxidation products	130

TABLE		Page
4.6	Effect of Mn on Al_2O_3-(Fe,Mn)O.Al_2O_3 transition point	139
AI.1	Upper plateaus in the Fe-Ti-O system	170
AI.2	Intermediate plateaus in the Fe-Ti-O system (Fig. AI.2)	170

LIST OF SYMBOLS

s, ℓ, g	(subscripts) indicate the physical state of the material, i.e. solid, liquid and gas respectively.
$\underline{X}$	indicates that X is in solution in liquid iron.
lw/o	(subscript) refers to the 1 wt. pct. standard state.
K	equilibrium constant for the reaction as written.
h_i & f_i	Henrian activity and activity coefficient of componeht i respectively.
T	absolute temperature in degrees kelvin
P_i	partial pressure of gaseous species i
f_i^j	gives the effect of solute j on the activity coefficient of i ($f_i = \prod_{j=1}^{n} f_i^j$ where j = 1 to n represents n solutes in iron).
e_i^j	interaction parameter, $e_i^j = \frac{\partial \log f_i}{\partial [\%j]}$
K'	deoxidation "constant" (obtained by replacing activities in K by concentrations).
ΔG°	change in the Gibbs standard free energy.
E	electromotive force of an electrochemical cell.
F	Faraday, 96494 coul/mole.
R	gas constant, 1.987 cal/mole-deg.
μ_i	chemical potential of element i
t_i	transference number of species i
σ_i	conductivity of species i
c_i	concentration of species i
q_i	charge of species i
u_i	mobility of species i
$P_\oplus$	partial pressure of oxygen when $\sigma_{ion} = \sigma_\oplus$ where $\oplus$

denotes a positive hole.

P_Θ partial pressure of oxygen when $\sigma_{ion} = \sigma_\Theta$, where Θ denotes an excess electron.

Q_i activation energy of species i

σ_i° constant in Arhenius-type expressions for conductivity $\sigma_i = \sigma_i^\circ \exp(-Q_i/RT)$

Λ_i equivalent conductivity of component i

$$\Lambda = \frac{\sigma}{cz}$$

D_i diffusivity of component i

γ_i Raoultian activity coefficient of solute i.

γ_i° γ_i at infinite dilution (i.e. slope of the Henry's law line)

f (subscript) formation of the product from the elements.

$\overline{\Delta G}_x$ change of the Gibbs' free energy for the reaction

$$x_{(\ell)} \rightleftarrows \underline{x} \text{ lw/o}$$

gef_T Gibbs' energy function given by:

$$gef_T = \frac{G_T^\circ - H_{298}^\circ}{T}$$

ΔH_T° change in the standard enthalpy at temperature T.

CHAPTER I

INTRODUCTION

Deoxidation has always been one of the most important problems in steelmaking. The oxygen excess after refining, can be removed either as carbon monoxide during solidification (rimmed steels) or as nonmetallic inclusions (killed steels). The latter condition is achieved by the addition to the melt, of strong deoxidisers, that is, metals which exhibit a high chemical affinity for oxygen. Manganese, silicon and aluminum have been traditionally used for this purpose.

Control of the nature of the inclusions formed is also of great importance, the efficiency of inclusions removal from the metallic melts depending on inclusion type. In cases where more than one oxide is formed by one deoxidiser, the lower oxides are the ones which are more easily removed.

In addition to deoxidation there are other reasons for introducing microalloying elements into steel. Carbides, nitrides, sulfides, oxysulfides, are some of the inclusions that can be formed and the mechanical properties of the final product, depend greatly on the nature and the shape of these inclusions. Hence, control of inclusion formation is essential.

This is particularly true in the manufacture of high-strength, low-alloy (HSLA) steels, where microalloying elements play a critical role in controlling the various types of temperature dependent precipitation reactions which take place during their manufacture. Niobium, forming carbonitrides, and titanium, forming oxides, carbides and nitrides, have been extensively used in the manufacture of HSLA steels.

Whether or not a particular alloying element is used to form oxide inclusions in steel, the study of its deoxidation thermodynamics is necessary. At high oxygen potentials in the melt, most alloying elements can be oxidised, thus becoming unavailable for any subsequent precipitation reactions. Equilibration techniques combined with chemical analysis were the first to be employed for the study of deoxidation thermodynamics. These have been recently replaced to a great extent by electrochemical techniques employing solid-oxide electrolytes usually calcia-stabilised zirconia or yttria doped thoria. Thus, oxygen activity can be more accurately determined, but solution thermodynamics have to be employed to determine the activity of the alloying element in the melt. In cases where more than one oxide product can be formed, the oxygen activity for the transition from one product to the other, can only be determined indirectly.

In this work, a direct method for determining the oxygen activity at the transition point has been developed, based on an electrochemical cell of the type:

$$Mo|Cr\text{-}Cr_2O_3|CSZ|Fe_{(\ell)},\underline{O},\underline{M}|\underset{cermet}{Mo\text{-}ZrO_2}|Mo \qquad (1.1)$$

The systems studied were: Fe-Nb-O, Fe-Al-O and Fe-Al-Mn-O.

The free energy changes for the reactions:

$$FeNb_2O_{6(s)} \rightleftarrows Fe_{(\ell)} + 2NbO_{2(s)} + 2\underline{O}_{1w/o} \quad (1.2)$$

$$FeAl_2O_{4(s)} \rightleftarrows Fe_{(\ell)} + Al_2O_{3(s)} + \underline{O}_{1w/o} \quad (1.3)$$

and the influence of Mn on the equilibrium oxygen activity of the reaction:

$$(Fe_{1-x}, Mn_x)\ Al_2O_{4(s)} \rightleftarrows (1-X)Fe_{(\ell)} + Al_2O_{3(s)} + x\underline{Mn}_{1w/o} + \underline{O}_{1w/o} \quad (1.4)$$

were determined in the temperature range 1550° - 1600°C.

The deoxidation products were identified by X-ray diffraction analysis and their morphology examined by scanning electron microscopy.

An attempt was also made to study the Fe-Ti-O systems at oxygen activities corresponding to a Ti_3O_5 - TiO_2 transition. The results obtained in this system are presented in Appendix I, as they have not been fully resolved.

CHAPTER II

LITERATURE REVIEW

2.1 Introduction

This chapter reviews the work reported in the literature related to this investigation. The review is divided into three main sections:

(A) The first section deals with general considerations concerning steel deoxidation. The theoretical background of the thermodynamics of steel deoxidation systems is given. Reference is made to the conditions under which different deoxidation products can occur, and the significance of the transition point from one deoxidation product to another is discussed. The thermodynamics of the reaction $\frac{1}{2}O_2(g) \rightleftarrows \underline{O}_{1w/o}$ are reviewed and the solubility minima of oxygen in Fe-O-M melts are discussed. Finally a brief review on inclusions in deoxidation is presented.

(B) The second section deals with the use of solid electrolytes in steel deoxidation studies. Oxygen concentration galvanic cells, and the properties of calcia stabilised zirconia are reviewed. Data for the free energy of formation of Cr_2O_3 are reviewed as Cr/Cr_2O_3 mixtures were used as reference electrodes in this study.

(C) In the final section the deoxidation systems studied in this investigation i.e. Fe-Nb-O, Fe-Al-O, Fe-Al-Mn-O and Fe-Ti-O, are reviewed.

A. Steel Deoxidation

2.2 Deoxidation equilibria in Fe-M-O systems

Most of the deoxidising elements used to deoxidise steel, form more than one deoxidation product. The formation of any particular product depends on the initial oxygen content in the melt, the residual deoxidant content and the temperature.

In a simple ternary system, Fe-M-O, where M represents the elements Al, Cr, Nb, Ti or V, one of the products is a complex oxide $FeO.M_2O_x$ and the other is a simple oxide of the general form M_2O_x. Other oxides can be formed, at lower oxygen potentials but the discussion here will only deal with the two mentioned above as the treatment is equally applicable to any other case.

Under conditions in which $FeO.M_2O_x$ is the stable product, one may write

$$Fe(\ell) + 2\underline{M}\ \text{lw/o} + (x+1)\ \underline{O}\ \text{lw/o} \rightleftharpoons FeM_2O_{(x+1)} \qquad (2.1)$$

Assuming that the product is in a pure condensed phase, as is true in most cases, the equilibrium constant for equation (2.1) can be written as

$$k_{(2.1)} = \frac{1}{h_M^2 \quad h_O^{(x+1)}} \qquad (2.2)$$

For conditions under which M_2O_x is the stable product, one

may write:

$$2\underline{M}_{1\ w/o} + x\underline{O}_{1\ w/o} \rightleftarrows M_2O_x \qquad (2.3)$$

Assuming again that M_2O_x is in a pure condensed state the equilibrium constant for equation (2.3) may be written as:

$$k_{(2.3)} = \frac{1}{h_M^2 \quad h_O^x} \qquad (2.4)$$

From equations (2.2) and (2.4) respectively:

$$\log h_O = -(\frac{1}{x+1}) \log K_{(2.1)} - (\frac{2}{x+1}) \log h_M \qquad (2.5)$$

and:

$$\log h_O = -(\frac{1}{x}) \log K_{(2.3)} - (\frac{2}{x}) \log h_M \qquad (2.6)$$

Plotting $\log h_O$ versus $\log h_M$, straight lines are obtained with slopes of $-\frac{2}{x+1}$ and $-\frac{2}{x}$ and intercepts of $-(\frac{1}{x+1}) \log K_{(2.1)}$ and $-(\frac{1}{x}) \log K_{(2.3)}$ for melts in equilibrium with $FeO.M_2O_x$ and M_2O_x respectively. At the point of intersection of these two lines, the melt is in equilibrium with both oxides and the following reaction is in equilibrium.

$$Fe\ M_2O_{(x+1)\ (s)} \rightleftarrows Fe_{(\ell)} + \underline{O}_{1\ w/o} + M_2O_{x\ (s)} \qquad (2.7)$$

Fig. (2.1) is a schematic representation of the deoxidation diagram for an Fe-M-O system.

In general the higher oxide has a lower interfacial energy in steel than M_2O_x, which is more readily absorbed by a slag cover and is thus more easily removed from the liquid steel[1,2].

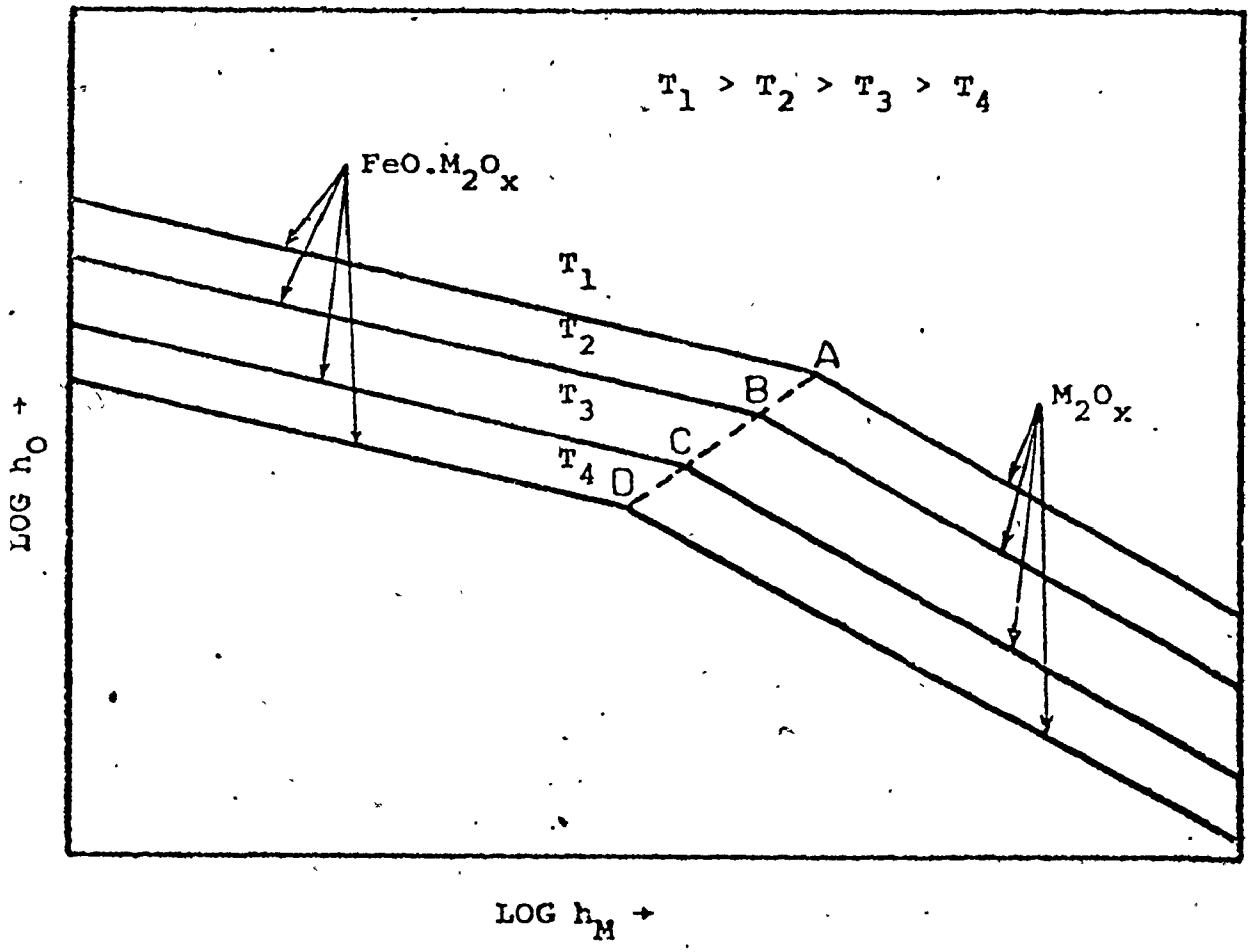

Figure 2.1 Schematic representation of the deoxidation diagram for Fe-M-O system (From ref. 6)

The importance of the transition point is thus easily recognizable. Deoxidation should occur only through the formation of the M_2O_x oxide i.e. at oxygen activities lower than those given by points A, B, C and D in Fig. 2.1. For successful deoxidation, precise data concerning these points are therefore essential.

2.3 Determination of the transition points

Indirect as well as direct methods have been used to determine the position of the transition points.

The indirect methods consist of equilibrating an Fe-M-O melt with a gaseous mixture of known oxygen potential, such as H_2/H_2O or CO/CO_2, at steelmaking temperatures, quenching the melt and analysing for O and M. The oxide phase in equilibrium is also identified. Interaction parameters are used to transform composition to henrian activity and in plots of $\log h_O$ versus $\log h_M$, straight lines, according to equations (2.5) and (2.6) are obtained[3,4,5].

Interpolation of the straight lines for two different oxides at low and high deoxidant content gives the transition oxygen activity at the point of intersection.

The direct methods are based on the monitoring of the oxygen activity in an Fe-M-O melt during oxidising or reducing conditions. Assuming that, in equation (2.7), M_2O_x and $FeM_2O_{(x+1)}$ are pure and do not form a solid solution, we find upon the application of Gibbs' phase rule that equation (2.7) has only one degree of freedom. At constant temperature, therefore, the transition point is unique and the value of $\log h_O$, remains

constant under reducing or oxidising conditions as long as two deoxidation phases coexist.

Plotting h_O versus time in an oxidation or reducing experiment should give a plateau at a constant temperature where $\partial h_O/\partial t = 0$, Fig. 2.2.

The equilibrium constant for equation (2.7) may be written as:

$$K_{(2.7)} = h_O \tag{2.8}$$

and expressing $K_{(2.7)}$ as a function of temperature, one may write:

$$\log h_O = \log K_{(2.7)} = -\frac{A}{T} + B \tag{2.9}$$

where A and B are constants. The constants A and B may be calculated from the free energy change for the reaction (2.7) and a plot of $\log h_O$ versus $\frac{1}{T}$, should yield a straight line. Fig. 2.3 schematically shows a deoxidation diagram in three dimensions.

Vahed[6] has studied the system Fe-V-O and determined the transition point for the phases FeV_2O_4 - V_2O_3 using calcia stabilised zirconia and probes for spot measurements of the oxygen activity of the melt. He also used thoria-yttria crucibles as solid electrolytes in galvanic cells where he continuously monitored the oxygen activity.

Apte[7] used an oxygen concentration galvanic cell, identical with the one used in this study, for continuously monitoring the oxygen activity of liquid Fe-V-O and Fe-Cr-O systems and determining the respective transition points. Several people have used the indirect method for studying deoxidation systems. Jaquemont et al.[8] have given an excellent

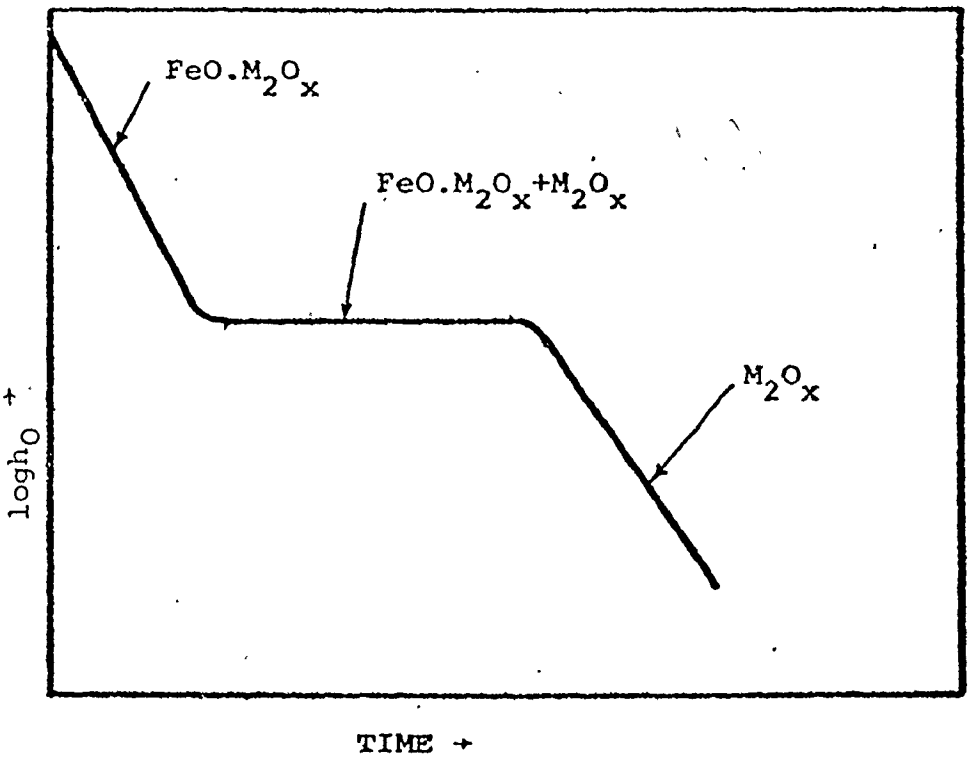

Figure 2.2 Schematic representation of the $\log h_O$ versus time trace for Fe-M-O system, while reducing (From ref.6)

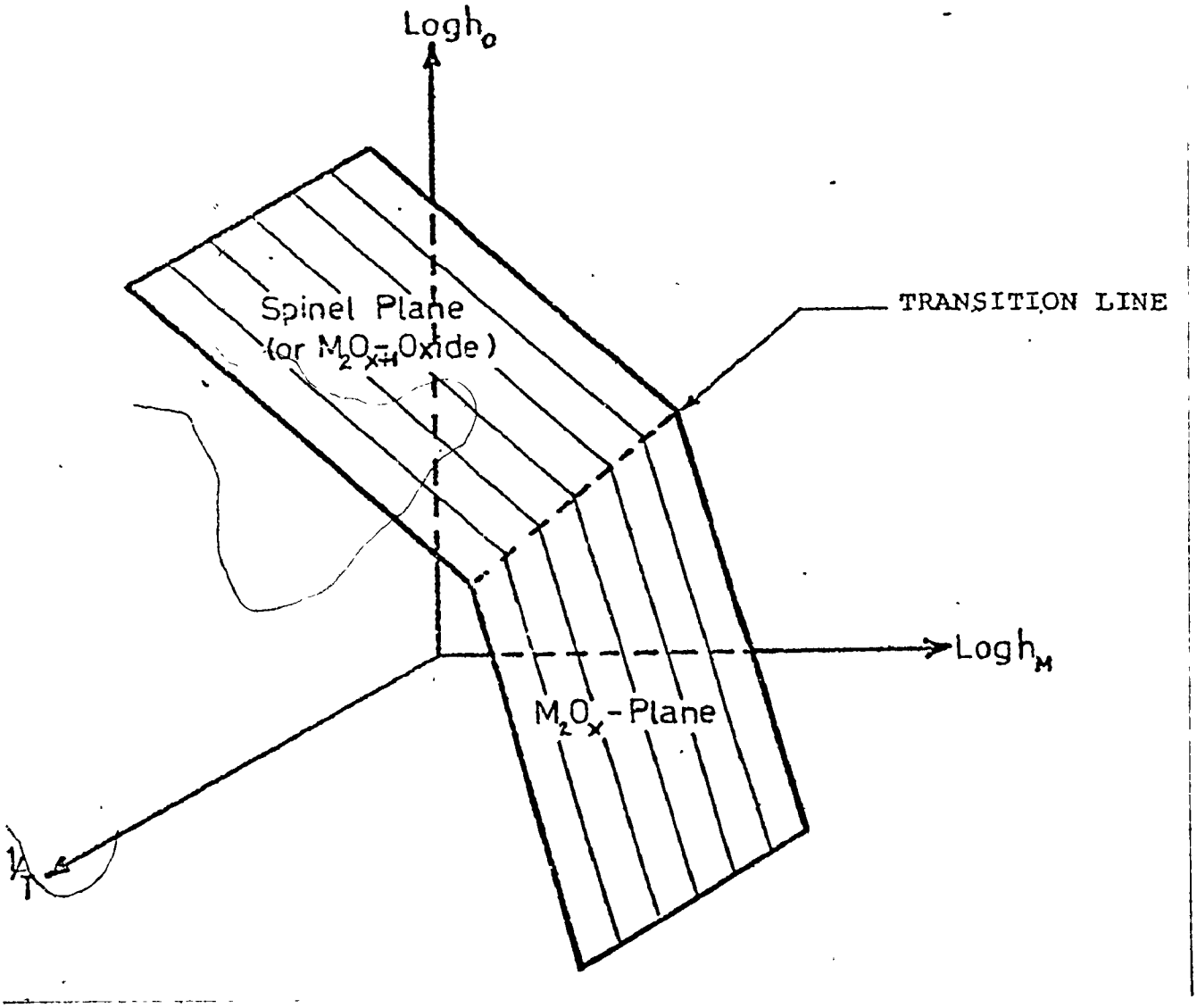

Figure 2.3 Three dimensional representation of the deoxidation diagram in Fe-M-O system (From ref. 6)

literature survey of iron deoxidation systems. They have critically assessed experimental results given in the literature and have selected the most reliable thermodynamic data. Sigworth and Elliott[9] have also done a literature survey on the thermodynamics of dilute liquid iron alloys and present interaction coefficients for several deoxidation systems.

2.4 The Binary Fe-O system

The role of oxygen as a principal reagent in the refining of liquid iron and the necessity for its removal in the final product have stimulated many studies of its chemical behaviour in liquid iron. The usual method employed is equilibration of molten metal with a gaseous atmosphere of known oxygen potential, normally mixtures of CO/CO_2 or H_2/H_2O of known composition. The melt is quenched and oxygen in solution is determined by vacuum or inert gas fusion techniques. Using the H_2/H_2O gas mixtures the following reaction may be written:

$$H_2(g) + \underline{O}_{1\ w/o} \rightleftharpoons H_2O(g) \qquad (2.10)$$

The equilibrium constant for (2.10) is:

$$K_{(2.10)} = \frac{P_{H_2O}}{P_{H_2}} \cdot \frac{1}{h_O} \qquad (2.11)$$

and:

$$h_O = f_O\,[\%O] \qquad (2.12)$$

Since:

$$\log f_O = \log f_O^O = e_O^O[\%O] \qquad (2.13)$$

equation (2.11) can be rewritten as:

$$\log K_{(2.10)} = \log K'_{(2.10)} - e_O^O[\%O]$$

where $K'_{(2.10)}$ is the apparent equilibrium constant:

$$K'_{(2.10)} = \frac{P_{H_2O}}{P_{H_2}} \frac{1}{[\%O]} \qquad (2.15)$$

From equation (2.14) it is obvious that a plot of log $K'_{(2.10)}$ versus [%O] should yield a straight line of slope e_O^O and that log K, is the intersept at infinite dilusion of oxygen. Various workers[3,10-19] have reported results for the Fe-O system and there is a rather large discrepancy between their values of $K_{(2.10)}$ arising mainly from errors in oxygen analysis and the existence of thermal diffusion in H_2/H_2O gas mixtures.

Floridis and Chipman[16], in a very careful study, found slight non-henrian behaviour of oxygen in liquid iron, the activity coefficient being given by the relation:

$$\log f_O = -0.20[\%O] \qquad (2.16)$$

The values of $K_{(2.10)}$ were found to be 4.68 and 3.65 at 1550°C and 1600°C respectively. Combining this with data given previously by Dastur and Chipman[13] the following temperature dependence of $K_{(2.10)}$ is obtained:

$$\log K_{(2.10)} = 7050/T - 3.20 \qquad (2.17)$$

$$\Delta G^O_{(2.10)} = -32,200 + 14.63T \qquad (2.18)$$

Combining (2.18) with the standard free energy of formation of $H_2O(g)$:[20]

$$\Delta G^O_{(2.10)} = -60,200 + 13.94T \qquad (2.19)$$

the free energy change for the reaction:

$$\tfrac{1}{2}O_2(g) \rightleftarrows \underline{O}_{1w/o} \qquad (2.20)$$

is given by:

$$\Delta G_{(2.20)} = -28,000 - 0.69T \qquad (2.21)$$

2.5 Solubility minima of oxygen in liquid Fe-O-M alloys

Equations (2.5) and (2.6) indicate a linear relationship between h_O and h_M in equilibrium with different deoxidation products. However in plots of [%O] vs [%M], most deoxidisers exhibit a minimum in the deoxidation equilibrium curve at high deoxidant concentration. Subsequent additions of deoxidisers thus increase the soluble oxygen content.

Turkdogan[21] has reviewed studies by Fruehan[22-24] using Cr, V, B, Ti, Al as deoxidisers and has used compiled data[25] for Mn, Si, C. Fig. 2.4 is taken from reference (21) and shows oxygen solubility minima for most common deoxidisers. Studies by Kontopoulos[3] on vanadium, Fischer and Janke[26] on boron, Narita and Koyama[27] on niobium and Schenk et al.[28] on carbon, also indicate the existence of oxygen solubility minima in molten Fe-O-M alloys.

The phenomenon is of great practical importance in steelmaking and can be explained[21] by considering the effect of alloying elements on the activity coefficient of oxygen. As the deoxidant content increases, its activity increases. However, since e_O^M is negative, f_O decreases as %M increases thus increasing the tendency of oxygen to enter solution. Eventually this effect becomes so marked that a further addition of deoxidiser results in an increase in the dissolved oxygen content.

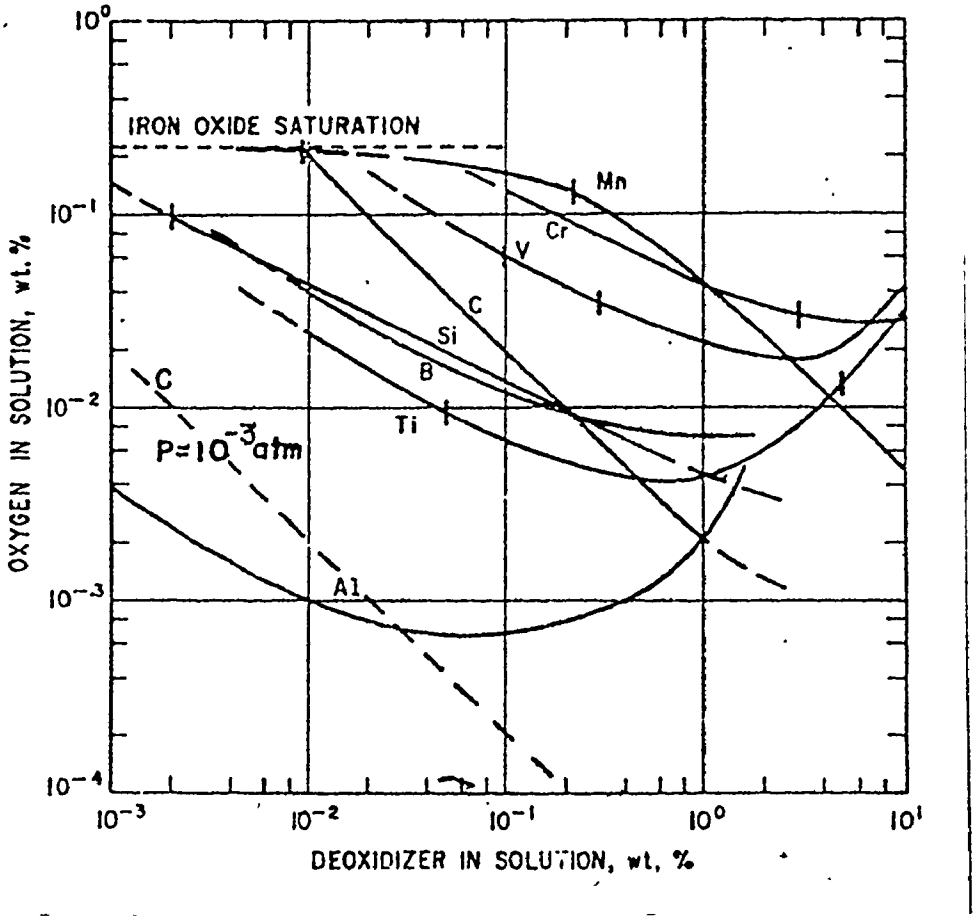

Figure 2.4 Deoxidation equilibria in liquid iron alloys at 1600°C (From ref. 21)

This phenomenon has been treated mathematically[29,30]. Equations relating the position of the "deoxidation minimum" to the equilibrium constant K and first-order interaction parameters have also been derived[31]. Smith and Kirkaldy[32] and Feldman and Kirkaldy[33] have produced an alternative thermodynamic analysis of the phenomenon. Using their analysis and experimental data for several deoxidation systems, they predict values for the Wagner cross-interaction parameters which are in good agreement with direct determinations. It should be noted that univariant transition points should be represented by changes in slope of the curves in Fig. 2.4. However, these changes are not apparent due to experimental scattering. Activity plots give a more accurate determination of such transition points.

2.6 Inclusions in deoxidation

Since an extensive review of the literature dealing with inclusions in deoxidation is not considered necessary for the present study, only a brief discussion is presented here.

As the formation and flotation of deoxidation products is of great practical importance in the deoxidation of steel, a thorough study has been undertaken to understand the kinetics of these phenomena. Turkdogan[21] has given a good review of existing theories on the rate of deoxidation, growth and flotation of inclusions. He emphasises the role of growth by diffusion in contrast with other possible mechanisms such as Brownian motion, Ostwald ripening and collision. Lindborg and Torssell[34] have studied the size distribution function

of particles growing by collision with other smaller particles.

In order to explain the apparent discrepancy between thermodynamic predictions of the oxygen residual in steel after deoxidation and the actual measured values, Turkdogan[35] has introduced the concept of a slow approach to equilibrium at low oxygen potentials thereby implying that equilibrium is not achieved in practice when strong deoxidisers are used. He then introduced the idea of a "practical solubility product" as a measure of the deoxidising capacity of any deoxidiser. It appears that further investigations are necessary in order to reconcile the discrepancies between theoretical prediction and experimental measurements. This is particularly true when rare earths are used for steel deoxidation and desulfurisation. A number of studies[36,37,38] have recently appeared.

The shape and size, as well as the mechanical properties of inclusions have been the subjects of recent investigations because of the increasing use of high-strength low-alloy (HSLA) steels. McLean and Kay[39] have discussed inclusion control in HSLA steels. Practical considerations and alloy additions practice are discussed. A more detailed review concerning the composition and shape of inclusions when Nb, Al, Al-Mn, Ti are introduced into steel, will be found in Chapter 5 where the morphology of the inclusions of the present study is discussed.

B. Galvanic cell measurements using solid Electrolytes

2.7 Introduction

Although EMF measurements with galvanic cells employing solid electrolytes have been used for many years, to obtain thermodynamic data, it was not until 1957 when Kiukkola and Wagner[40] published their work with lime stabilised zirconia, that the advantages of using cells reversible to oxygen ions only, began to be fully realised. Since then, extensive studies using solid electrolyte cells have been undertaken, and their use has been extended to study the thermodynamics of many metal-oxygen systems.

Wagner[41], in 1933, considered theoretically the transport of ions and electrons in a crystalline binary compound $Mz_X Xz_M$ and derived the following relationship:

$$E = -\frac{1}{F}\int_{\mu_X''}^{\mu_X'} t_{ion}\,\frac{d\mu_X}{|Zx|} = -\frac{1}{F}\int_{\mu_M'}^{\mu_M''} t_{ion}\,\frac{d\mu_M}{|Z_M|} \qquad (2.22)$$

where t_{ion} is the sum of the cationic and anionic transference numbers, and μ_X and μ_M are the chemical potentials for the nonmetal and metal respectively. Equation (2.22) serves as a basis for solid electrolyte galvanic cells. It is also obvious from equation (2.22) that the anodic and cathodic reactions, must always involve, as charge carrying species, one of the compounds of the electrolyte. In contrast to aqueous electrolytes, the crystalline compounds exhibit partial electronic conductivities, which are rarely negligible.

Only a few binary and ternary compounds exhibit exclusive ionic conduction ($t_{ion} > 0.99$) and even this is limited to a specific range of metal or nonmetal chemical potentials. It is therefore necessary to determine partial conductivities or partial transference numbers for the electrolyte, to correctly interpret the voltage of a solid electrolyte cell.

Rapp and Shores[42] have given a detailed summary of the defect reactionsoccurring in nonstoichiometric compounds. The same authors also discussed the effect of an alliovalent ion dopant on the partial conductivities of a solid electrolyte.

The discussion that follows deals mainly with oxygen-ion conducting electrolytes as they are the most widely used at high temperatures and have been used exclusively for the present study.

2.8 Transport properties of solid oxide electrolytes

In a solid electrolyte which exhibits mixed ionic and electronic conduction:

$$t_{ion} = \frac{\sigma_{ion}}{\sigma_{total}} = \frac{\sigma_{ion}}{\sigma_{ion}+\sigma_e} \tag{2.23}$$

where σ_i is the conductivity of the species i given by

$$\sigma_i = c_i\, q_i\, U_i \tag{2.24}$$

Schmalzried[43], considering oxygen-ion conducting electrolytes, derived the expression:

$$t_{ion} = \left[1 + \left(\frac{P_{O_2}}{P_{\oplus}}\right)^{1/n} + \left(\frac{P_{O_2}}{P_{\ominus}}\right)^{-1/n}\right]^{-1} \tag{2.25}$$

where $P_{\oplus}$, $P_{\ominus}$ and n are constants. He substituted this expression for t_{ion} into equation (2.22) and found, after integration:

$$E = \frac{nRT}{4F}\left[\ell n \frac{P_{\oplus}^{1/n} + P_{O_2}'^{1/n}}{P_{\oplus}^{1/n} + P_{O_2}''^{1/n}} + \ell n \frac{P_{\ominus}^{1/n} + P_{O_2}''^{1/n}}{P_{\ominus}^{1/n} + P_{O}'^{1/n}}\right] \quad (2.26)$$

where P_{O_2}'' and P_{O_2}' correspond to the standard and the variable electrode respectively. Equation (2.26) can be used to predict the galvanic cell voltage for any pair of electrodes if the three empirical parameters n, $P_{\oplus}$, $P_{\ominus}$ are determined. From equation (2.25) it follows that for very low or very high values of P_{O_2}, t_{ion} will vary significantly from unity.

$P_{\oplus}$ and $P_{\ominus}$ are temperature dependent and follow relationships of the type:[44]

$$P_{\oplus} = -n\left(\frac{Q_{ion}-Q_{\oplus}}{2.303R}\right)\frac{1}{T} + n \log \frac{\sigma^{\circ}_{ion}}{\sigma^{\circ}_{\oplus}} \quad (2.27)$$

and

$$P_{\ominus} = n\left(\frac{Q_{ion} - Q_{\ominus}}{2.303R}\right)\frac{1}{T} - n \log \frac{\sigma^{\circ}_{ion}}{\sigma^{\circ}_{\ominus}} \quad (2.28)$$

where Q_{ion}, $Q_{\ominus}$ and $Q_{\oplus}$ are activation energies for σ_{ion}, $\sigma_{\ominus}$, $\sigma_{\oplus}$ respectively.

Patterson[44] has suggested the use of partial pressure vs $\frac{1}{T}$ diagrams to represent the domains of a solid electrolyte where t_{ion} is usually > 0.99.

Fig. 2.5 shows the electrolyte domain for calcia stabilised zirconia and yttria doped thoria as given by Patterson.

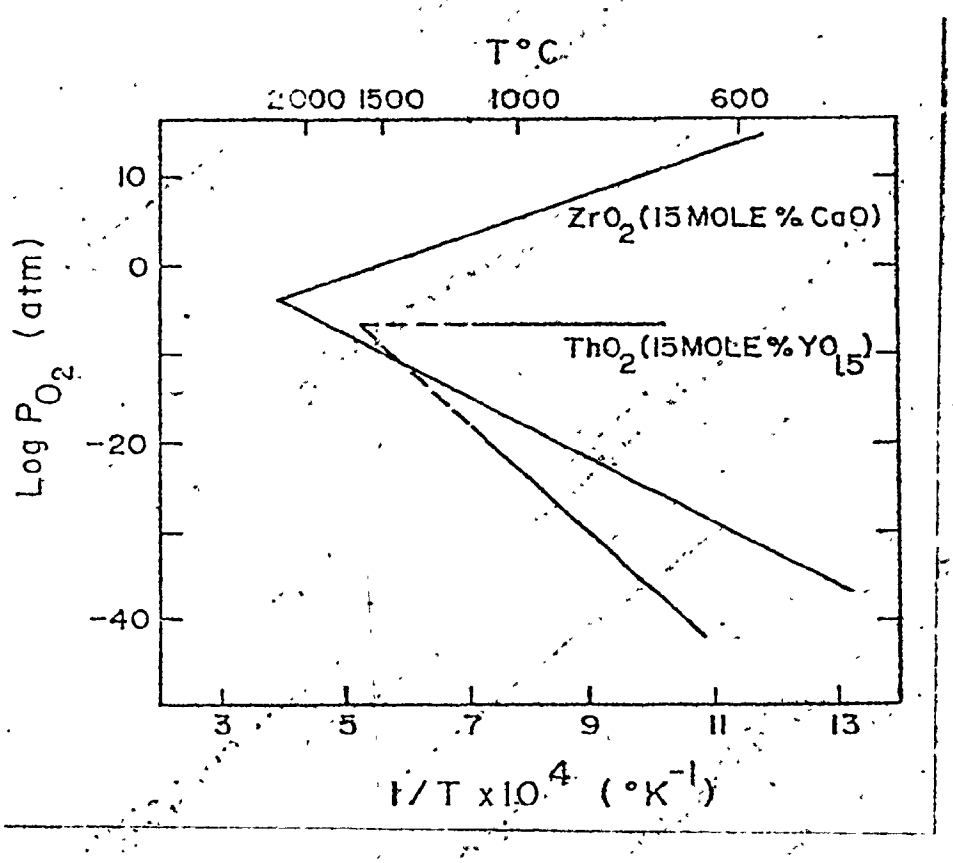

Figure 2.5 Electrolytic domain for CSZ and YDT after Patterson (44)

Worrell[45] has reviewed the electrochemical properties of solid ceramic electrolytes using thoria-yttria solid solutions as specific examples. Defect structures and conductivity mechanisms in predominantly ionic solids have been summarized.

2.9 Transference Number Measurements

Several techniques have been used to determine the ionic and electronic contribution to the conductivity. They have been reviewed by Rapp and Shores[42] and Etsell and Flengas[46].

Specimens can be electrolysed between reversible metal or oxygen electrodes and the quantity of matter transferred measured and compared to the current passed. Electrolysis can be carried out between two or more oxide pellets in series and weight losses or gains recorded. An EMF[47,48] method can also be used in which ionic transport numbers can be determined as:

$$t_{ion} = \frac{E_{meas}}{E_{thermo}} \qquad (2.29)$$

E_{meas}[49] is the measured EMF and E_{thermo} is the thermodynamic EMF calculated for the case where $t_{ion} = 1$. This method is not always accurate. If the electronic conductivity is large (i.e. > 0.1), open circuit oxygen transfer occurs from the high to the low-potential side. The electrodes may become polarised, the EMF dropping below the true value.

Equation (2.25) can be used to evaluate t_{ion} if P_{O_2}, $P_{\oplus}$, $P_{\ominus}$ and n are known.

Lasker and Rapp[50] have reported two-probe conductivity measurements for a series of ThO_2-Y_2O_3 solutions over a wide range of P_{O_2} and temperature. For fairly large ionic-transport numbers, oxygen permeability measurements can be used providing that sufficiently dense material is available so that transport through pores does not interfere. The individual ionic contribution can be separated by measuring diffusion coefficients and calculating partial conductivities from the Nernst-Einstein relation: $\Lambda=\ell_+ + \ell_- = \frac{zF^2}{RT}(D_+ + D_-)$. Ilschner-Gench and Wagner[51] have reported a semi-quantitative method for measuring transference numbers from local cell action during the scaling of metals. Meier and Rapp[52] used a local-cell scaling experiment to evaluate the compounds Be_3N_2 and Th_3N_4 as potential solid electrolytes.

2.10 Solid electrolyte galvanic cells for thermodynamic and kinetic studies

There is a wide range of application of solid electrolyte galvanic cells in electrochemical equilibrium as well as in kinetic studies. A good summary of these applications is given by Rapp and Shores[42], Worrell et al.[45] and a brief description only will be given in this section.

2.10.1 Equilibrium measurements

The thermodynamics of formation of binary compounds have been studied by several workers for different systems, using direct electrodes[53], or direct and coexistance electrodes[54]. Kiukiola and Wagner[40] and many other

investigators have studied cells with two coexistance electrodes of the type:

$$M', M'O/CSZ/M'', M''O \qquad (2.30)$$

The EMF of the above cell is given as:

$$E = -\frac{1}{2F}(\Delta G^{\circ}_{M'O} - \Delta G^{\circ}_{M''O}) \qquad (2.31)$$

Exchange electrodes have been used for several studies and the cell:

$$Ag/AgI/Ag_2Se/Se_{(\ell)},C \qquad (2.32)$$

has been used[40] for example, the EMF for which is:

$$E_{(2.32)} = (-\frac{1}{2F})\ \Delta G^{\circ}_{Ag_2Se} \qquad (2.33)$$

The thermodynamics of formation of ternary compounds have been reported by numerous authors such as Taylor and Schmalzried[55], Schmalzried and Tretyakov[56], Benz and Wagner[57] Rezukina et al.[58,59]

Thermodynamic activities in solid[40,60] and liquid[61,62] alloys have been studied and many engineering applications, such as fuel cells[63] and oxygen activity probes in liquid metal baths, have been reported.

2.10.2 Kinetic measurements

Because of the higher accuracy in measuring current or voltage rather than volume, weight, composition or other properties of reactant or product phases, electrochemical techniques are ideal for measuring the rates or reaction and the correlation of those rates to the corresponding driving force. Hence the great number of applications and the

continuously increasing interest of these techniques to kinetic measurements is understandable. Solid electrolyte galvanic cells have been used in a coulometric titration method to study the composition of several compounds such as FeO[64,65], NbO_2[66] and UO_2[67].

Rickett and coworkers[68,69] have studied the rate of growth of NiS on Ni and the rate of reaction of Ag and Cu with liquid sulfur. Evaporation and condensation using electrochemical methods[70,71] and reactions between gases and compounds have been studied[72]. Dissolution and diffusion studies have also been reported for interstitial and substitutional solids[73,74,75].

In spite of the difficulties in performing kinetic studies with electrochemical cells at high temperatures, due to the absence of suitable electrolytes, an increasing number of new studies is appearing in the literature.

2.11 The Oxygen concentration cell

The oxygen concentration cell consists of two electrodes, I and II, with oxygen chemical potentials μ_I and μ_{II} respectively, separated by a solid oxide electrolyte which conducts essentially via oxygen ions.

$$M|\mu_I(O_2)|\text{solid oxide electrolyte}|\mu_{II}(O_2)|M \qquad (2.34)$$

At elevated temperatures (>500 C) this cell is the source of an electromotive force E which is given by the expression[40]

$$E = \frac{1}{4F}\int_{\mu_I(O_2)}^{\mu_{II}(O_2)} t_i \, d\mu_{O_2} \qquad (2.35)$$

It is evident that in order to measure thermodynamic properties of systems containing oxygen, the solid electrolyte used must be essentially an anionic conductor ($t_i \simeq 1$). Then equation (2.35) becomes

$$E = \frac{RT}{4F} \ln \frac{P_{O_2}^{II}}{P_{O_2}^{I}} \qquad (2.36)$$

where $P_{O_2}^{I}$ and $P_{O_2}^{II}$ represent the oxygen partial pressures in equilibrium with electrodes I and II respectively.

From the steelmakers' point of view such a cell is of great importance as it enables them to measure the oxygen activity in molten steel, rather than the total oxygen content by analytical techniques.

Many investigators have therefore tried to develop cells for directly measuring the oxygen activity of steel baths. Fischer and coworkers[76,77,78] used an oxygen probe employing a calcia stabilised zirconia tube with air as the standard electrode. They used this probe to measure oxygen potentials in H_2O/H_2 mixtures as well as in iron melts. The same authors investigated the ranges of oxygen potentials in which solid electrolytes such as calcia stabilized zirconia, mullite, alumina and magnesium oxide are purely ionic conducting at steelmaking temperatures.

The bad thermal shock resistance of calcia stabilised zirconia tubes was overcome by Fitterer[79,80,81] who used a silica tube with a small pellet of $ZrO_2(CaO)$ electrolyte sealed in one end. Such probes are relatively inexpensive,

and they show a better thermal shock resistance as they only employ an electrolyte pellet. Fitterer employed these probes using air or CO/CO_2 as the standard electrode.

The same type of probe with air as the standard electrode was developed and tested on a laboratory and industrial scale by the Mines Branch of the Department of Energy, Mines and Resources of Canada, and became commercially available through Leigh Instruments Ltd.

Turkdogan and Fruehan[82] used a probe similar to that of Fitterer except that the standard electrode was replaced by a $Cr-Cr_2O_3$ solid mixture. Under these conditions, the standard electrode is compatible with $ThO_2-Y_2O_3$ and $ZrO_2(CaO)$ solid electrolytes. The resulting probe, called the U.S. steel probe has been successfully used in a number of laboratory investigations and is produced commercially by Leeds and Northrup Ltd. In France, the "CELOX" cell was introduced, similar to previous probes[83].

In Fig. 2.6 several designs of the oxygen probes mentioned above, are illustrated.

Vahed[6] was the first to develop an oxygen concentration galvanic cell using the solid electrolyte as a crucible holding the melt. He used $ThO_2-Y_2O_3$ crucibles and Cr/Cr_2O_3 mixtures as the standard electrode to study the thermodynamics of the Fe-V-O system.

Apte[7] and the author have developed a cell similar to that of Vahed, using $ZrO_2(CaO)$ crucibles and a Mo/ZrO_2 cermet contact. The cell can be represented as:

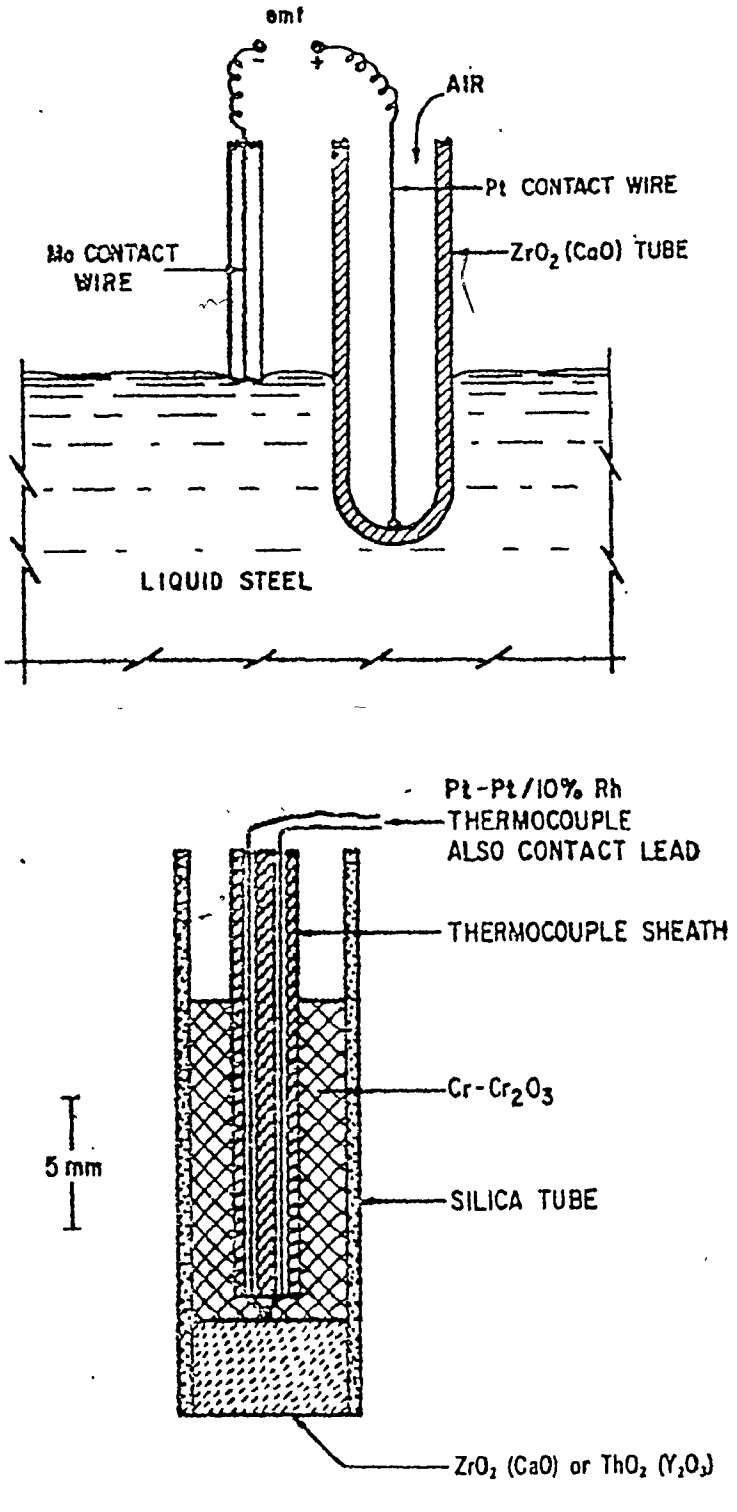

Figure 2.6 Different designs of oxygen probes

$$\oplus, Mo, Mo\text{-}ZrO_2 \text{ cermet} | \underline{O} \text{ in } Fe_{(\ell)} | CSZ | Cr\text{-}Cr_2O_3 | Mo, \ominus \quad (2.37)$$

and the virtual cell reaction is:

$$\underline{O}_{1w/o} + \frac{2}{3} Cr_{(s)} \rightleftarrows \frac{1}{3} Cr_2O_{3(s)} \quad (2.38)$$

The relation between the Henrian activity of oxygen in the melt, the measured EMF and temperature is given in section 4.2. Alcock and Zador[84] have discussed experimental considerations when using solid electrolytes. Ramanarayanan and Worrell[85] and den Hardog and Slangen[86] have reported the limitations and error sources in the use of solid electrolytes for high temperature equilibrium measurements.

A detailed discussion of these subjects will be given in Chapter 5 where the precautions taken to avoid possible errors in the present work are discussed.

2.12 Calcia stabilised zirconia as a solid electrolyte

Calcia stabilised zirconia, usually containing 15 mole % CaO, has been extensively used as a solid electrolyte not only in experimental studies but also on a commercial scale in the form of probes. Garvie[87] and Etsell and Flengas[46] have reviewed the properties of CSZ in terms of equilibrium phase diagrams, lattice parameters and transport numbers. In using CSZ for high temperature equilibrium measurements, the density should be as high as possible and the conduction purely ionic. These are the main aspects that have been extensively studied.

Alcock and Chan[88] have studied the oxygen permeability of stabilised zirconia electrolytes at high tempera-

tures, and concluded that in commercial electrolyte tubes, oxygen permeates through the walls either in the form of neutral oxygen atoms or as oxygen ions associated with positive holes. To minimise the oxygen tendency to permeate through the CSZ tubes when measuring oxygen activity in gases, they introduced Mo/MoO_2 as the reference electrode which has a higher equilibrium partial pressure of oxygen than that of Cr/Cr_2O_3. Cerkasor et al.[89] also studied the oxygen permeability in stabilised zirconium oxide.

Steele and Alcock[90] determined the upper limit of oxygen partial pressure, above which $t_{ion} > 0.99$. They found that positive hole conduction becomes significant at 1000°C when $P_{O_2} > 1$ atm. Tretyacov and Muan [91] found that t_{ion} becomes less than 0.99 for $P_{O_2} > 100$ atm at 1000°C. Patterson[44] in his electrolytic domain determination (Fig. 2.5) gives a value of 10^8 atm. for the upper limit of oxygen partial pressure . The same figure shows that at steelmaking temperatures the upper limit remains at about 1 atm. well above the region of interest in steel deoxidation systems. The lower limit of oxygen partial pressure, that is the oxygen pressure below which appreciable electronic conduction takes place, is of great importance for studies of this kind. At 1000°C, the values reported, vary from 10^{-15} atm.[43] to 10^{-23} atm[92].

At 1600°C Baker and West[49] report significant electronic conductivity at $P_{O_2} < 10^{-8.4}$atm. Fischer and Janke[93] report the lower limit as 2.8×10^{-10} atm.

They measured the equilibrium oxygen partial pressure of H_2O/H_2 gas mixtures using CSZ and air as the reference electrode. Fruehan et al.[82] compared CSZ probes against ThO_2-Y_2O_3 probes and found consistent agreement down to oxygen partial pressure as low as that for Cr/Cr_2O_3 equilibrium. This value is 8×10^{-13} atm. at 1600°C. They estimated that the critical lower value of P_{O_2} for CSZ is less than 3.10^{-13} atm. at 1600°C. Below this value, appreciable drift was observed in the EMF readings, which was attributed to polarisation of the Cr/Cr_2O_3 solid electrode.

Indirect evidence from the present study agrees with the lower limits set by Fruehan. The measurements taken with CSZ and Cr/Cr_2O_3 were stable and reproducible as long as the oxygen potential in the melt electrode was higher than that of Cr/Cr_2O_3.

2.13 The Cr/Cr_2O_3 reference electrode

Cr/Cr_2O_3 has been quite extensively used as a reference electrode in oxygen concentration galvanic cells. The main reason for this is that the partial pressure of oxygen in equilibrium with Cr/Cr_2O_3:

$$\frac{3}{2} O_{2(g)} + 2Cr_{(s)} \rightleftharpoons Cr_2O_{3(s)} \qquad (2.39)$$

is close to that in steelmaking deoxidation systems. However, it has been reported that it displays irreversible[94] behaviour and that the standard free energy change for reaction (2.39) is not as accurately known as that for the Mo/MoO_2 system. Alcock[88] has therefore suggested the use

of Mo/MoO_2 as a reference electrode. However, in this study, Cr/Cr_2O_3 was adopted because it was found that Mo/MoO_2 behaved irreversibly and therefore only the thermodynamics of the Cr/Cr_2O_3 system are discussed here.

Jeannin et al.[171] investigated the free energy of formation of Cr_2O_3 by equilibrating Cr/Cr_2O_3 samples with H_2/H_2O mixtures in the temperature range 1040-1300°C. They reported that:

$$\Delta G^\circ_{(2.34)} = -266700 + 59.95\ T(\pm 300)\ \text{cal} \qquad (2.40)$$

This equation gives values in the above temperature range approximately 2000 cal higher than the values of the free energy of formation of Cr_2O_3 tabulated by Elliott and Gleiser[25].

Tretjakov and Schmalzried[96], and Pugliese and Fitterer[97] used a solid electrolyte technique to determine the free energy of formation of Cr_2O_3. CSZ was used as a solid electrolyte and air as the reference electrode. They reported:

$$\Delta G^\circ_{(2.39)} = -258600 + 55.2\ T\ (\pm 300)\ \text{cal} \qquad (2.41)$$
$$(1000 - 1500°K)$$

and

$$\Delta G^\circ_{(2.39)} = -263590 + 59.6\ T\ \text{cal} \qquad (2.42)$$
$$(1000 - 1500°K)$$

respectively.

These values agree well at 1000°K but they differ substantially at higher temperatures. Recently Pehlke et al.[98] measured the free energy of formation of Cr_2O_3 using a ThO_2-Y_2O_3 solid electrolyte and Co/CoO and Mn/MnO as reference

electrodes. They report reproducible results in agreement with Jeannin et al.

$$\Delta G^{\circ}_{(2.39)} = -266600 + 59.78\ T\ (\pm 300)\ \text{cal} \qquad (2.43)$$
$$[1148^{\circ}K - 1523^{\circ}K]$$

In Table 2.1 values of $\Delta G^{\circ}_{(2.39)}$ up to 1500 K are given as calculated by several investigators. The disagreement of the data of Tretjakov and Schmalzried as well as Pugliese and Fitterer with data of Pehlke et al. and Jeannin et al. is attributed to electronic conduction in the calcia stabilised zirconia employed. In this study, the expression reported by Jeannin et al. was adopted. Their results were extrapolated at steelmaking temperatures. From equation (2.40) the partial pressure of oxygen in equilibrium with Cr/Cr_2O_3 is calculated as:

$$\log P_{O_2}(Cr/Cr_2O_3) = -\frac{38900}{T} + 8.74 \qquad (2.44)$$

TABLE 2.1

Free energy of formation of Cr_2O_3

	ΔG°_f (Cr_2O_3) cal				
T°K	Elliott & Gleiser[25]	Tretjakov & Schmalzried[96]	Pugliese & Fitterer[97]	Jeannin et al.[171]	Pehlke et al.[98]
1000	-209150	-203400	-204000	-206700	-206840
1100	-203000	-197900	-198000	-200800	-200825
1200	-196900	-192400	-192100	-194800	-194810
1300	-190800	-186800	-186100	-188800	-188795
1400	-184700	-181300	-180100	-182800	-182780
1500	-178600	-175800	-174200	-176800	-176765

C. Deoxidation studies in the Fe-Nb-O, Fe-Al-O, Fe-Al-Mn-O and Fe-Ti-O systems

2.14 Equilibrium in the Fe-Nb-O system

Elle and Chipman[99] studied the Fe-Nb-O system at 1600°C. They equilibrated a molten Fe-Nb alloy with H_2/H_2O mixture of known oxygen potential. After quenching the melt, they analysed for niobium and oxygen and identified the oxide formed, as NbO_2 by X-ray powder diffraction in the range 0.76 - 1.61 % Nb.

They report a value of ΔG° equal to 30300 cal at 1600°C for the reaction:

$$NbO_{2(s)} \rightleftarrows \underline{Nb}\ \text{lw/o} + 2\underline{O}\ \text{lw/o} \qquad (2.45)$$

In trying to determine the temperature dependence of the deoxidation equilibrium, they used the free energy of formation data of NbO_2 as estimated by Coughlin[95]:

$$Nb_{(s)} + O_{2(g)} \rightleftarrows NbO_{2(s)} \qquad (2.46)$$

$$\Delta G^\circ_{(2.46)} = -187000 + 40.2\ T\ \text{cal.} \qquad (2.47)$$

for temperatures around 1900°K.

The estimated value for the free energy of fusion of niobium[25]:

$$Nb_{(s)} \rightleftarrows Nb_{(\ell)} \qquad (2.48)$$

$$\Delta G^\circ_{(2.48)} = 6300 - 2.3\ T\ \text{cal.} \qquad (2.49)$$

was combined with equation (2.47) together with data for the solution of O_2 into iron[16] to give the standard free energy change for the reaction:

$$Nb_{(\ell)} + 2\underline{O}_{1w/o} \rightleftarrows NbO_{2(s)} \quad (2.50)$$

$$\Delta G^{\circ}_{(2.50)} = -137000 + 43.9\ T \text{ cal.} \quad (2.51)$$

Using their high temperature results and equation (2.51), and assuming regular behaviour for solutions of Nb in Fe, they calculated a value of the corresponding free energy of solution:

$$Nb_{(\ell)} \rightleftarrows \underline{Nb}_{1w/o} \quad (2.52)$$

$$\Delta G^{\circ}_{(2.52)} = -50100 - 10.16\ T \text{ cal.} \quad (2.53)$$

Equations (2.51) and (2.53) were then combined to give:

$$NbO_{2(s)} \rightleftarrows \underline{Nb}_{1w/o} + 2\underline{O}_{1w/o} \quad (2.54)$$

$$\Delta G^{\circ}_{(2.54)} = 131600 - 54.1\ T \text{ cal.} \quad (2.55)$$

Equation (2.55) yields:

$$\log K_{(2.54)} = \log h_{Nb} \cdot h_O^2 = -\frac{28780}{T} + 11.93 \quad (2.56)$$

It should be mentioned here that the results of Elle and Chipman, apart from the errors in the estimated values used in their calculation, might involve some additional errors due to interaction of the melt with the crucibles used. MgO and Al_2O_3 crucibles were used with unsatisfactory results and the silica crucibles finally used, introduced some silicon into the melt, thus necessitating some uncertain but small correction for its effects on the activity of the other solutes. The authors did correct their results for silicon, taking $\log f_O^{Si} = -0.14\ (\%Si)$, but the resulting scatter in their estimation of $\log f_O^{Nb}$ versus (%Nb) suggests some uncertainty in the estimations of h_{Nb} which is used to determine

the equilibrium constant, equation (2.56).

Sato et al.[100] studied equilibria in the Fe-Nb-O system with H_2O/H_2 mixtures. For niobium contents between 1 and 2% they identified NbO_2 as the deoxidation product and determined a value for $K_{(2.54)}$ of $2.23\ 10^{-4}$ at 1600°C. Narita and Koyama[27,101] studied the same system again using H_2O/H_2 mixtures. They used alumina, and in some cases silica, crucibles to melt the iron, in a high frequency induction furnace. Samples were taken from the liquid melt using a silica tube, or in some cases, the whole melt was quenched under argon and samples taken from the solidified ingot. The deoxidation products were identified by electron and X-ray diffraction techniques.

For Nb contents between 0.4 and 5% they found tetragonal NbO_2 as the only deoxidation product. For Nb contents less than 0.4% they did identify the product as $FeO.Nb_2O_5$ and concluded therefore that columbite exists as an equilibrium oxide at low niobium contents.

Their data may be represented as follows:

$$NbO_{2\,(s)} \rightleftharpoons \underline{Nb}_{\text{1w/o}} + 2\underline{O}_{\text{1w/o}} \qquad (2.54)$$

$$\log K_{(2.54)} = -\frac{32780}{T} + 13.917 \qquad (2.57)$$

$$FeO.Nb_2O_{5\,(s)} \rightleftharpoons Fe_{(\ell)} + 6\underline{O}_{\text{1w/o}} + 2\underline{Nb}_{\text{1w/o}} \qquad (2.58)$$

$$\log K_{(2.58)} = -\frac{88300}{T} + 36.76 \qquad (2.59)$$

The authors state that although $FeNbO_3$ would be theoretically

expected as a phase in between NbO_2 and $FeO.Nb_2O_5$, they could not identify such a product.

Fisher and Janke[109] used a stabilised zirconia cell and air as the reference electrode to measure oxygen activities in iron melts containing niobium. They report:

$$\log f_O^{Nb} = -0.066[\%Nb] \qquad (2.60)$$

Teblitsky and Vladimirov[103] calculated the equilibrium constant for reaction (2.54) as:

$$\log K_{(2.54)} = -\frac{27530}{T} + 10.89 \qquad (2.61)$$

and finally Buzek et al.[104] as reported by Jaquemont et al.[8] give:

$$K_{(2.54)} = 1.7\ 10^{-4} \text{ at } 1600°C.$$

All these results are summarised in Table 2.2.

TABLE 2.2

Studies of the Fe-Nb-O liquid system

Author	Nb%	Oxide formed	log K deoxidation	K_{1600} deoxidation
Elle & Chipman[99]	0.76-1.61	NbO_2	$-\frac{28780}{T} + 11.83$	$2.9\ 10^{-4}$
Sato et al[100]	1-2	NbO_2		$2.33\ 10^{-4}$
Narita and Koyama[101]	<0.4	$FeNb_2O_6$	$-\frac{88300}{T} + 36.76$	$4.1\ 10^{-11}$
	0.4-5.0	NbO_2	$-\frac{32780}{T} + 13.917$	$2.6\ 10^{-4}$
Teplitsky and Vladimirov[103]		NbO_2	$-\frac{27530}{T} + 10.89$	$1.5\ 10^{-4}$
Buzek et al[104]	1.5-3.2	NbO_2		$1.7\ 10^{-4}$

2.15 The system Nb-O

Fig. 2.7 shows the equilibrium phase diagram[105] for the Nb-O system as it has been determined from metallographic, X-ray and incipient melting studies on alloys made from electron gun refined Nb, and Nb_2O_5 of 99.9% purity. Three oxides, NbO, NbO_2 and Nb_2O_5 are reported. However, Nb_2O_5 is not stable at steelmaking temperatures. Elliott[105] in reviewing this system, reports several studies at lower temperatures where the existence of two suboxides NbO_x and NbO_y is reported at temperatures between 300 and 500°C.

NbO has a cubic structure while NbO_2 is tetragonal. Nb_2O_5 is polymorphic and has a range of non-stoichiometry. Its defect structure involves oxygen vacancies. Blumenthal et al.[106] studied the thermodynamics of nonstoichiometric niobium pentoxide employing electrochemical cell measurements with calcia stabilised zirconia. They defined the range of nonstoichiometry in Nb_2O_{5-x} between 890°-1090°C as: $5-x = 4.887$ at 890°C to 4.841 at 1090°C.

Wicks and Block[107] have reviewed the thermodynamic properties of Nb, NbO_2 and Nb_2O_5, and Barin and Knacke[108] have reported thermodynamic properties for Nb, NbO, NbO_2 and Nb_2O_5.

Ignatowicz and Davies[109] studied the free energy of formation of NbO using an electrochemical cell with ThO_2 + 1% Y_2O_3 as solid electrolyte and Fe/FeO as the reference electrode in the temperature range 800 - 1100°C. For the reaction:

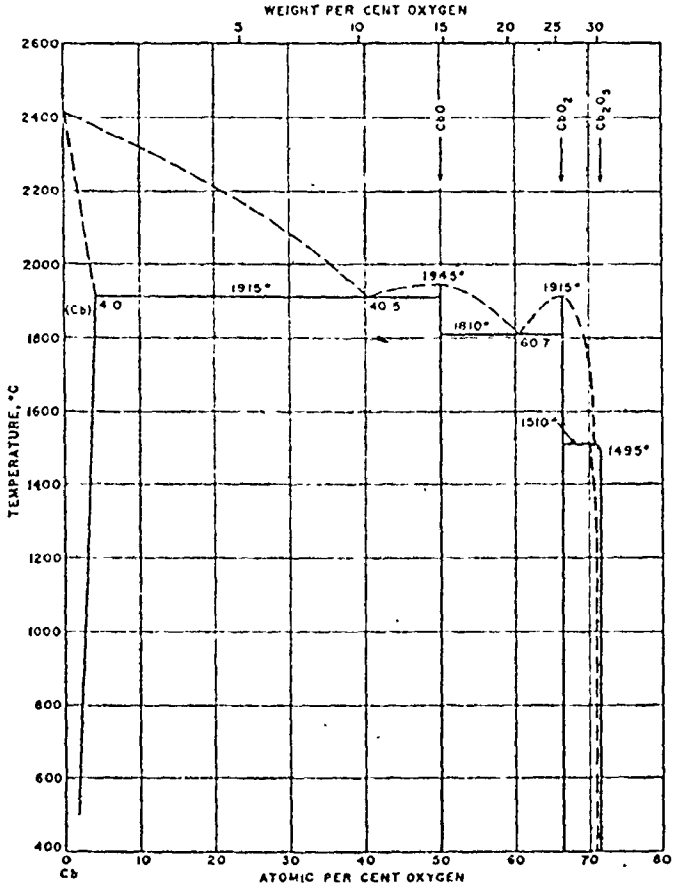

Figure 2.7 The Nb-O phase diagram
(From ref. 105)

$$Nb_{(s)} + \frac{1}{2}O_{2(g)} \rightleftarrows NbO_{(s)} \qquad (2.62)$$

$$\Delta G^{\circ}_{(2.62)} = -98830 + 20.57\ T\ cal. \qquad (2.63)$$

These results agree well with experimental results reported by Drobyshev and Rezukhina but differ slightly from those reported by Steele and Alcock[90].

The data of Worell[110] for the same reaction are in reasonable agreement with the Ignatowicz and Davies data and for this reason, the data given by equation (2.63) are used in the present work (section 5.4).

2.16 Equilibrium in the Fe-Al-O system

As aluminum is used extensively for steel deoxidation, many studies on the Fe-Al-O system have been reported. Ghosh[111] has given an excellent review of studies in this system. Al_2O_3 has been reported to be the only deoxidation product by most researchers. The determination of the free energy change for the reaction:

$$Al_2O_3(s) \rightleftarrows 2\underline{Al}_{\text{1w/o}} + 3\underline{O}_{\text{1w/o}} \qquad (2.64)$$

the deoxidation constant for which is given by:

$$K_{(2.64)} = h^2_{Al}\ h^3_O \qquad (2.65)$$

has been the subject of many publications. In quite a few of the studies, especially the earlier ones, a quasi "deoxidation constant":

$$K'_{(2.64)} = [\%Al]^2\ [\%O]^3 \qquad (2.66)$$

has been determined by analysing the oxygen and aluminum content of iron in equilibrium with Al_2O_3. However, as the

interaction between a strong deoxidiser such as aluminum and oxygen in iron cannot be neglected, this "constant" varies with aluminum content at a constant temperature. In early studies of the Fe-Al-O system, it was recognised that, depending on the amount of aluminum in iron, the deoxidation product could be $FeAl_2O_4$ or mixtures of Al_2O_3 and $FeAl_2O_4$.

The determination of the free energy change for the reaction:

$$FeAl_2O_{4(s)} \rightleftarrows Fe_{(\ell)} + 2\underline{Al}_{\text{1w/o}} + 4\underline{O}_{\text{1w/o}} \qquad (2.67)$$

has been reported and values of the deoxidation constant

$$K_{(2.67)} = h_{Al}^2 . h_O^4 \qquad (2.68)$$

as well as the quasi "deoxidation constant"

$$K'_{(2.67)} = [\%Al]^2 \ [\%O]^4 \qquad (2.69)$$

have been determined.

In the following subsection the experimental determination of $K'_{(2.64)}$, $K_{(2.64)}$, $K''_{(2.67)}$ and $K_{(2.67)}$ are discussed.

2.16.1 Experimental determinations of the deoxidation "constant" $K'_{(2.64)}$

The determinations of the "constant" $K'_{(2.64)}$ reported in the literature are summarised in Table 2.3.

Hassenbruch[112] and Herty et al.[113] carried out the first experimental determination, and a more systematic study followed by Wentrub and Hieber[114]. Here, aluminum was added to liquid iron with a high oxygen content under air at reduced pressure (10-20 Torr). Samples of the melt

TABLE 2.3

Experimental values of deoxidation constant $K'_{(2.64)} = [\%Al]^2\ [\%O]^3$

Authors	%Aluminum into solution	log K'	$K'_{1873°K}$
Hassenbruch[112]			$\approx 10^{-9}$
Herty et al.[113]			6.3×10^{-9}
Wentrup and Hieber[114]		$-\frac{71200}{T} + 27.98$	0.9×10^{-10}
Hilty and Crafts (115)	<1	$-\frac{58600}{T} + 22.75$	2.91×10^{-9}
Repetylo et al.[116]	0.003		5×10^{-13}
Swisher[117]	<20	$-\frac{45500}{T} + 11.55$	$\approx 10^{-13}$ (1853°)
Rohde et al.[126]			3.5×10^{-11} without slag 7.1×10^{-14} with slag
Geller and Dicke (120)		$-\frac{58600}{T} + 18.90$	4.1×10^{-13}
Shibata and Yagihashi[122]		$-\frac{12675}{T} - 2.85$	2.4×10^{-10}
Braun et al.[127]			5×10^{-14}

were analysed for total aluminum and oxygen, assuming that all alumina inclusions were in solution at the experimental temperature. Their results show a considerable scatter and the sources of errors present are basically, the highly oxidising atmosphere resulting in a higher oxygen content in the steel, the possibility of the melt not being in equilibrium due to the short equilibration time (10 min.), the inaccurate temperature measurement and finally, the difficulties in analysing small quantities of aluminum and oxygen in iron accurately.

Hilty and Crafts[115] studied the solubility of oxygen in liquid iron containing aluminum in an inert argon atmosphere, using a rotating induction furnace. Their results showed a very high scatter, the deoxidation "constant" $K'_{(2.64)}$ varying by a factor of 50. X-ray analysis of the deoxidation product showed the existence of hercynite. Although their melts were clearly not in equilibrium with alumina, they expressed their results in terms of the product $[\%Al]^2\ [\%O]^3$.

The same authors studied the influence of manganese in the solubility of oxygen in Fe-Al-Mn melts and found a great increase in the deoxidising power of aluminum. Repetylo et al.[116] tried to understand why the deoxidation "constants" obtained by Hilty and Crafts and from most industrial experiments were so different from deoxidation constants obtained from thermochemical data ($K = 10^{-14}$ at 1600°C). They performed some kinetic experiments, under an

argon atmosphere, by adding aluminum to an iron melt containing oxygen and taking samples for analysis at convenient intervals. Although the lowest value of the product $[\%Al]^2\ [\%O]^3 = K'_{(2.64)}$, was 5×10^{-13}, the true K' is probably lower than this value since it is almost impossible to sample from a completely clean melt.

Experiments by the same authors were carried out under oxidising atmospheres. The average value of K' thus obtained was 10^{-9}, in good agreement with industrial practice. This difference in results is attributed to the formation of an alumina suspension which is produced continuously by reaction with oxygen.

Swisher[117] used melts with Al contents as high as 10% and reported values of $K'_{(2.64)}$ at 1580°C. The value of K' at 0.01% Al was then combined with the data of Gocken and Chipman[118] and d'Entermont et al.[119] to yield the temperature dependence given in Table 2.3. Swisher used a vacuum fusion technique to analyse for oxygen at very low levels (<10 ppm), i.e. close to the limits of analysis of this method. Moreover as pointed out by d'Entermont et al.[119] and Fruehan[24], the vacuum fusion technique is not suitable for oxygen analysis at high aluminum levels because of absorption of gas by the aluminum distilled from the sample, and vaporisation of Al_2O which condenses at lower temperatures. Because of the difficulties in accurately analysing the low levels of oxygen in equilibrium with aluminum in iron, some workers have used the C-O equilibrium:

$$\underline{C}_{\text{lw/o}} + \underline{O}_{\text{lw/o}} \rightleftarrows CO_{(g)} \qquad (2.70)$$

to calculate the oxygen content of iron in equilibrium with Al and C in solution. Geller and Dicke[120] studied the equilibrium:

$$3\underline{C}_{\text{lw/o}} + Al_2O_{3(s)} \rightleftarrows 2\underline{Al}_{\text{lw/o}} + 3CO_{(g)} \qquad (2.71)$$

$$K_{(2.71)} = \frac{h_{Al}^2}{h_C^3} = \frac{(\%Al)^2 f_{Al}^2}{(\%C)^3 f_C^3} \quad (P_{CO} = 1 \text{ atm}) \qquad (2.72)$$

Using the inaccurate assumption that the activity coefficients f_{Al}, f_O, f_C are all unity and, combining their results with the data for the C-O equilibrium (eqn. 2.70) published by Geller[121], they obtained:

$$K'_{(2.64)} = [\%Al]^2\ [\%O]^3 = \frac{K'_{(2.71)}}{K'_{(2.70)}}$$

Their results are included in Table 2.3.

Yagihashi and Shibata[122] equilibrated carbon saturated iron containing about 2% Al with CO gas. Their data were analysed as in reference 120 and their results are presented in Table 2.3. Again, concentrations rather than activity were used, introducing a considerable error because of the high solute concentration.

2.16.2 Experimental determination of the deoxidation constant $K_{(2.64)}$

In table 2.4 all the determinations of the constant $K_{(2.64)}$ are summarised.

Gocken and Chipman[118] equilibrated iron, containing an initial charge of aluminum, in alumina crucibles under

TABLE 2.4

Experimental values of Equilibrium constant $K=h_{Al}^2 h_O^3$

Authors	% Aluminum in solution	logK	$K_{1873°K}$	e_O^{Al} at 1873°K
Gocken and Chipman[118]	<0.1	$-\frac{64000}{T} + 20.48$	2.0×10^{-14}	-12
McLean and Bell[123]	<1	$-\frac{60300}{T} + 18.6$	2.5×10^{-14}	-4.6
d'Entremont et al.[119]	<2	$\frac{38200}{T} + 7.8$	2.5×10^{-13}	-1.0
Buzek[124]	<1.25		3.2×10^{-14}	-1.15
Schenck et al.[125]	10^{-3}	$-\frac{49500}{T} + 17.21$	7.1×10^{-10} Precipitation experiments	-0.22
			3.3×10^{-12} Reduction with CO	--
Rohde et al.[126]	<3	$-\frac{64000}{T} + 20.57$	2.7×10^{-14}	-1.17
Chipman and Langenberg[128]			3.6×10^{-14}	--
Sawamura et al.[129]		$-\frac{62500}{T} + 19.70$	2.1×10^{-14}	--
Fruehan[24]	<0.4		5.6×10^{-14}	-3.90
Jaquemont et al.[130]	<2		1.2×10^{-13}	--

controlled atmospheres of H_2O and H_2. Based on the results of analysis for aluminum and oxygen, they determined $e_O^{Al} = -12$ at 1600°C. They then determined $K_{(2.64)}$ from $K'_{(2.64)}$ using this interaction coefficient and assuming that f_O^O and f_{Al}^{Al} are equal to unity. The result agrees fairly well with thermochemical data.

McLean and Bell[123] redetermined the equilibrium constant $K_{(2.64)}$ and the solution thermodynamics of the Fe-Al-O system, using the same method as Gocken and Chipman, except that they diluted their H_2O/H_2 mixtures with Argon in order to reduce errors caused by thermal diffusion. The value of the interaction parameter e_O^{Al} calculated, was -4.6 which does not agree with that of Gocken and Chipman. D'Entremont et al.[119] redetermined the Al-O interaction coefficient in iron containing larger quantities of Al, equilibrating Fe-Al melts in alumina crucibles at 1740° and 1910°C, under argon atmospheres. Their value of e_O^{Al} is -1. Buzek[124] also determined e_O^{Al} using the same technique and obtained a value of -1.15 at 1600°C. Since interaction parameters cannot account for the large difference in values of $K'_{(2.64)}$, Schenck[125] claimed that a large supersaturation of aluminum and oxygen is necessary to nucleate alumina particles in liquid iron, thus preventing the bath from reaching equilibrium. However, the reverse process, reduction of alumina, should reach equilibrium. Calculation of logK from reduction experiments they performed, led to an average value of -11.48 at 1600°C which is still larger than the thermochemical value, logK = -13.24.

Rohde et al.[126] carried out aluminum deoxidation experiments with and without an alumina saturated lime-alumina slag. Argon was used to stir the melt and the slag, scavenged the inclusions. The scatter in the results from runs without the slag was much greater than those with the slag. From the variation of $\log K'_{(2.64)}$ with aluminum content (runs with slag), values of $e_O^{Al} = -1.17$ and $K_{(2.64)} = 2.7 \times 10^{-14}$ were obtained at 1600°C. The authors conclude that the difference in the value of the deoxidation constant between runs with and without slag is partly caused by an alumina suspension in the melt. They also concluded that fine particles remained in the melt even after slag treatment. Braun et al.[127] showed that long times are essential for equilibrium conditions to be attained and that mechanical stirring is necessary if sampling is to be made from a clean melt. They obtained the value $K'_{(2.64)} = 5 \times 10^{-14}$ at 1600°C, which is very close to that derived from thermochemical data, even witnout the use of activity coefficients.

Chipman and Langenberg[128] have indirectly determined aluminum and oxygen activities rather than concentrations by calibrating alumina saturated Al_2O_3-SiO_2-CaO slags with graphite saturated Fe-C-Si-Al melts under CO atmospheres at 1600° and 1700°C. They analysed the slag for its constituents, the metal for silicon and aluminum, and obtained h_O from the relation:

$$\log h_O = -\frac{37.2}{T} - 4.29 \qquad (2.73)$$

for the reaction $C_{(gr)} + \underline{O}$ lw/o $\rightleftharpoons CO_{(g)}$.

The value of h_{Al} was obtained from the known effects of carbon and silicon on f_{Al} and they obtained $K_{(2.64)} = 3.6 \times 10^{-14}$ at 1600°C and 2.8×10^{-13} at 1700°C. This technique has the advantages (a) of high aluminum content thus minimising the uncertainty in aluminum analysis, (b) of accurate oxygen potentials and (c) minimisation of melt contamination with Al_2O_3, because of the very little oxygen involved.

Sawamura et al.[129] have used recent data for the C-O equilibrium and various interaction coefficients to calculate equilibrium activities of aluminum and oxygen from the data of Geller and Dicke. Their results are in good agreement with thermochemical data. Electrochemical methods have been employed in determination of the oxygen activity in equilibrium with iron-aluminum melts.

Fruehan[24] and Jacquemont et al.[130] have used ThO_2-Y_2O_3 solid electrolytes in the electrochemical cell:

$$Cr_{(s)}\text{-}Cr_2O_{3(s)} \,|\, ThO_2\text{-}Y_2O_3 \,|\, Fe\text{-}Al\text{-}O_{(\ell)},\ Al_2O_{3(s)} \qquad (2.74)$$

Fruehan[24] limited his aluminum content in iron to 1.14% in order to avoid electronic conduction in the electrolyte. He calculated $K = h_{Al}^2 . h_O^3 = 5.6 \times 10^{-14}$ at 1600°C and also found $e_O^{Al} = -3.90$ and $\log f_{Al}^O = -1.68$ at 1600°C.

Jaquemont et al.[130] corrected for the partial electronic conductivity of their cell using a relation given by Schmalzried[131]. They obtained $K = 1.2 \times 10^{-13}$ at 1600°C.

2.16.3 Experimental determination of $K'_{(2.67)}$ and $K_{(2.67)}$

Pillay et al.[132] determined the free energy of formation of the spinel $FeAl_2O_4$ from its constituent oxides

in the temperature range 1500° to 1700°C. Liquid iron was held in a pure corundum crucible in an atmosphere of water vapor and hydrogen of controlled composition, for a prolonged period. It was then quenched and analysed for oxygen. The occurrence of hercynite was determined by inspection of the crucible after the run. They determined the free energy change for the reaction:

$$FeAl_2O_{4(s)} + H_{2(g)} \rightleftarrows Al_2O_{3(s)} + Fe_{(\ell)} + H_2O_{(g)} \qquad (2.75)$$

as

$$\Delta G^\circ_{(2.75)} = +5260 - 0.32\ T\ cal \qquad (2.76)$$

Combining equation (2.76) with data for the free energy of formation of water vapor given by Floridis and Chipman, they o obtained:

$$FeAl_2O_{4(s)} \rightleftarrows Fe_{(\ell)} + Al_2O_{3(s)} + \tfrac{1}{2}O_{2(g)} \qquad (2.77)$$

$$\Delta G^\circ_{(2.77)} = +65460 - 14.26T\ cal \qquad (2.78)$$

Equation (2.78) can be combined with equation (2.21) to give ΔG° for the equilibrium between hercynite, alumina and oxygen in liquid iron, equation (2.67). Values of $K_{(2.67)}$ are given in Table 2.5.

McLean and Ward[133] equilibrated liquid iron in alumina crucibles containing synthetic hercynite. In some melts hercynite was not added, but the iron was superoxidised to ensure an oxygen potential higher than that required for hercynite formation. The melt after equilibration was quenched in a helium stream and the oxygen content of the

TABLE 2.5

EXPERIMENTAL VALUES FOR HERCYNITE FORMATION

Authors	Reaction	ΔG°_T (cal/mole)	ΔG°_T for reaction $FeAl_2O_{4(s)} \rightleftarrows Fe_{(\ell)} + 2Al_{lw/o} + 4\underline{O}_{lw/o}$ (cal/mole)	$\log K_{Hercynite}$	$K_{1600°C\ Hercynite}$
Pillay et al.[132]	$FeAl_2O_{4(s)} \rightleftarrows Fe_{(\ell)} + Al_2O_{3(s)} + \frac{1}{2}O_{(g)}$	65460-14.26T	324842-110.38T	$-\frac{70347}{T} + 24.13$	-13.43
McLean and Ward[133]	$FeAl_2O_{4(s)} \rightleftarrows Fe_{(\ell)} + Al_2O_{3(s)} + \underline{O}_{lw/o}$	34950-12.99T	319333-108.33T	$-\frac{69800}{T} + 23.68$	-13.59
Chan et al.[134]	$FeAl_2O_{4(s)} \rightleftarrows Fe_{(\ell)} + Al_2O_{3(s)} + \frac{1}{2}O_{2(g)}$	73195-18.24T	329577-114.36T	$-\frac{72038}{T} + 25.0$	-13.46
Kim and McLean[173]	$FeAl_2O_{4(s)} \rightleftarrows Fe_{(\ell)} + Al_2O_{3(s)} + \underline{O}_{lw/o}$	43810-18.21T	328192-113.64T	$-\frac{71736}{T} + 24.84$	-13.46

samples was analysed by a vacuum fusion technique. Assuming Henrian behaviour of oxygen in the melt, they found for the reaction:

$$FeAl_2O_{4(s)} \rightleftarrows Fe_{(\ell)} + \underline{O}_{1w/o} + Al_2O_{3(s)} \quad (2.79)$$

$$\log K_{(2.79)} = \log[\%O] = -\frac{7640}{T} + 2.84 \quad (2.80)$$

Using a value of $\log K_{(2.64)} = -\frac{64090}{T} + 20.41$ they then determined for the reaction:

$$FeAl_2O_{4(s)} \rightleftarrows Fe_{(\ell)} + 2\underline{Al}_{1w/o} + 4\underline{O}_{1w/o} \quad (2.67)$$

$$\log K_{(2.67)} = -\frac{71730}{T} + 23.25 \quad (2.81)$$

For the reaction (2.77), using Tankins'[17] data, they determined:

$$\Delta G^\circ_{(2.77)} = 63910 - 12.54T \text{ cal} \quad (2.82)$$

Chan et al.[134] determined the oxygen potential for the system iron-alumina-hercynite in the temperature range 750° to 1600°C. They employed electrochemical cells of the type:

$$Mo_{(s)} - MoO_{2(s)} \left| \begin{matrix} CaO\text{-}ZrO_2 \\ \text{or} \\ CaO\text{-}ZrO_2 \\ ThO_2\text{-}Y_2O_3 \end{matrix} \right| + Fe_{(s,\ell)}, Al_2O_{3(s)}, FeAl_2O_{4(s)} \quad (2.83)$$

to determine ΔG°_T for the reaction:

$$FeAl_2O_{4(s)} \rightleftarrows Fe_{(s,\ell)} + \tfrac{1}{2}O_2(g) + Al_2O_{3(s)} \quad (2.84)$$

$$\Delta G^\circ_{(2.84)} = 69895 - 16.42T(\pm 300) \text{ cal } (750\text{-}1536°C) \quad (2.85)$$

$$\Delta G^{\circ}_{(2.84)} = 73195 - 16.24T\ (\pm 300)\ \text{cal}\ (1536\text{-}1700^{\circ}C) \quad (2.86)$$

These results are in excellent agreement with Pillay et al. but differ significantly from the results of McLean and Ward.

Recently, Kim and McLean[173] redetermined the oxygen activity in equilibrium with alumina and hercynite in liquid iron using the same technique as in reference 133, and gave new values of $K_{(2.77)}$ and $K_{(2.67)}$. Their results agree very well with results of Chan et al.. It is reported that Novokatsky and Belov[135] equilibrated Fe-Al melts with Al_2O_3-FeO mixtures. They determined hercynite as the equilibrium phase for $0.001\% < Al < 0.007\%$ and concluded that:

$$\log K'_{(2.67)} = -\frac{59570}{T} + 22.49 \quad (2.87)$$

Tretjakov and Schmalzried[96] used stabilised zirconia in electrochemical cells, to determine the equilibrium oxygen partial pressures for the reaction:

$$FeAl_2O_{4(s)} \rightleftarrows Al_2O_{3(s)} + FeO_{(s)} \quad (2.88)$$

At 1000°C they reported: $\Delta G^{\circ}_{(2.85)} = -5.7 \pm 0.2$ Kcal.

As it can be seen, values of $K'_{(2.87)}$ have not been independently determined. Their values depend not only on results for the equilibrium (2.79) but also on the values chosen for $K_{(2.64)}$ or $K'_{(2.64)}$. This complicates even more the process of comparing the different values of $K_{(2.67)}$. The best way for doing so would be to compare values for the equilibrium (2.79) and then calculate $K_{(2.67)}$ using the "best" value for $K_{(2.64)}$. This by itself is difficult as there are

large differences in reported values for $K_{(2.64)}$.

Ghosh[111] tried to resolve the discrepancies in the reported values for the free energy of formation of alumina, in the temperature range 1700°-1850°K. Using high temperature electrochemical cells of the types:

$$Pt_{(s)}, Al_{(\ell)} \left| Al_2O_3 \text{ in } CaF_2 \right| O_2(g), Pt_{(s)} \qquad (2.89)$$

$$C_{(gr)}, Al_{(\ell)} \left| Al_2O_3{}_{(s)} \right| \begin{matrix}\text{Electrolyte} \\ \text{containing} \\ O^{2-}\end{matrix} \left| Al_2O_3{}_{(s)} \right| \begin{matrix}\text{Fe-C} \\ \text{sat'd}\end{matrix}, CO(g), C_{(gr)} \qquad (2.90)$$

he obtained:

$$\Delta G^\circ_f(Al_2O_3) = -398{,}560 + 80.02T(\pm 1800)\frac{cal}{mol} \qquad (2.91)$$

Although his results are 3.3% more positive than the generally accepted thermochemical value at 1800°K, he argues rather convincingly, that his are the correct values. Evidence supporting his value of $\Delta G^\circ_f(Al_2O_3)$ is obtained from mineralogical data..

Ghosh also determined values of $K_{(2.64)}$ using his ΔG°_f data:

$$\log K_{(2.64)} = -\frac{62160}{T} + 20.86 \qquad (2.92)$$

His value agrees well with Jaquemont et al.[130], the most recent work in this system.

Equation (2.92) has been used in the present work in combination with values for $K_{(2.79)}$ reported by several authors, to give the values of $K_{(2.67)}$ given in Table 2.5.

2.17 The Al-O system

Although the existence of compounds such as AlO, Al_2O have been reported[105], the stable deoxidation product in steelmaking is Al_2O_3. Numerous attempts have been made to determine its free energy of formation and, although most of them are studies in the system Fe-Al-O, which have already been reviewed, there is a number of determinations using thermochemical methods.

Ghosh[111] has reviewed all these investigations. Table 2.6 has been taken from Ref. 111 and summarises the results from thermochemical studies. The importance of the choice of ΔH°_{298} in the calculation of $\Delta G_{f(Al_2O_3)}$ is apparent in Table 2.6.

Ghosh[111] has given an exhaustive analysis of the accuracy of these values and further assessment of these values will not be attempted here.

2.18 The free energy of solution of aluminum

In order to calculate the free energy change for the reaction

$$Al_{(\ell)} \rightleftarrows \underline{Al}_{1w/o} \qquad (2.93)$$

the slope of the Henry's low line, γ°_{Al} in the Fe-Al system is required.

Distribution ratios of aluminum between liquid iron and liquid silver can be measured and the activity of Al in iron can be found by determining the activity of Al in liquid silver.

Studies in the system Al-Ag have appeared[142,143]

TABLE 2.6

The standard free energy of formation of Alumina

ΔG°_T from Thermochemical Data

Authors	ΔH°_{298} used Kcal/mole	ΔG°_T cal/mole	Range °K
Treadwell and Terebesi[136]	-293.2	-396678 + 78.17T	930-2320
Chipman[137]	?	-399800 + 74.8T	930-2320
DeKay Thompson[138]	-388.1	-376000 + 61.56T	929-2073
Richardson and Jeffes[139]	?	-386250 + 66.45T	930-2318
Elliott et al.[25]	-400.4	-401500 + 79.91T	1500-2000
Wicks and Bloch[107]	-400.29	$-408660-2.69T\ \ln T - -0.78\times10^{-3}T^2 + 3.9\times10^{5}\,T^{-1} + 102.38T$	931-1300
Kubaschewski et al.[140]	-400.0	$-405760-3.75T\log T + 92.22T$	923-1800
JANAF[141]	-400.4	Approx. same as in (25)	1500-2000

which give values for γ^{o}_{Al}.

Electrochemical studies have been done[145] using the cell:

$$Al_{(\ell)} | Al^{3+} \text{ in } KCl\text{-}NaCl | Al\text{-}Ag_{(\ell)} \qquad (2.94)$$

in temperatures between 700° and 980°C.

To calculate the temperature dependence of γ_{Al}, the value of the partial molar heat of mixing of aluminum in iron is essential. This quantity has been determined by Woolley and Elliott[147] using a high temperature solution calorimeter at 1600°C. They calculated for reaction (2.93):

$$\Delta\bar{G}_{Al} = -15350-5.05T \text{ cal} \qquad (2.94)$$

Belton and Fruehan[148] have directly determined activities in the Fe-Al and Ag-Al systems at 1600°C using a mass spectrometer.

Finally, Fruehan[24] determined oxygen activities in the Fe-Al-O system using the oxygen cell (2.75). Using values of the free energy of formation of alumina given in reference 25, they obtained a value $\log\gamma^{o}_{Al} = -1.68$ at 1600°C, agreeing with the value of $\log\gamma^{o}_{Al} = -1.62$ determined by Belton and Fruehan.

All these results are summarised in Table 2.7.

TABLE 2.7

Free Energy Change for the Reaction $Al_{(\ell)} \rightleftarrows [Al]_{1w/o}$

Authors	Quantity	Value	$\Delta\bar{G}_{Al}$ cal/mole
Chipman[142]	γ°_{Al}	0.014	-15900 - 7.71T
Chipman and Floridis[143]	γ°_{Al}	0.031	-13000 - 7.71T
Hultgren et al.[144]	γ°_{Al}	0.035	-12500 - 7.71T
Wilder and Elliott[145]	γ°_{Al}	0.063	-10300 - 7.71T
Vachet et al.[146]	γ°_{Al}	0.053	-10970 - 7.71T
Woolley and Elliott[147] (and ref. 145)	ΔH^{M}_{Al}	-15350 cal/mole	-15350 - 5.05T
Belton and Fruehan[148]	γ°_{Al}	0.024	-15100 - 6.67T

2.19 Equilibrium in the Fe-Al-Mn-O system

Oelsen and Heynert[149] tried to establish the effect of manganese on the solubility of oxygen in Fe-Al-O melts. They equilibrated Fe-Al-Mn-O melts in corundum crucibles and analysed the slag and melt for their constituents.

An increase in the Mn content of the melt resulted in a corresponding decrease in oxygen content and an increase in the FeO/MnO ratio of the slag, the Al_2O_3 content remaining substantially constant. The authors presented results at different temperatures, the amount of oxygen in equilibrium with the melt, increasing with temperature at constant manganese content.

McLean[1], in a study of aluminate inclusion in continuously cast steel, concluded that the presence of manganese lowers the oxygen activity of the alumina/spinel transformation, the latter phase being a complex spinel of Fe and Mn, $(Fe,Mn)O.Al_2O_3$. The spinel composition should always lie on the line AB of Fig. 2.8, and it should shift towards composition B as the Mn content in steel increases.

Figures 2.9 and 2.10 are taken from McLean[1] and show the calculated effect of Mn on oxygen in equilibrium with alumina and aluminate spinel.

Recently Kim, McLean and Murray[150] reported results confirming the theoretical predictions of ref. 1. An induction furnace was used to equilibrate an iron or iron-manganese alloy contained in alumina crucible with and without the addition of synthetic non-manganese aluminates,

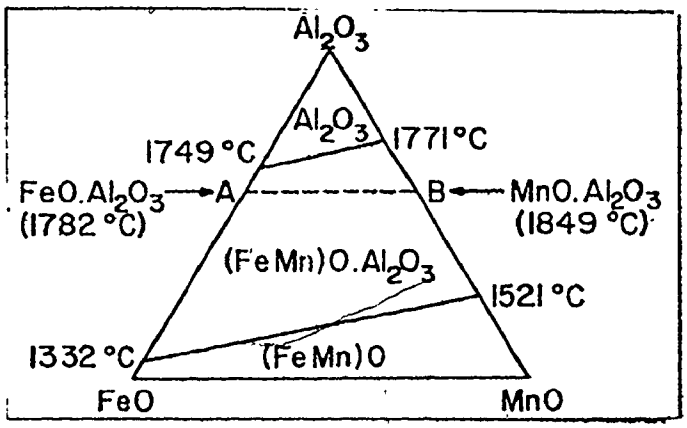

Figure 2.8 Region of spinel stability in the Fe-MnO-Al_2O_3 system (From ref. 1)

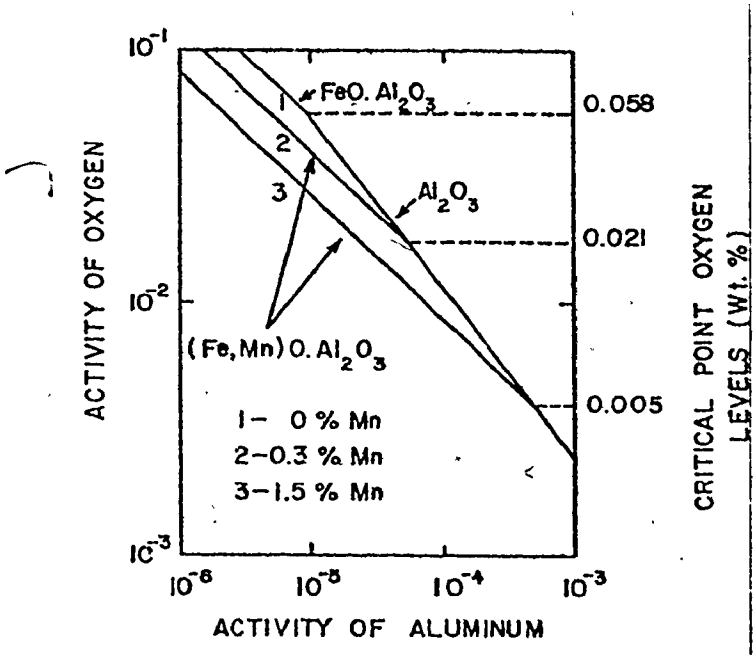

Figure 2.9 Effect of manganese at the deoxidation behavior of aluminum at 1600°C (From ref.1)

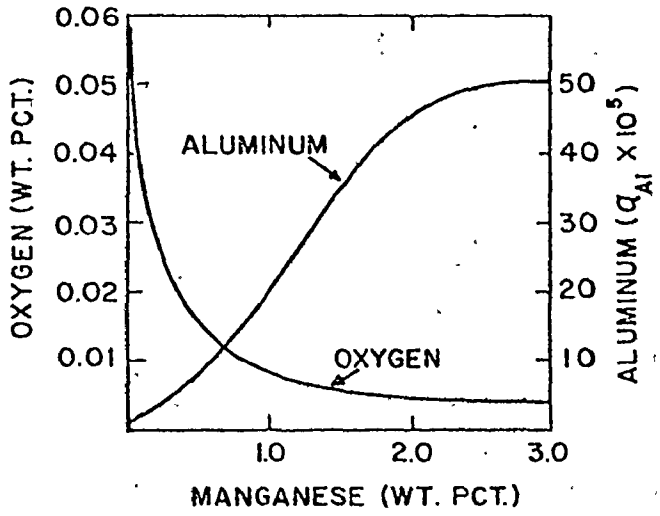

Figure 2.10 Effect of manganese on the aluminum and oxygen contents of liquid iron in equilibrium with alumina and aluminate spinel at 1600°C (From ref. 1)

under argon. Samples from the melts or from the solidified ingot were analysed for oxygen and manganese. The composition of thin films of spinel solid solution, formed as the alumina crucible walls, was determined by neutron activation analysis and by electron microprobe analysis. As predicted the oxygen content of the melt, decreased with increasing manganese content. For Mn content >2% the equilibrium oxygen content remained practically constant at a very low value which was dependent on the temperature. Although there could be some error in the analysis of manganese and oxygen in solution, due to the pressence of alumina and spinel inclusions, this should not be significant because of the experimental technique employed.

In the present study, the effect of manganese in the Fe-Al-O deoxidation system has been determined experimentally.

2.20 Equilibrium in the Fe-Ti-O system

There have been many studies in the Fe-Ti-O system, but even today, the nature of the deoxidation products and the conditions of their existence have not been resolved because of many conflicting results.

Wentrup and Hieber[151] equilibrated Fe-O melts containing Ti, under air at 1600°C and found inclusions of $FeO.TiO_2$ and Ti_2O_3 depending on the titanium content of the melt. Evans and Sloman[152] identified α-Ti_2O_3 as the principle deoxidation product but they also determined the existence of Ti_3O_5 and TiO_2 as the titanium content decreased.

Hadley and Derge[153] melted iron containing titanium under helium, into a TiO_2 crucible. They then took samples for analysis, either with a suction technique or from the solidified ingot. They concluded that the solubility of oxygen in the metal decreased to a minimum of between 0.002 and 0.004 wt% in the range 0.1 to 1.0% Ti.

The deoxidation phases they observed were mainly TiO_2 and Ti_2O_3 depending on the amount of Ti in the melt. These results along with those of other studies in the Fe-Ti-O systems, are summarised in Table 2.8. Liaudis and Samarin[154] added Ti to an Fe-O melt and, using a technique similar to that of Hadley and Derge, identified $2FeO.TiO_2$ and TiO_2 as the main deoxidation products. They also gave expressions for the ΔG°_T of the reactions:

$$2Fe.TiO_{2(s)} = \underline{Ti}_{1w/o} + 4\underline{O}_{1w/o} + 2Fe_{(\ell)} \qquad (2.95)$$

and

$$TiO_{2(s)} = \underline{Ti}_{1w/o} + 2\underline{O}_{1w/o} \qquad (2.96)$$

which are given in Table 2.8.

Chipman[155] using the results of ref. 153, calculated $e_O^{Ti} = -0.187$.

Chino et al.[156] used an Al_2O_3 crucible to equilibrate Fe containing Ti and oxygen. They analysed their samples for Ti, using a spectrophotometric method, and oxygen, using the inert gas fusion method.

In determining their deoxidation products by X-ray techniques, they used a "replica method" to extract the

TABLE 2.8

Summary of Results in the Fe-Ti-O system

Authors	Ti%	Oxide formed	$\log K = \log h_N^x h_O^y$	$K_{1600°}$	e_O^{Ti}
Wentrub and Hieber[151]	<0.2	$FeO.TiO_2$			
	0.2-1	Ti_2O_3			
Evans and Sloman[152]	0.2-0.4	Ti_2O_3			
Hadley and Derge[153]	0.05-1	TiO_2			
	1-5	Ti_2O_3			
Liaudis and Samarine[154]	<0.04	$2Fe.TiO_2$	$-\frac{64250}{T} + 23.45$	1.4×10^{-11}	
		TiO_2	$-\frac{30700}{T} + 10.34$	8.9×10^{-7}	
Chipman[155]	<1	TiO_2			-0.187
Chino et al.[156]	0.001-0.2	Ti_3O_5	$-\frac{41500}{T} + 3.4$*	2×10^{-19}*	
	0.2-2	Ti_2O_3			
Suzuki et al.[157]	0.03-0.5	TiO_2	$-\frac{30900}{T} + 10$	3.2×10^{-7}	-0.158
Gatellier and Olette[158]	0.3	TiO_2		1.1×10^{-6}	
Kojima et al.[159]	0.0001-0.4	T_3O_5		3.5×10^{-18}	-0.37
	0.4-2	T_2O_3			-0.37

TABLE 2.8 (continued)

Authors	Ti %	Oxide formed	$\log K - \log h_N^X h_O^X$	$K_{1600°}$	e_O^{Ti}
Fruehan[24]	<1				-1.12
Fisher and Janke[160]	<0.3				-0.45
Smellie and Bell[161]	0.002-2	Ti_3O_5	$-\frac{90750}{T} + 29.15$	5.1×10^{-20}	-5.0
Suzuki and Sambongi[162]	0.013-0.25	Ti_3O_5		8×10^{-17}	-0.31
	0.25-4.8	Ti_2O_3			
	>4.8	TiO			
Jaquemont et al.[8]	<0.0013	TiO_2	$-\frac{33740}{T} + 11.72$	5×10^{-7}	
from ref. (25) and (20)	0.0013-0.09	Ti_3O_5	$-\frac{87020}{T} + 29.12$	4.6×10^{-18}	
	>0.09	Ti_2O_3	$-\frac{53280}{T} + 17.88$	2.7×10^{-11}	

*logK' rather than logK

oxides from the ingot without using any chemical reagents.

They concluded that only Ti_3O_5 and Ti_2O_3 were present and found:

$$\log K'_{Ti_3O_5} = \log [\%Ti]^3 [\%O]^5 = -\frac{41500}{T} + 3.4 \qquad (2.97)$$

They could not define exactly the value for

$$\log K'_{Ti_2O_3} = \log [\%Ti]^2 [\%O]^3 \qquad (2.98)$$

It is reported that Suzuki, Omori and Sambongi [157] equilibrated iron-titanium melts with H_2/H_2O mixtures and that for their deoxidation product (TiO_2), they found:

$$\log K_{TiO_2} = -\frac{30900}{T} + 10 \qquad (2.99)$$

Gatellier et al.[158] used an electrochemical cell with a ZrO_2-CaO solid electrolyte to study the system Fe-Ti-O. Using $e_O^{Ti} = -0.19$ from Chipman[155] and their own results for the activity of oxygen and the Ti content of the melt, they reported:

$$\log K'_{TiO_2} = 1.1 \times 10^{-6} \text{ at } 1600°C.$$

Kojima et al.[159] identified Ti_3O_5 and Ti_2O_3 as the deoxidation products in studies of the Fe-Ti-O system.

Fruehan[24] used a ThO_2-Y_2O_3 solid electrolyte in an electrochemical cell and from the measured h_O, he calculated h_{Ti} in Fe-Ti-O melts. The assumption was that for Ti>5% in the melt, only TiO exists as a stable phase. He concluded that $e_O^{Ti} = -1.12$ at 1600°C.

Fisher and Janke[160] used an electrochemical cell with a calcia stabilised zirconia electrolyte to determine the oxygen activity in Fe-Ti-O melts. Combining their results with chemical analysis, they found $e_O^{Ti} = -0.45$ at 1600°C.

Smellie and Bell[161] studied the same system at 1625° and 1700°C. Equilibrium was established between Fe-Ti-O alloys held in Ti_3O_5 or Al_2O_3 crucibles, and H_2/H_2O mixtures of known oxygen partial pressure. They identified Ti_2O_3 as the only product in their study and give:

$$\log K_{Ti_2O_3} = -\frac{90750}{T} + 29.15 \qquad (2.100)$$

The authors gave a good review of the existing controversy concerning the mixture of titanium deoxidation products. Suzuki and Sambongi[162] measured: (a) the partial pressure of oxygen in equilibrium with titanium oxides using oxygen concentration cells with ThO_2-based solid electrolytes, and (b) equilibria between titanium oxides and liquid Fe-Ti-O alloys.

Their results are summarised as follows:

1) In the deoxidation equilibria determined at 1600°C, the [%Ti] corresponding to the transition points is given by:

	[%Ti]
$Ti_4O_7 \rightleftarrows Ti_3O_5$	0.013
$Ti_3O_5 \rightleftarrows Ti_2O_3$	0.25
$Ti_2O_3 \rightleftarrows TiO$	4.8

2) $\log K_{Ti_3O_5} = 8 \times 10^{-17}$ at 1600°C

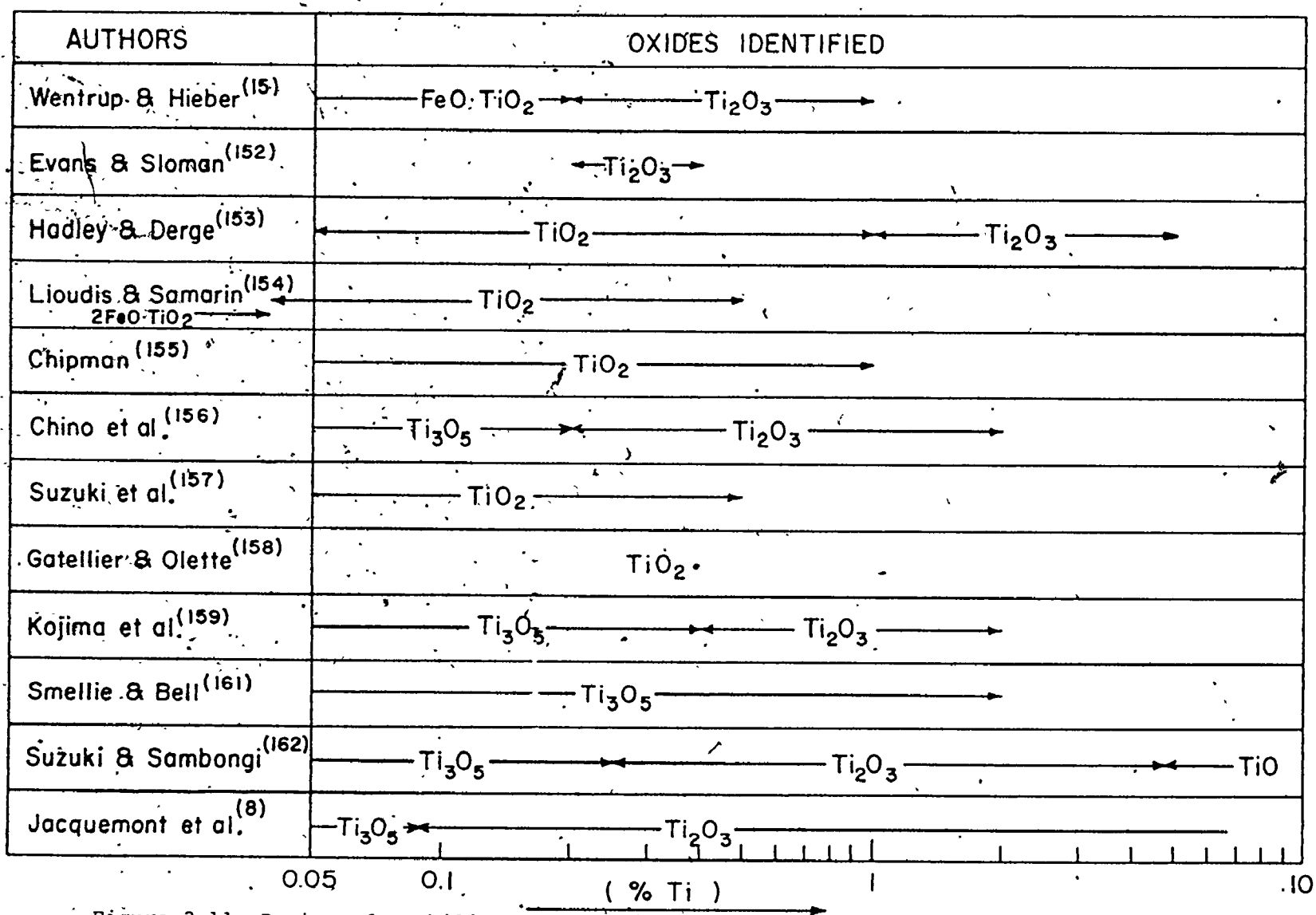

Figure 2.11 Region of stability of Titanium oxides as reported by several authors

3) The following interaction parameter and the activity coefficient of Ti were determined:

$$e_O^{Ti} = -\frac{1040}{T} + 0.245 \qquad (2.101)$$

$$e_{Ti}^{O} = -0.93,\ e_{Ti}^{Ti} = 0.042,\ \gamma_{Ti}^{O} = 0.016 \text{ at } 1600°C$$

4) P_{O_2} isotherms for the Ti-O system were drawn indicating the existence of Magneli phases between Ti_3O_5 and TiO_2. The oxygen contents of liquid Fe-Ti alloys equilibrated with different titanium oxides were determined at 1600°C.

Jaquemont et al.[8] using the data of Elliott et al.[25] and Chipman[20] present deoxidation product relationships for the oxides TiO_2, Ti_3O_5, Ti_2O_3. The results of the studies described above are summarised in Table 2.8.

Fig. 2.11 gives the regions of stability of titanium oxides in terms of %Ti as defined by different authors.

2.21 The Ti-O system

The controversy apparent in the previous section, concerning the titanium oxides present in iron deoxidation studies is also evident in studies of the Ti-O system. Several phase diagrams have appeared in the literature[163,164] and have been repeatedly revised and corrected. In 1966, Wahlbeck and Gilles[165] presented a Ti-O phase diagram based on the results of previous investigations and experiments of their own. Their diagram is shown in Fig. 2.12 and is divided into three regions:

1) Ti to Ti_2O

This region contains the α-hexagonal metal phase,

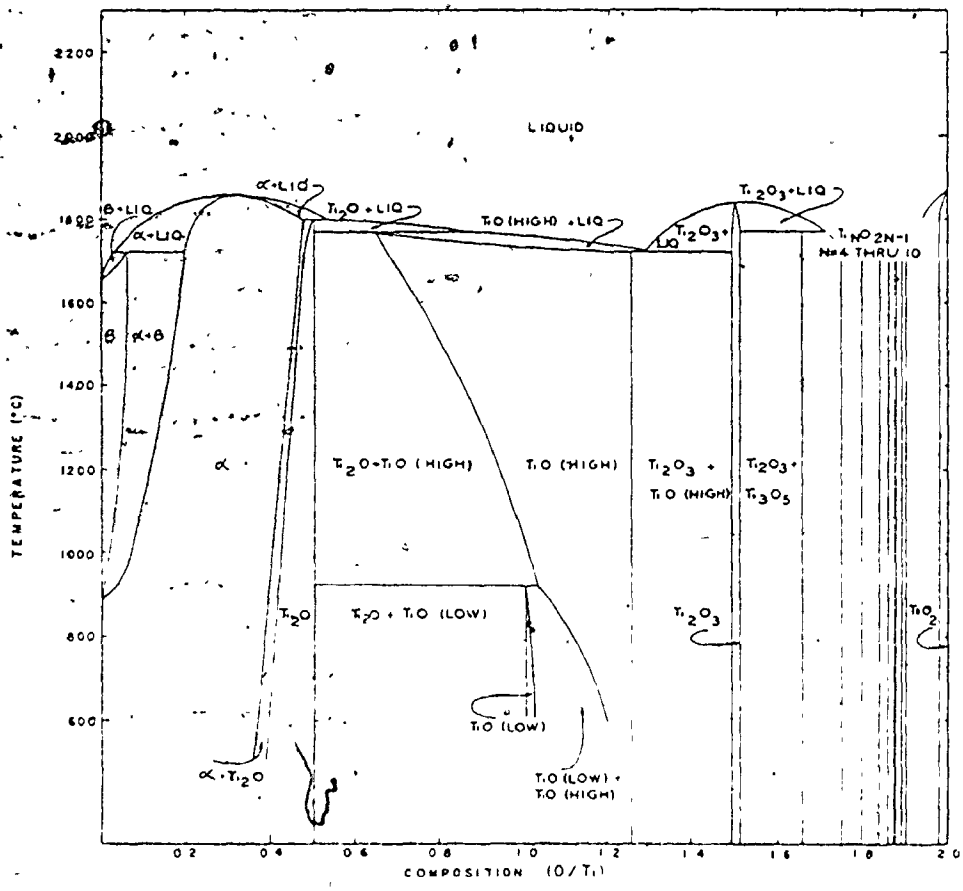

Figure 2.12 The Ti-O phase diagram[165]

the β cubic metal phase, the Ti_2O phase of variable composition, an ordered $Ti_2O_{1-1/3}$ phase and the Ti_2O phase.

2) Ti_2O to Ti_2O_3

This region contains high and low temperature TiO and two additional phases have been reported but their existence has not been confirmed. The high-temperature form of TiO has a NaCl-type structure and the low temperature form has a very complex X-ray pattern. Its structure has not yet been reported.

3) Ti_2O_3 to TiO_2

This region contains Ti_2O_3, Ti_3O_5 and several other discrete phases of the formula Ti_nO_{2n-1}.

There exists[167] a transition in crystal structure from a low temperature T_3O_5 which is monoclinic to a high temperature T_3O_5 which is also monoclinic but with different basic cell dimensions. The high-temperature phase appears to be stabilised by impurities of iron or magnesium, although Smellie and Bell[161] suggest that formation temperature and cooling rate also affect the transformation. The Magneli phases T_nO_{2n-1}, with n ranging from 3 to 10 have been confirmed by several workers in studies of the Fe-Ti-O system. Grey et al.[166] have found these Magneli phases to incorporate about 1% of divalent iron in solid solutions of the type $T_{1n}O_{2n-1}FeTi_{n-1}O_{2n-1}$ at 1900°C. The same authors reported the oxygen activity in equilibrium with several of these oxides.

In work by Sticher and Schmalzried[168], a diagram of P_{O_2} versus $\xi = \frac{n_{Ti}}{n_{Ti}+n_{Fe}}$ is presented, where all the titanium oxides stable at 1600°C are shown.

Finally Bursill and Hyde[169] give a comprehensive review on crystallographic aspects and conditions of formation of the higher titanium oxides.

CHAPTER III

APPARATUS AND EXPERIMENTAL TECHNIQUE

3.1 Introduction

A new electrochemical cell was designed to continuously monitor the oxygen activity in iron based melts, using calcia stabilised zirconia. The furnace atmosphere was either oxidising, using argon-oxygen mixtures, or reducing, using argon-hydrogen gas mixtures.

Plots of EMF versus time showed a plateau whenever two deoxidation phases coexisted. Outside the coexistence region the EMF was increased or decreased with time under oxidising and reducing conditions respectively. The melt was quenched under argon and the deoxidation phases identified by X-ray powder diffraction. Scanning electron microscopy was used to determine the morphology of the inclusions, after etching of the samples by an iodine etching technique.

3.2 Apparatus

3.2.1 The furnace

A vertically mounted, molybdenum wound, tubular resistance furnace was used for the experiments. The furnace and temperature control assembly are shown schemati-

cally in Fig. 3.1.

The furnace tube, of high purity recrystallised alumina, was wound with 0.05 in Mo wire over 14 in with 9, 8, 7, 8, 9, turns per inch for 2, 2½, 5, 2½ and 2 in respectively. This winding, gave a large furnace hot zone.

The furnace tube was centrally located in a brick lined cylindrical steel shell of 16 in diameter and 22 in in height. The shell was fitted with a removable top and base. The tube was secured by means of water-cooled glands and "O" rings, located at the top and the base of the shell. In this way the shell was gas tight. The space inside the shell around the tube was fitted with -8+72 mesh alundum grain and a protective 5% H_2-95%N_2 gas mixture was passed through the shell to prevent the Mo wire from oxidising. The whole furnace shell was very effectively watercooled by means of a $\frac{1}{4}$ in. copper tube welded around it with 0.5 turn/in.

A Pt 6%Rh-Pt 30%Rh control thermocouple was placed inside a thin recrystallised alumina sheath located at the side of the shell and extending up to the hot zone of the furnace tube.

Power to the furnace was supplied through a proportional power controller (Barber-Colman, series 621) driven by a null balance millivoltmeter controller (Barber-Colman Solid State Controller, series 520) which received the output from the control thermocouple. A current limiting feature was incorporated in the power controller to limit the output current to a predetermined value. This is essential

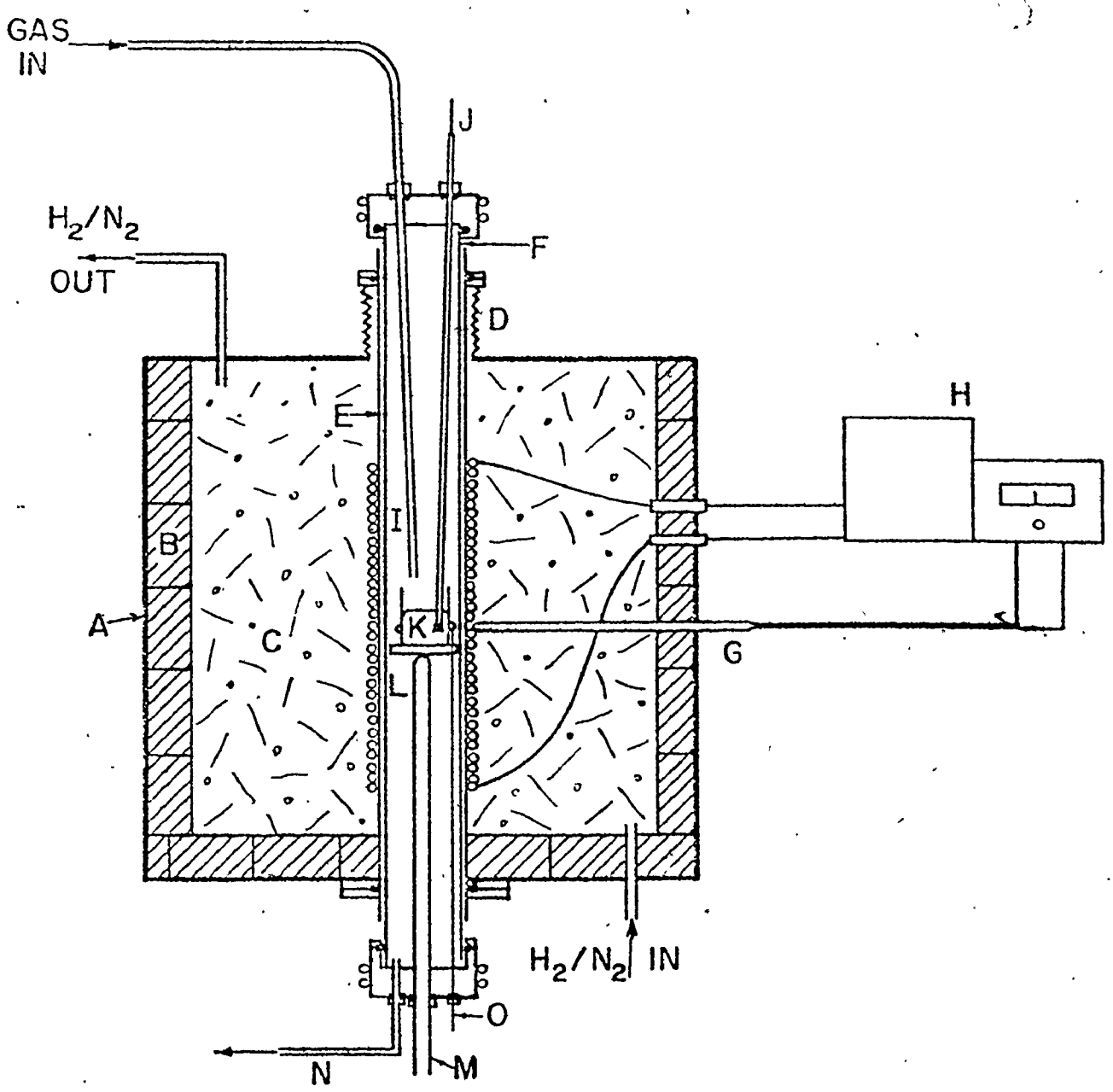

Figure 3.1 The furnace and temperature control assembly (not to scale)

under load conditions where transformer coupled heating elements have a very high temperature coefficient of resistivity, as is the case with Mo elements. An alumina working tube was placed concentrically inside the furnace tube.

A typical temperature profile of the furnace is shown in Fig. 3.2. The temperature variation at the hot zone of the furnace was ±2°C over 1 in and ±7°C over 2 in. The power controller limited variation in the furnace temperature to ±2°C.

The working tube was of high purity recrystallised alumina and was sealed at the top and bottom with water-cooled brass heads through "O" ring seals. The upper head had a central opening for insertion of the alumina tube supporting the Mo cermet lead, one opening sealed with a circular quartz disc for observation inside the furnace, and two more openings, one for inserting the gas inlet tube, and the second for inserting a thermocouple, whenever the temperature measurements were cross-checked with a thermocouple inserted inside the melt.

The lower head of the furnace had one central opening for inserting the thermocouple sheath and a second one for the Mo lead coming from the standard electrode of the cell (Fig. 3.4). This second opening was fitted with a Teflon stopper so that electrical contact between the Mo wire and the metallic furnace head was prevented.

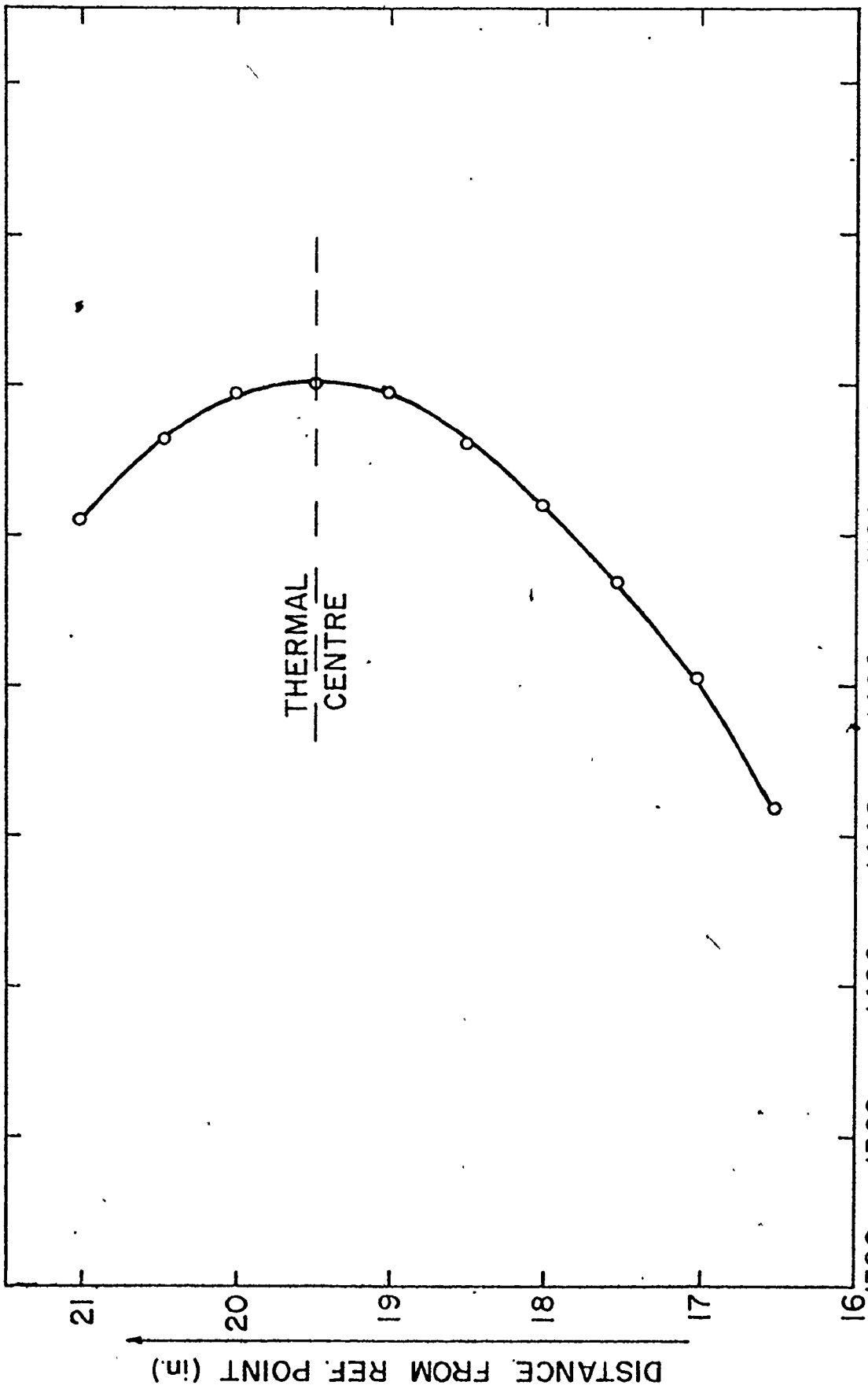

Figure 3.2 Temperature profile of the resistance furnace

3.2.2 The gas train

The gas train is shown schematically in Fig. 3.3 and, basically, consists of hydrogen and argon lines. Commercial purity H_2 was passed at room temperature through a palladium catalyst to convert traces of O_2 to H_2O, ascarite to remove CO_2 and a calibrated flowmeter. It was then mixed with prepurified argon and sent into the furnace. Argon was passed through tubes containing silica gel and drierite for H_2O removal, ascarite for CO_2 removal, and magnesium perchlorate to remove traces of H_2O. It was then passed over Zr chips held at 800°C for removal of oxygen. Finally it passed through a calibrated flow meter and sent to the furnace after mixing with hydrogen.

Whenever an oxidising atmosphere was desired, mixtures of argon + 1% Oxygen were passed through the argon purification line, omitting the Zr oxygen purification step. The mixtures were then passed through a calibrated flowmeter into the furnace.

3.2.3 The galvanic cell

A schematic diagram of the galvanic cell, is shown in Fig. 3.4.

The cell is basically similar to the one used by Vahed[6]. The metallic melt was held in a calcia-stabilised zirconia crucible, 1 in [illegible] in O.D. with a wall thickness of 1/8 in. The solid electrolyte crucible was placed inside an alumina crucible, 1½ in x 1½ in O.D. with a wall thickness of 1/16 in. The space between the two crucibles

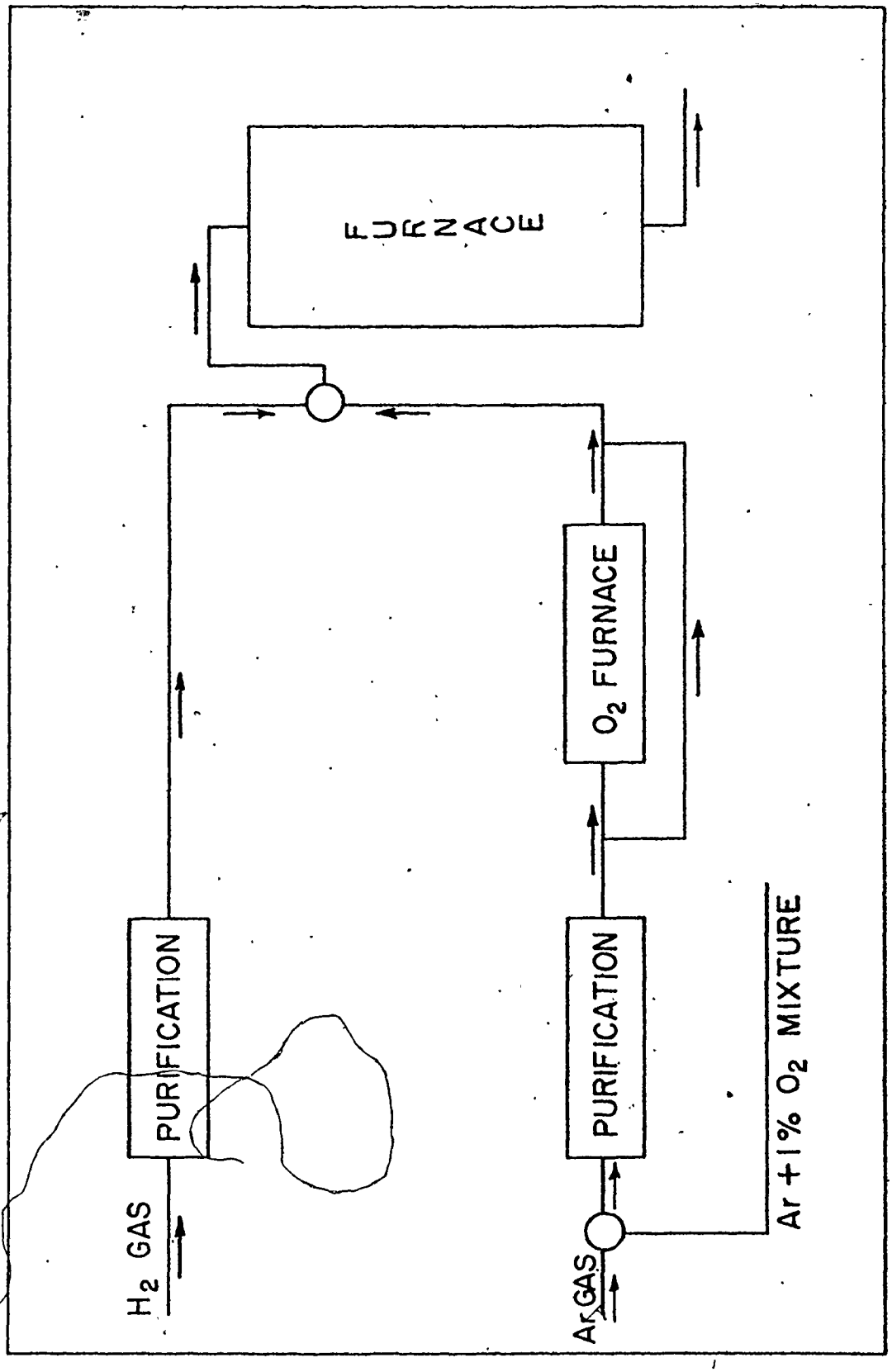

Figure 3.3 Schematic representation of the gas train

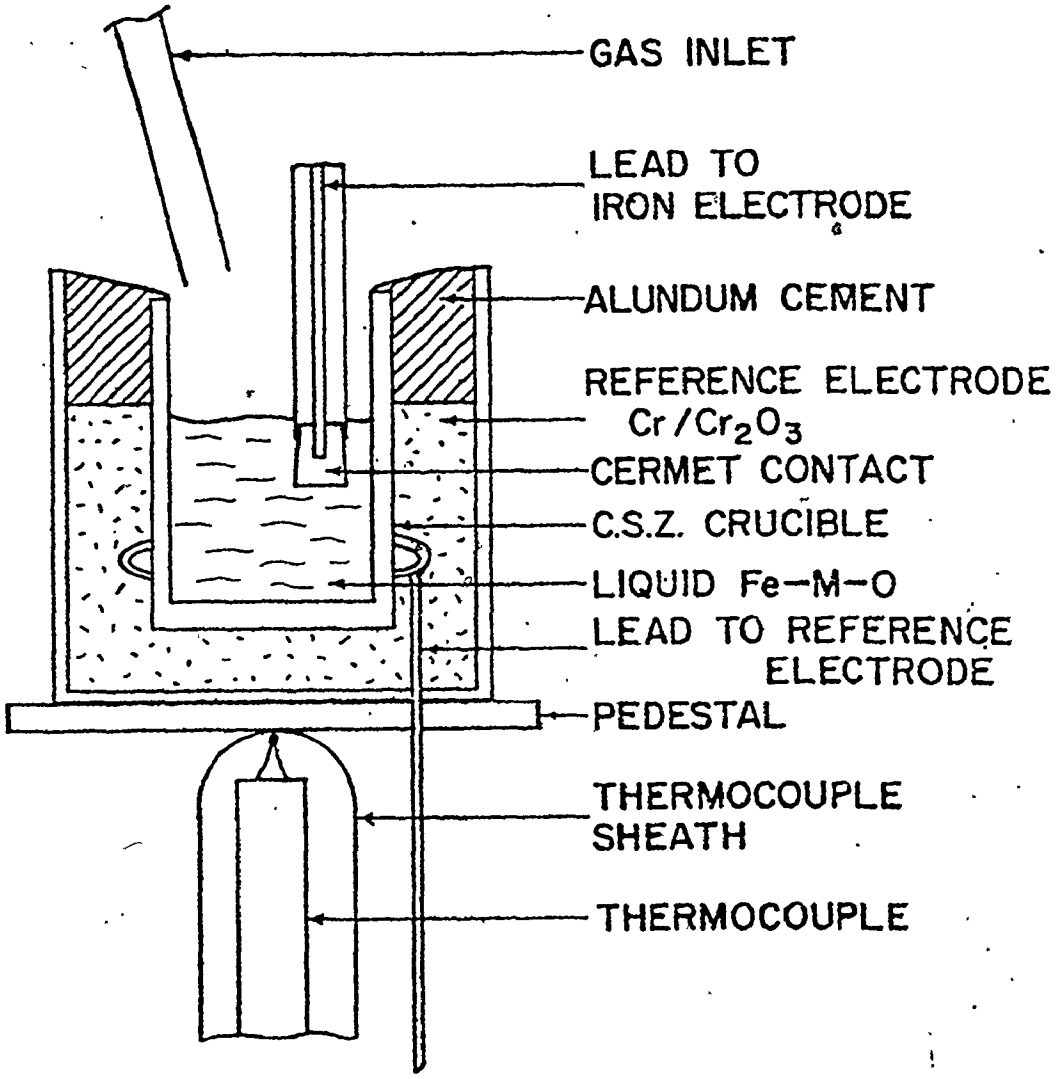

Figure 3.4 Schematic diagram of the galvanic cell

was filled with an equal volume mixture of either chromium metal and chromic oxide, or molybdenum metal and molybdenum oxide powders, to form the reference electrode. To avoid contact between the reference electrode and the furnace atmosphere, alundum cement was used to seal the annulus between the two crucibles, as in Fig. 3.4.

It was essential to ensure good contact between the reference electrode and the solid electrolyte crucible and therefore the metal/metal oxide mixture was well compacted between the two crucibles.

The leads from the two galvanic cell compartments were made of Mo wire. The lead from the reference electrode compartment was placed around the electrolyte crucible and in contact with it so as to prevent any error in EMF measurements caused by oxygen potential gradients across the electrode during the course of the experiments. It passed through the bottom of the alumina crucible through a small hole and finally out of the furnace through an insulated port in the lower brass head of the working tube.

The lead to the melt compartment made contact with the melt through a cermet made of ZrO_2 and Mo powder. The main reason for using a cermet in contact with the melt was to minimise the dissolution of Mo. Mo wire dissolved rapidly in the iron melt and without the cermet, it would result in melt contamination. Continuous monitoring of the EMF would also become impossible.

3.2.4 The cermet preparation

Because of the difficulties of welding premade cermets, which are commercially available, with the Mo wire lead, a method was developed[7] in our laboratory for making the cermet with the Mo wire already in contact with it. The metal-oxide powder mixture was pressed at 120 Kpsi around a Mo wire lead. It was then sintered under H_2 in an induction furnace at around 2000°C. Under controlled conditions of heating and cooling, the product was crack free. Its electrical resistance was found to be negligible.

Several metal/oxide powder ratios were tried to determine the optimum manufacturing conditions. A powder mixture, with a Mo/ZrO_2 volume ratio of 1/1.5 was finally adopted.

After grinding, the cermet was mechanically fitted into an alumina tube (1/4 in O.D. and 1/8 in I.D.) to prevent dissolution of the Mo lead. The cermet and lead was inserted in the melt, through the central opening of the upper head of the furnace working tube.

Fig. 3.5 shows a cermet before and after use for 1 hour at 1600°C. It is obvious that cermet deterioration is negligible.

3.3 Experimental technique

3.3.1 EMF measurements

About 20 g of very pure iron together with the necessary additions of deoxidation elements (Al, Al-Mn, Nb, Ti) were put into the solid electrolyte crucible. The whole

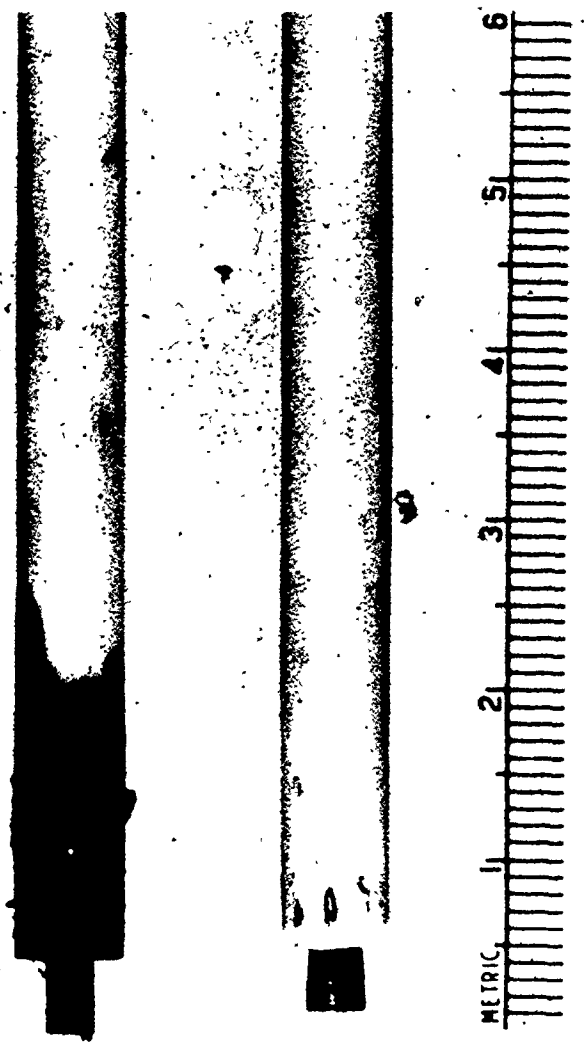

Figure 3.5 A cermet mounted in an alumina tube, before and after use for 1 hr at 1600°C

cell was inserted in the furnace bottom, and by means of the thermocouple sheath, used also as cell support, it was slowly raised to the hot zone of the furnace. To avoid thermal shock of the alumina and electrolyte crucibles, the rate of raising the cell was about 1 in/10 minutes. During the same time, the furnace temperature was raised from 1200°C where the furnace was continuously kept, to the experimental temperature at the rate of 80°C/hour. The alumina tube supporting the cermet lead was also slowly lowered from the top of the furnace.

The furnace atmosphere was a mixture of argon and hydrogen, so that the Mo wire lead would not be oxidised and the alloy produced would be essentially oxygen free. In this way the complete dissolution of the deoxidising element in the molten iron was ensured.

Once the metal was molten and had reached the desired temperature, the cermet was inserted in the melt and a spot EMF measurement taken, to give an estimation of the oxygen activity in the melt. The hydrogen-argon mixture was then exchanged for an argon+1% oxygen mixture which was blown onto the melt by means of an alumina tube. The melt was agitated either by moving the cermet or by the gas flow itself so as to ensure melt homogeneity with respect to dissolved oxygen. The EMF was measured either with a type P3 Croydon potentiometer at normally 2 minutes invervals, or it was continuously recorded using a Honeywell potentiometric chart recorder.

During oxydation the EMF was increased with time until it reached the region in which the deoxidation products were in coexistence, where it remained constant for a certain time. After this, the EMF rose again, indicating that the lower oxide product was completely transformed into a higher oxide product.

During the time of the EMF vs. time plateau, the EMF was recorded with the furnace switched 'on' or 'off'. No difference was observed between the two readings, indicating that there were no induction effects on the cell. The oxidising gas flow rate was also increased or decreased during the plateau time, without any effect on the reading. It was observed that the electrolyte crucibles failed whenever the melt was highly oxidised. It was thus very difficult to perform an experiment under reducing conditions, i.e. starting from a superoxidised melt. Whenever such an experiment was done, the initial melt produced under reducing conditions, was vigorously flashed with the argon-oxygen mixture and once it was ensured that only the higher oxide phase was present, the hydrogen-argon gas was immediately introduced. The EMF then decreased and again showed a plateau at the two phase coexistence region. Considerable skill was required for experiments starting from an oxidised melt and accurate measurements were possible only for plateaus occurring at low oxygen activities.

At the end of the experiment, the sample was quenched to try and retain the deoxidation phases occurring at the experimental temperature.

3.3.2 Temperature measurements

The temperature was basically measured with a Pt 20%Rh -Pt 5%Rh thermocouple placed inside the thermocouple sheath supporting the cell. Care was taken to ensure that the cell was placed at exactly the furnace thermal centre. In this way, the temperature gradient within the cell was minimised, and it could be assumed that the temperature of the thermocouple was the same as that of the melt.

It was essential that thermal equilibrium was established during the course of an experiment. Readings were taken every two minutes during the measurement of the plateau EMF, to indicate any possible temperature change. Another thermocouple inserted from the top of the furnace was used to measure the temperature just above the melt. Whenever such a measurement was carried out, the two readings agreed within ±2°C.

Both thermocouples were calibrated against a standard thermocouple Pt 30%Rh-Pt 6%Rh - purchased from Thermo Electric and calibrated at N.R.C. The difference of ±2°C was within experimental error.

3.4 Oxide phase identification

The identification of the deoxidation phases existing during an experiment was carried out by X-ray powder diffraction.

The oxide layer on top of a solidified melt was scraped off using a stainless steel knife, and the powder

produced was ground in an agate mortar. Iron and iron oxide particles were removed by magnet and the rest was used for Debye-Scherer X-ray powder diffraction. Due to the small amount of the sample collected, eight hours of exposure were required, instead of the normal four hours, in order to get a distinct pattern. The use of a diffractometer was impossible again because of the very small sample quantity.

In order to observe the morphology of the oxide products, an iodine etching technique was used. Kitikawa[170] successfully used this technique in order to identify graphite flakes in carbon saturated iron. In Fig. 3.6, a schematic diagram of the apparatus used, is shown. A Lindberg Hevi-Duty model 54356-A furnace, with three independently controlled thermal elements was used. A steep thermal gradient (450°C/2 in) was achieved by setting the first thermal element at zero, the next two at 1020°C, and inserting a refractory ring to separate the hot from the cold zones.

The reaction chamber was a quartz tube 15 in long and 1 in diameter. A small piece (∿2g) of alloy sample was put in the tube along with 50 mg of solid iodine. The tube was vacuum sealed and put into the furnace, 5 in containing the alloy sample in the cold zone, and the rest in the hot zone. The reactions taking place in the different zones of the reaction chamber are shown in Fig. 3.6. Under these conditions a continuous removal of Fe from the sample occurs.

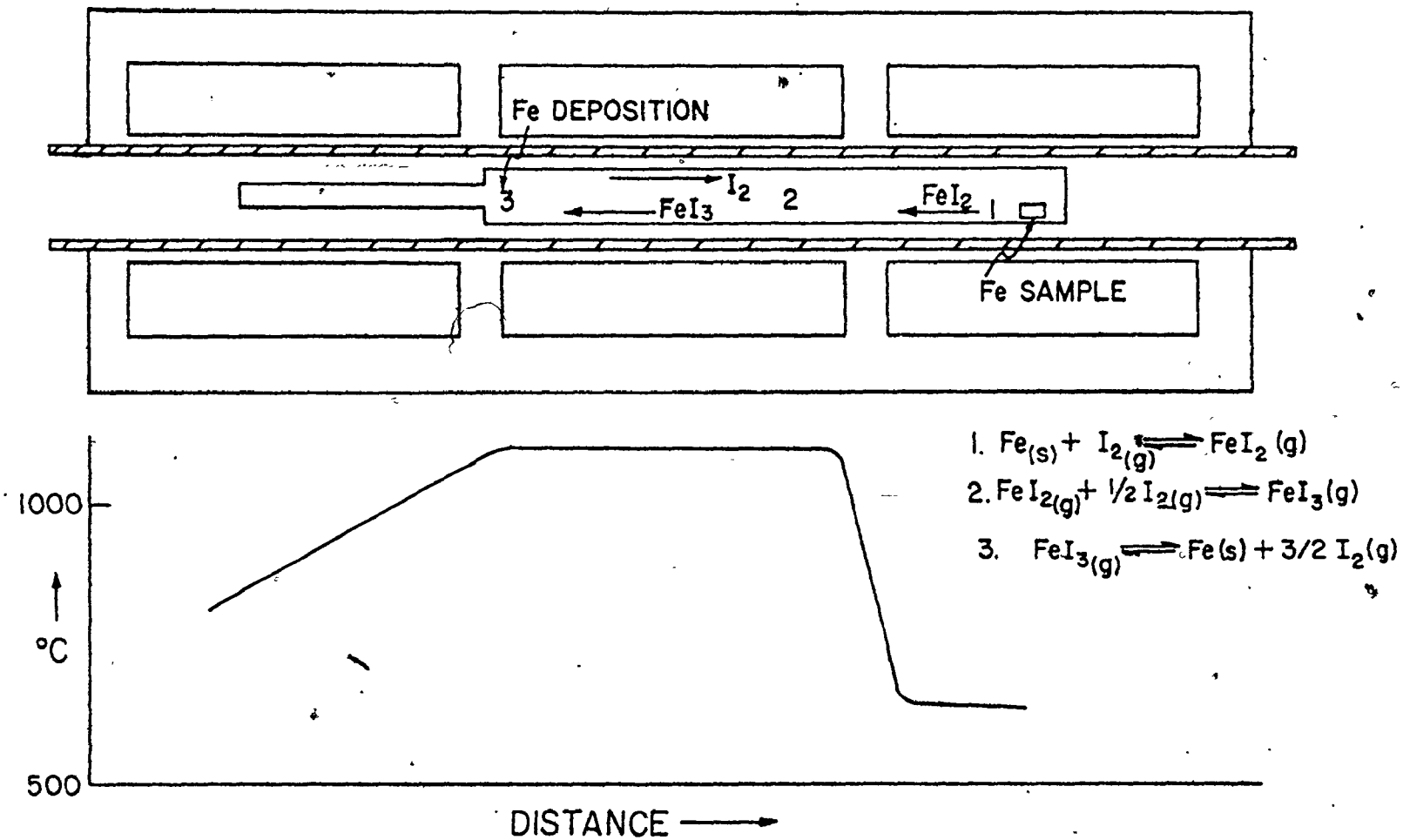

Figure 3.6 Schematic diagram of the apparatus used for the iodine etching technique

The iron is deposited in the hot zone and the free iodine diffuses back to continue the etching of the sample. After about 20 hr the quartz tube was cooled by first cooling the hot zone keeping the other zone at about 650°C, and then cooling that also. In this way, the volatile iodine and iodine compounds were deposited in the end of the tube away from the sample. The sample was taken out and examined in a scanning electron microscope. Since only the Fe was dissolved, all the oxide phases were clearly visible.

3.5 Testing of solid electrolyte crucibles

The calcia stabilised zirconia crucibles were bought from ZIRCOA. It was specified that the material should be fully stabilised (7.5 wt% calcia) and made from high purity, nuclear grade zirconia. The crucibles should have a bulk density of not less than 95% of the theoretical value and they should be leak tested at 10^{-6} Torr. In spite of all these specifications, quite a few of the crucibles did not perform satisfactorily, failing at the beginning of the experiments. In such cases the EMF dropped to zero because of direct contact between the two electrodes, through micro-cracks in the electrolyte.

A systematic investigation was thus undertaken to reveal the reason of poor performance. The main tests carried out are described below:

3.5.1 Bulk density measurements

A mercury displacement technique was used to measure the bulk density of the crucibles. The apparatus used is

shown in Fig. 3.7. Although most of the crucibles were found to have a bulk density around 98% of the theoretical value, a few showed values much lower than 95%, and one gave a value of only 83% of the theoretical value. All those crucibles were discarded.

3.5.2 Leak testing

The crucibles were leak tested at 10^{-6} Torr using helium and freon leak detectors. In the helium leak detector, the crucible is put under a vacuum of 10^{-6} Torr and helium is blown on its outer surface. The existence of cracks is detected by the helium passing through them into the vacuum chamber, and its detection by mass-spectrometry.

In the freon leak detector the procedure is the same, except that the freon in the vacuum chamber is detected by the heat evolved when the freon dissociates on a platinum filament. Crucibles which were not leak proof were also discarded.

3.5.3 Microscopic examination

Metallographic examination revealed that crucibles failing the previous tests were highly porous and some of them also showed a third phase in the grain boundaries. This phase was examined in an electron microprobe and proved to be a calcium aluminum silicate. Such a phase probably has a low melting point and causes the failure of the crucible.

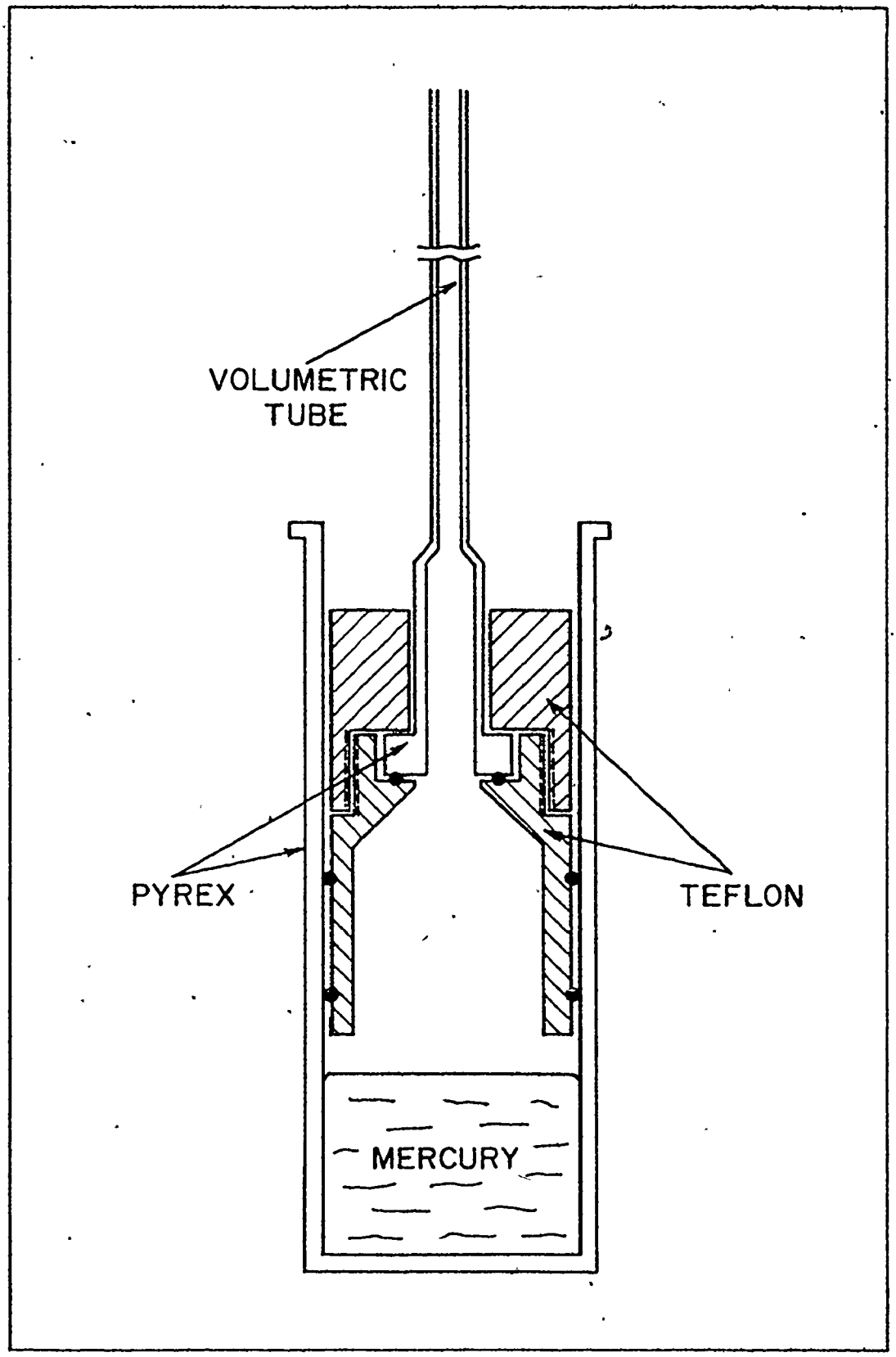

Figure 3.7 Apparatus for mercury displacement, volume measurements

Fig. 3.8 shows:

(a) The third phase and the high porosity of the crucible material.

(b) A large crack in a crucible that failed during an experiment. The melt, of very low oxygen activity, reacted with the Cr_2O_3 and formed a continuous metallic layer on the outside of the crucible.

Poor properties of the crucible material were attributed to impure raw materials and bad sintering conditions combined with almost complete lack of quality control in the manufacturing company.

3.6 Materials

Alloys were made during each experiment. The iron used was Ferrovac 'E' supplied by Crucible Steel Corp. in the form of rods, 6 in x 1 in D. The chemical analysis is given in Table 3.1. High purity niobium in the form of metal plate was supplied by the Kawecki Chemical Co.

Aluminum of ultra high purity (99.995% Al) was supplied by Alcan in the form of $\frac{1}{2}$" thick rolled slab. High purity Ti (99.98%) was supplied by Alfa Inorganics in the form of metal foil, 10 mil thick. Manganese was in the form of 99.99% pure electrolyte platelets and it was obtained from A. D. Mackay Inc.

Chromium powder for the electrode, and Mo powder for the cermets and the standard electrode, were supplied by Alfa Inorganics. Their analysis and size are given in Table 3.2.

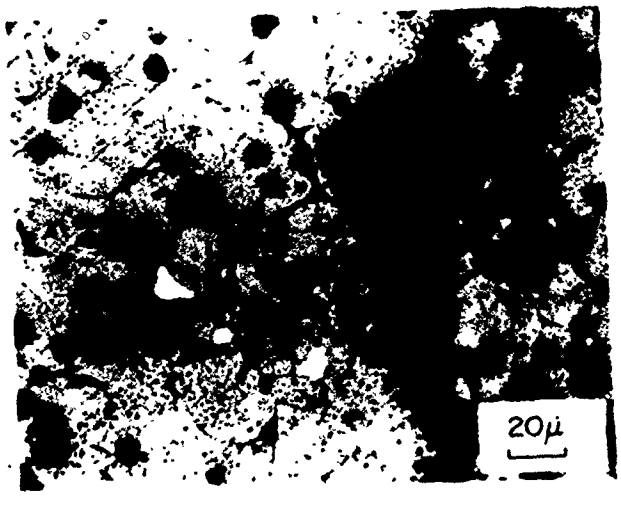

Figure 3.8 CSZ crucible micrographs

Cr_2O_3 for the standard electrode was Fisher "Certified Reagent" grade and the MoO_2 was obtained from Alfa Inorganics.

TABLE 3.1

Analysis of Ferrovac E in weight percent

C	0.008	Mo	0.001
Mn	0.001	Co	0.004
P	0.002	Cu	0.001
S	0.005	Sn	0.002
Si	0.005	Pb	0,0005
Ni	0.025	Al	<0.01
Cr	0.001	N_2	0.00015
V	0.004	O_2	0.0012
W	0.01	H_2	0.00006

Fe = 99.92

TABLE 3.2

Chemical	Metallic Impurity	Total impurity	Size
Chromium powder	0.02%	0.1%	-140 mesh
Molybdenum powder	<0.1	0.3%	-200 mesh
MoO_2	-	<0.1%	-200 mesh

CHAPTER IV

EXPERIMENTAL RESULTS

4.1 Introduction

The results obtained from studies of the systems Fe-Nb-O, Fe-Al-O and Fe-Al-Mn-O are reported in this chapter. The results from successful experimental runs, and all thermodynamic information extracted from those results are shown. Finally, the X-ray diffraction patterns and scanning electron microscope photographs of the oxide inclusions are presented.

It should be noted that since the Fe-Nb-O system was the first to be investigated, the development of the experimental technique was based on results obtained in this system.

Accordingly, Mo $|MoO_2$ was abandoned as a reference electrode since Mo metal coated the outside of the electrolyte crucible, resulting in premature polarisation.

EMF measurements made from an oxidised melt with subsequent reduction by $Ar+H_2$ mixtures again led to premature electrolyte crucible failure.

Figures 4.4 and 4.5 show the only runs involving measurements taken during reduction. Fig. 4.5 shows also the only run involving $Mo|MoO_2$ as a reference electrode. Whenever possible, an external EMF was imposed on the cell to test whether or not there was any polarisation effect on the EMF. The results did not indicate any such effect as is clear from the corresponding figures.

The third low analysis of the experimental results was used only for the Fe-Al-O data as this was the only system where accurate specific heat values are tabulated for all the constituents in the transition point reaction.

4.2 $Logh_O$ from the measured EMF

The cell used can be represented as follows:

$$Mo\left|\begin{matrix}Cr/Cr_2O_3\\ or\\ Mo/MoO_2\end{matrix}\right|\begin{matrix}CSZ\\ solid\\ electrolyte\end{matrix}\left|\begin{matrix}\underline{M},\underline{O}\text{ in liquid}\\ Fe\end{matrix}\right|\begin{matrix}ZrO_2\text{-}Mo,\ Mo\\ cermet\end{matrix} \qquad (4.1)$$

The virtual cell reaction may be written as:

$$\underline{O}_{1w/o} + \frac{2}{3}Cr_{(s)} \rightleftarrows \frac{1}{3}Cr_2O_{3(s)} \qquad (4.2)$$

or

$$\underline{O}_{1w/o} + \frac{1}{2}Mo_{(s)} \rightleftarrows \frac{1}{2}MoO_{2(s)} \qquad (4.3)$$

For reaction (4.2) the data used for the standard free energy of formation of Cr_2O_3 are those given by Jeannin et al.[171] These, combined with the data for the reaction:

$$\frac{1}{2}O_2 \rightleftarrows \underline{O}_{1w/o} \qquad (2.20)$$

give the standard free energy change for reaction (4.2).

Using the relation:

$$\Delta G_{T_{(4.2)}} = \Delta G^{\circ}_{T_{(4.2)}} - RT\ell nh_O \qquad (4.4)$$

the final relation of $logh_O$, temperature and cell EMF may be calculated. The following expression has been used in this study:

$$logh_O = 4.52 - \frac{13300 - 10.08E_{(mV)}}{T} \qquad (4.5)$$

taken from reference (6).

When $Mo|MoO_2$ was used as the reference electrode, the relation between $logh_O$, T and EMF was calculated using the free energy data for MoO_2 formation as reported by Chan et al.[134] and the relation (2.21) for the reaction (2.20). The resulting equation is:

$$logh_O = 4.52 - \frac{8740 - 10.05E_{(mV)}}{T} \qquad (4.6)$$

Equation (4.5) and (4.6) have been used to calculate $logh_O$ at the transition point for the systems studied. The results are presented in the corresponding tables.

4.3 Results in Fe-Nb-O system

(a) Transition point equilibrium

Figures 4.1 to 4.5 show the experimental runs for different temperatures for the Fe-Nb-O system. The plateaus shown are very stable, the scatter in the measurements at the plateau never exceeding ±1.5mV. It can be seen that the solid electrolyte crucibles failed a short time after the oxygen potential of the transition point was exceeded. The

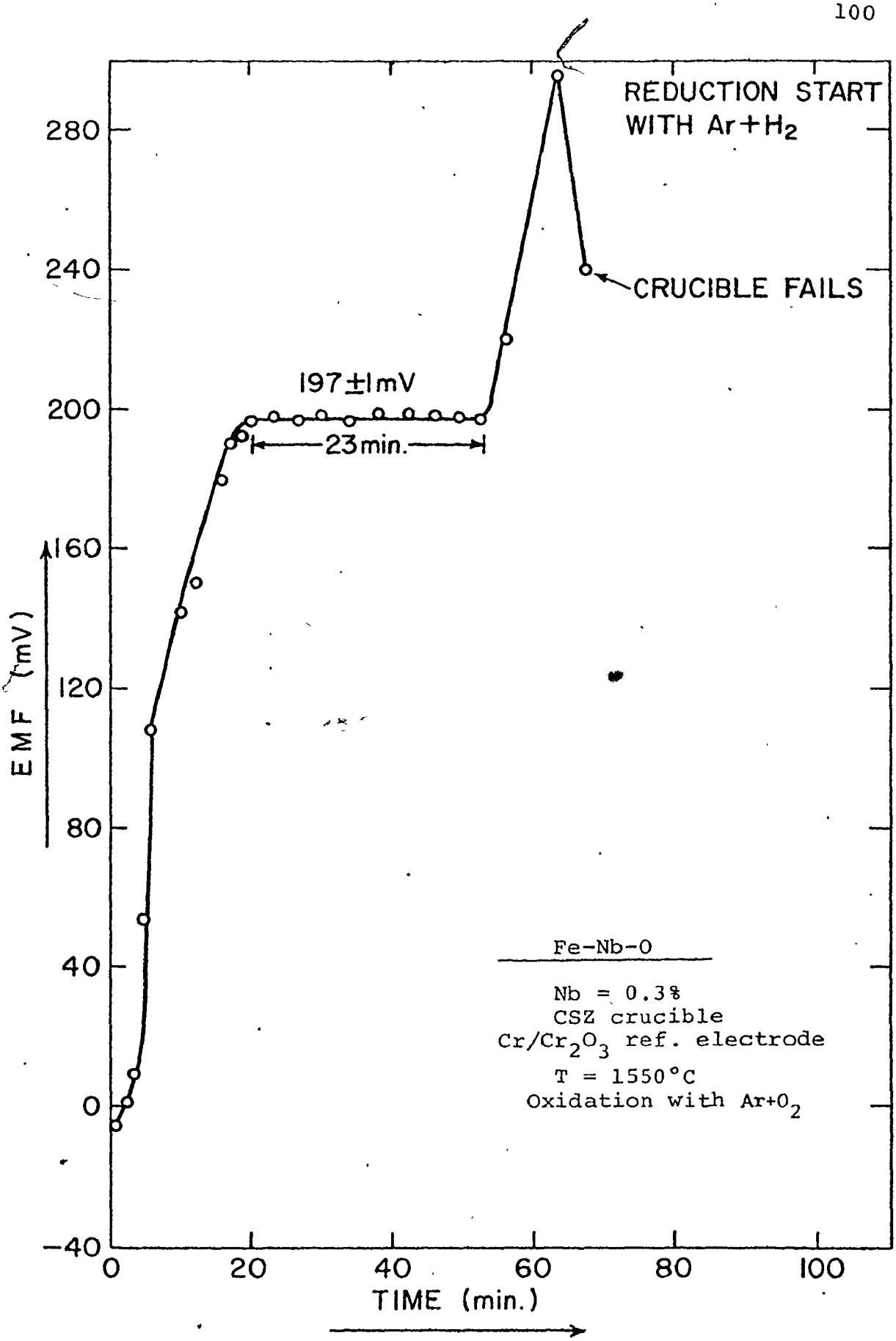

Figure 4.1 Experimental run in the Fe-Nb-O system

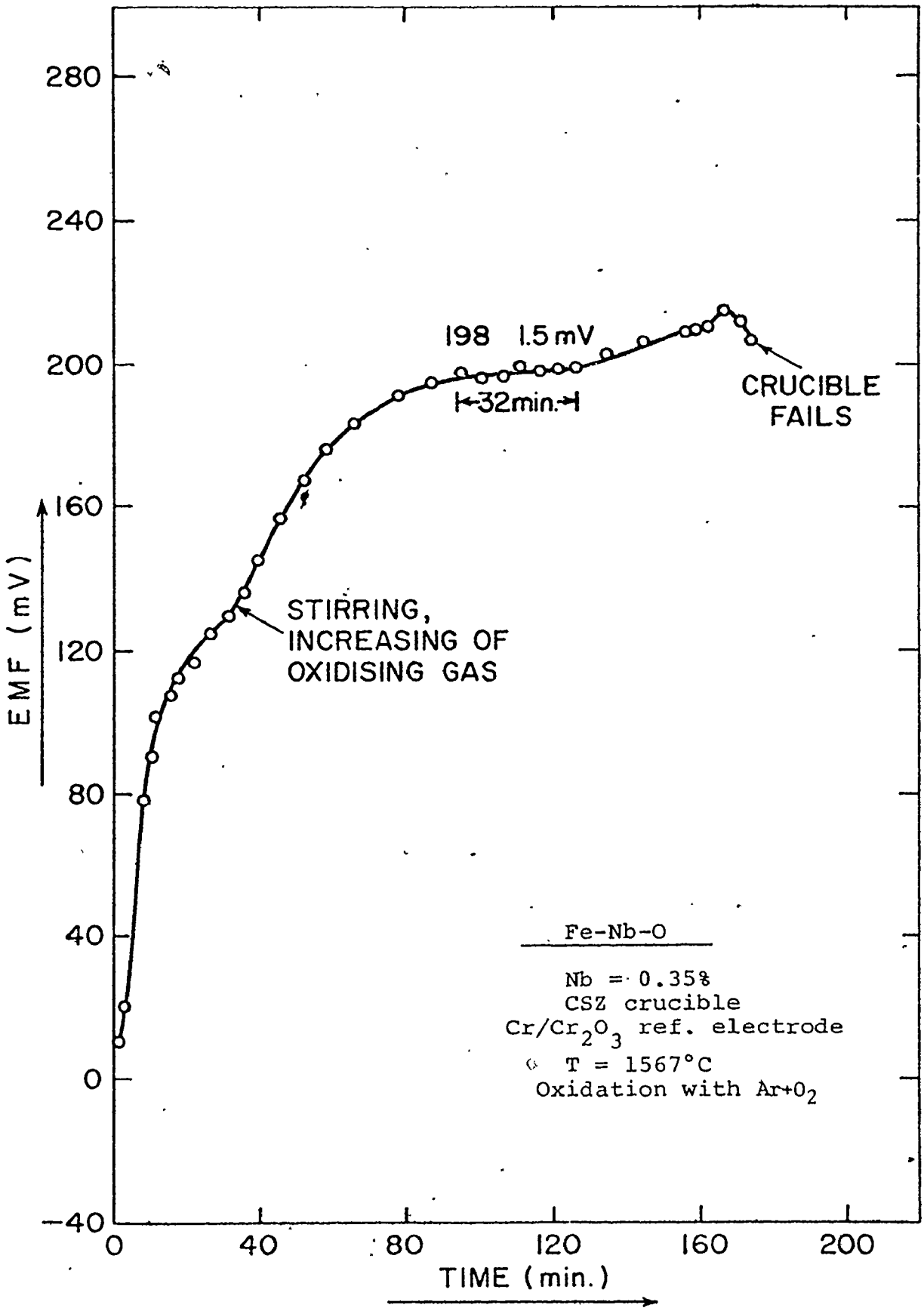

Figure 4.2 Experimental run in the Fe-Nb-O system

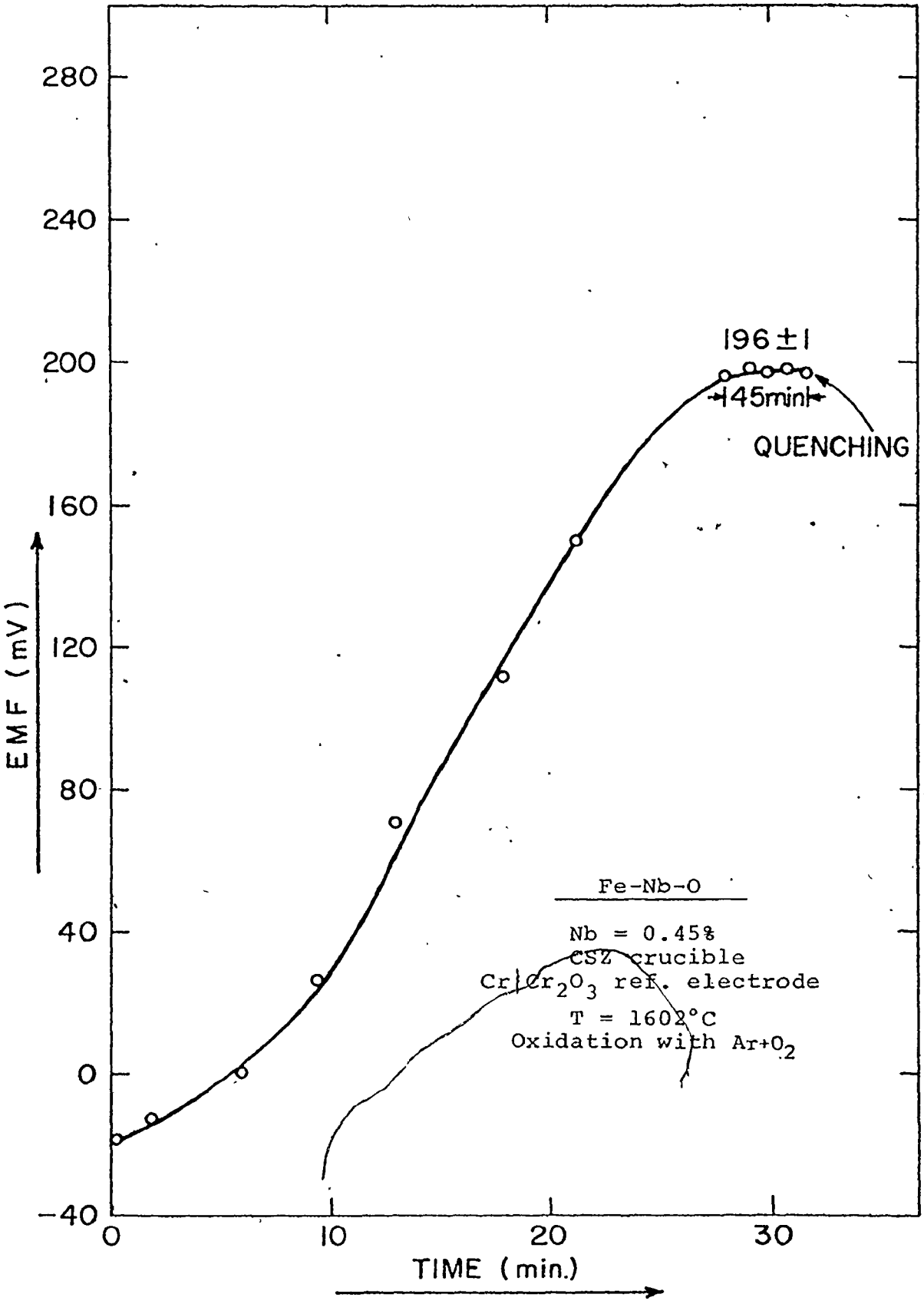

Figure 4.3 Experimental run in the Fe-Nb-O system

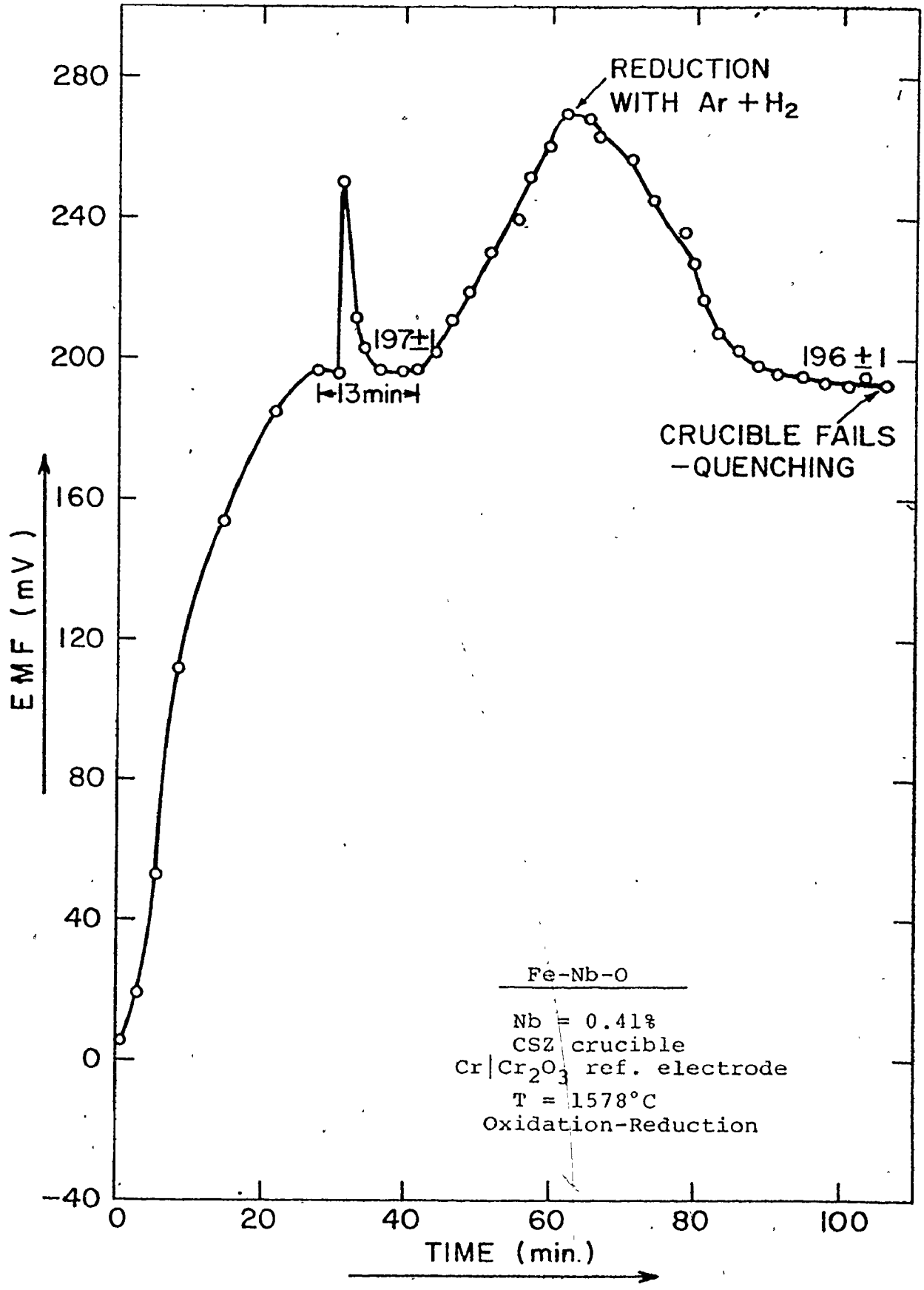

Figure 4.4 Experimental run in the Fe-Nb-O system

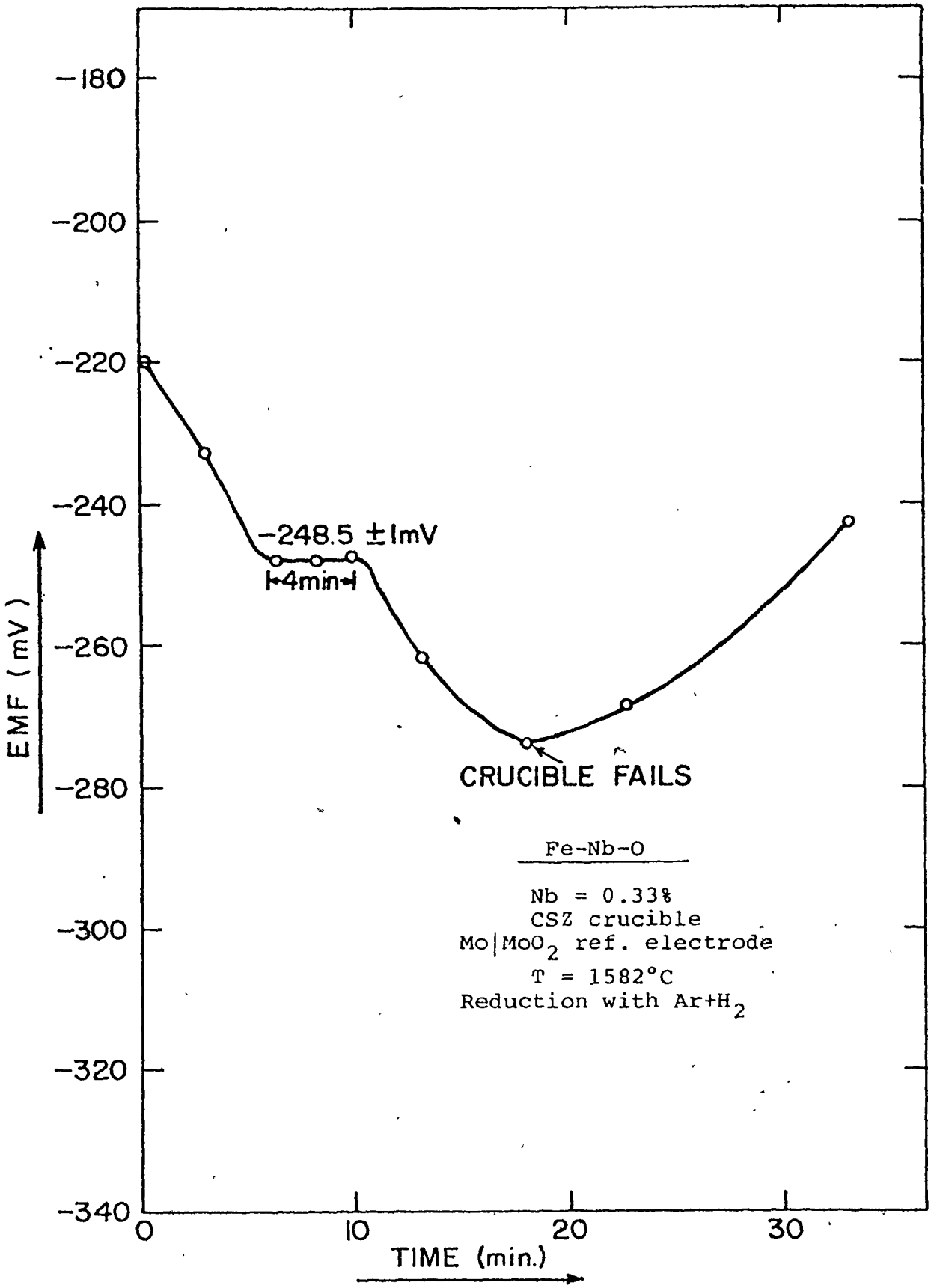

Figure 4.5 Experimental run in the Fe-Nb-O system

run in Fig. 4.4 was particularly successful as the crucible lasted long enough for the plateau to be approached during reduction from the oxidised melt also. In Fig. 4.5, results from the only successful run using $Mo|MoO_2$ as a reference electrode are shown.

The deoxidation products were identified (see below) as NbO_2 and $FeNb_2O_6$. Therefore, the reaction in equilibrium at the plateau can be written as:

$$FeNb_2O_{6(s)} \rightleftarrows Fe_{(\ell)} + 2NbO_{2(s)} + 2\underline{O}_{1w/o} \qquad (4.7)$$

$Logh_O$ and ΔG°_T for reaction (4.7) were calculated from the experimental data and are shown in Table 4.1.

In the same Table, ΔG°_T for the reaction:

$$FeNb_2O_{6(s)} \rightleftarrows Fe_{(\ell)} + 2NbO_{2(s)} + O_{2(g)} \qquad (4.8)$$

is presented. This was calculated from $\Delta G^\circ_{T(4.7)}$ and equation (2.20).

In Fig. 4.6 $logh_O$ for the reaction (4.7) is plotted against $\frac{1}{T}$. Apart from the point taken from the run using $Mo|MoO_2$ as the reference electrode the others show a very small deviation from linearity. Least square analysis of the data, excluding the $Mo|MoO_2$, yields:

$$logh_{O_{(4.7)}} = 4.66 - \frac{11570}{T} \qquad (4.9)$$

While there is enough evidence to indicate that the five points in Fig. 4.6 using Cr/Cr_2O_3 as a reference electrode

TABLE 4.1

Experimental Results on the Fe-Nb-O System

T°C	$\frac{1}{T} \times 10^4$ ($°K^{-1} \times 10^4$)	EMF (mV)	$\log h_O$	$\Delta G^\circ_{T(4.7)}$	$\Delta G^\circ_{T(4.8)}$
1550	5.485	197	-1.69	28190	86710
1567	5.435	198	-1.62	27270	85810
1578	5.402	197	-1.59	26930	85480
		196	-1.60	27100	85650
1582	5.391	-248.5*	-1.54	26140	84700
1602	5.333	196	-1.52	26080	84670

4.7: $FeNb_2O_{6(s)} \rightleftarrows Fe_{(\ell)} + 2NbO_{2(s)} + 2\underline{O}$ 1w/o

4.8: $FeNb_2O_{6(s)} \rightleftarrows Fe_{(\ell)} + 2NbO_{2(s)} + O_{2(g)}$

* $Mo|MoO_2$ used as reference electrode

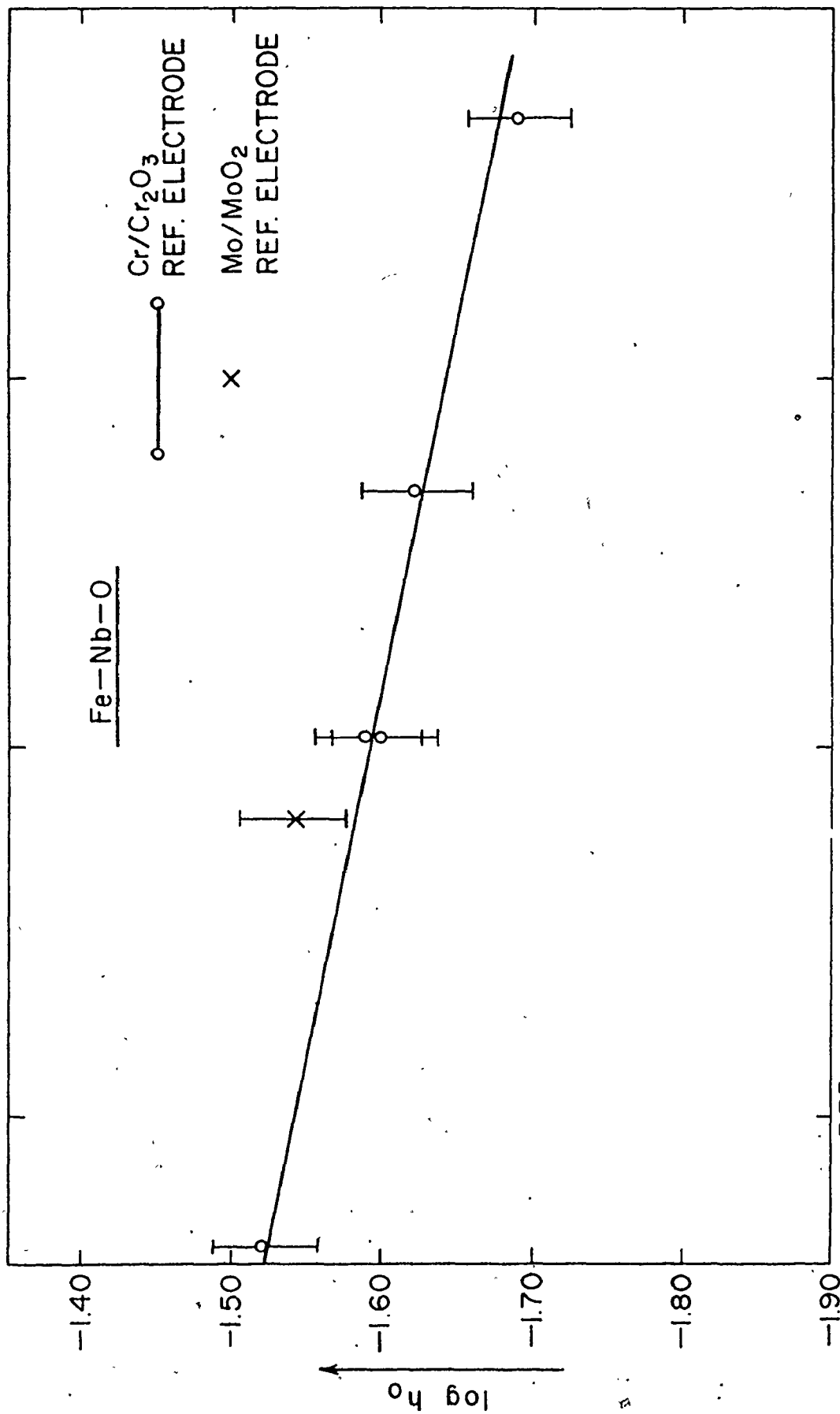

Figure 4.6 $\text{Log}h_o$ versus $\frac{1}{T}$ for the reaction: $FeNb_2O_{6(s)} + Fe_{(\ell)} + 2NbO_{2(s)} + 2\underline{O}$ lw/o

are self consistent, the validity of the result taken with $Mo|MoO_2$ as the reference electrode is suspect. Hence, in calculating $\log h_O$ vs. $\frac{1}{T}$ for the reaction (4.7), equation (4.9) is chosen for the temperature range of the present study (1550-1600°C). From equation (4.9), $\Delta G^\circ_{)4.7)}$ may be calculated using the relation:

$$\Delta G^\circ_{(4.7)} = -RT\ell nK_{(4.7)} = -2x4.575T \log h_O \qquad (4.10)$$

$$\Delta G^\circ_{(4.7)} = 105870 - 42.64T \text{ cal} \quad (1550\text{-}1600°C) \qquad (4.11)$$

Using Narita's and Koyama's[101] data

$$\log h_{O_{(4.7)}} = 4.463 - \frac{11370}{T} \qquad (4.12)$$

and

$$\Delta G^\circ_{(4.7)} = 104040 - 40.81T \text{ cal} \qquad (4.13)$$

In Fig. 4.7, the corresponding values of $\Delta G^\circ_{(4.7)}$ are shown as a function of temperature.

Combining equation (4.11) with equation (2.21), ΔG° for reaction (4.8) may be calculated as a function of temperature:

$$\Delta G^\circ_{(4.8)} = \Delta G^\circ_{(4.7)} - 2\Delta G^\circ_{(2.20)} \qquad (4.14)$$

and

$$\Delta G^\circ_{(4.8)} = 161870 - 41.26\ T \text{ cal} \ (1550\text{-}1600°C) \qquad (4.15)$$

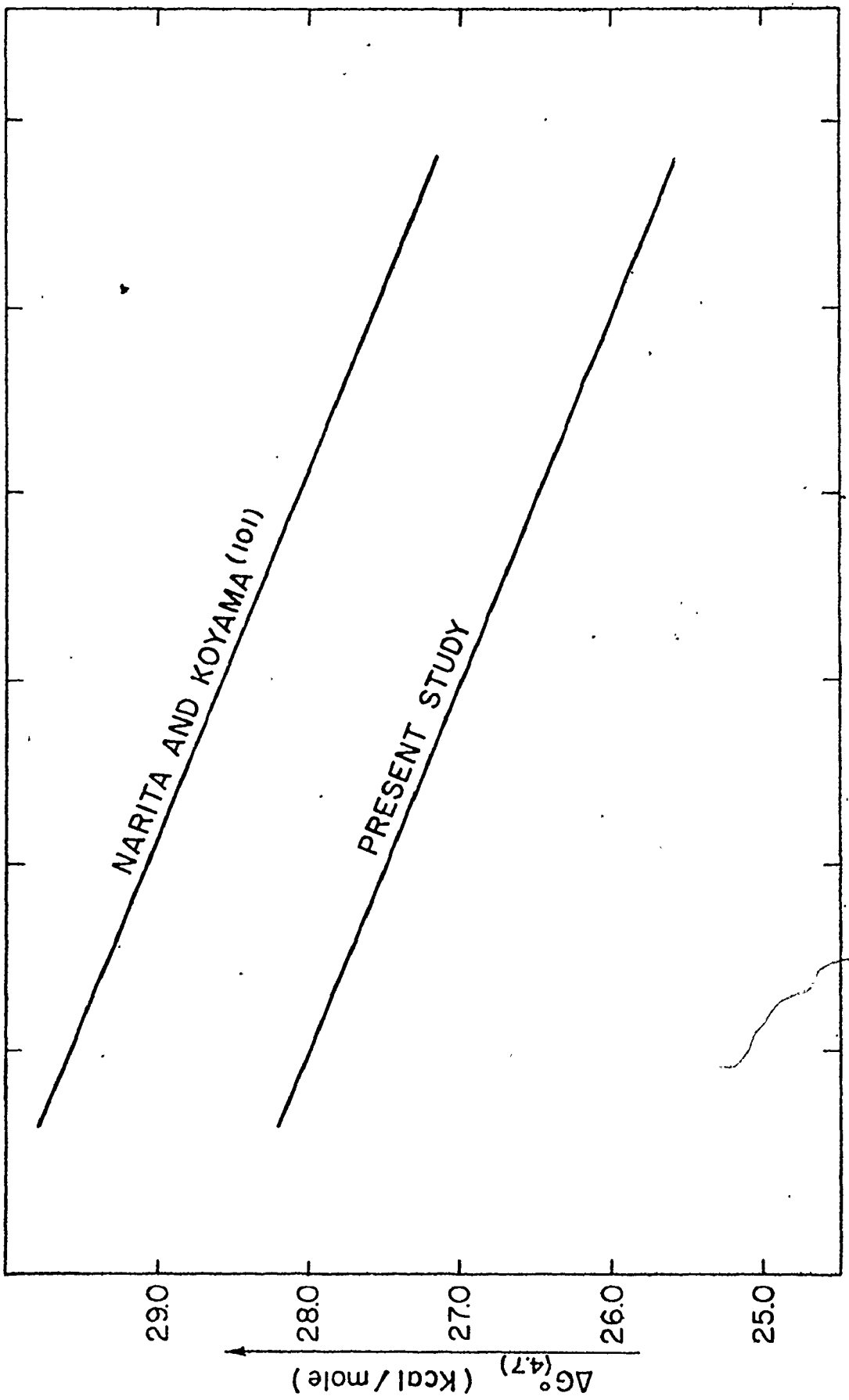

Figure 4.7 ΔG_T^o versus T for the reaction: $FeNb_2O_{6(s)} \rightleftharpoons Fe_{(\ell)} + 2NbO_{2(s)} + 20 \pm 1w/o$

b) Deoxidation products

The deoxidation products were identified using X-ray powder diffraction as described in Chapter 3.

Diffraction patterns taken from melts quenched during the plateau, gave lines corresponding to both oxides $FeNb_2O_6$ and NbO_2, whereas patterns taken before and after the plateau, gave lines corresponding to one oxide, NbO_2 or $FeNb_2O_6$ respectively. This is in agreement with the basic theory behind the study, i.e. that two deoxidation products coexist only at the plateau.

While very close agreement between the tabulated values for tetragonal NbO_2 and the X-ray diffraction patterns of the present work was found, there were problems in the identification of the higher oxide, the reason being that there is no powder diffraction data available for $FeNb_2O_6$. The only data available is for columbite: $(Fe,Mn)(Nb,Ta)_2O_6$. The present diffraction pattern, compares favourably with the pattern for columbite although there is a consistent slight shift in the diffraction lines. It was thought that this is convincing evidence for the existence of $FeNb_2O_6$, since columbite is basically $FeNb_2O_6$ with substitution of Fe with Mn and Nb with Ta in the orthorhombic lattice. A typical X-ray diffraction pattern from a sample taken after quenching from the plateau, is shown in Table 4.2.

Some ingots were sectioned and examined metallographically. Although there were always few inclusions, present, it was found that ingots containing $FeNb_2O_6$ contained more inclusions, than

TABLE 4.2

X-ray Diffraction Pattern from Fe-Nb-O Deoxidation Products

Line	d	Intensity	d due to NbO_2*	d due to Columbite**	Choice
1	2.942	vS		2.96	$FeNb_2O_6$
2	2.748	vS	2.745		NbO_2
3	2.416	W	2.40		NbO_2
4	2.537	W		2.53	$FeNb_2O_6$
5	2.369	S		2.38	$FeNb_2O_6$
6	2.29	W	2.589		NbO_2
7	1.917	S	1.926		NbO_2
8	1.804	S		1.77	$FeNb_2O_6$
9	1.728	S		1.721	$FeNb_2O_6$
10	1.683	S	1.689		NbO_2
11	1.571	W	1.568		NbO_2
12	1.537	vW		1.53	$FeNb_2O_6$
13	1.503	S		1.503	$FeNb_2O_6$
14	1.412	W	1.419		NbO_2

* ASTM powder file card 17-717

** ASTM Powder file card 16-337

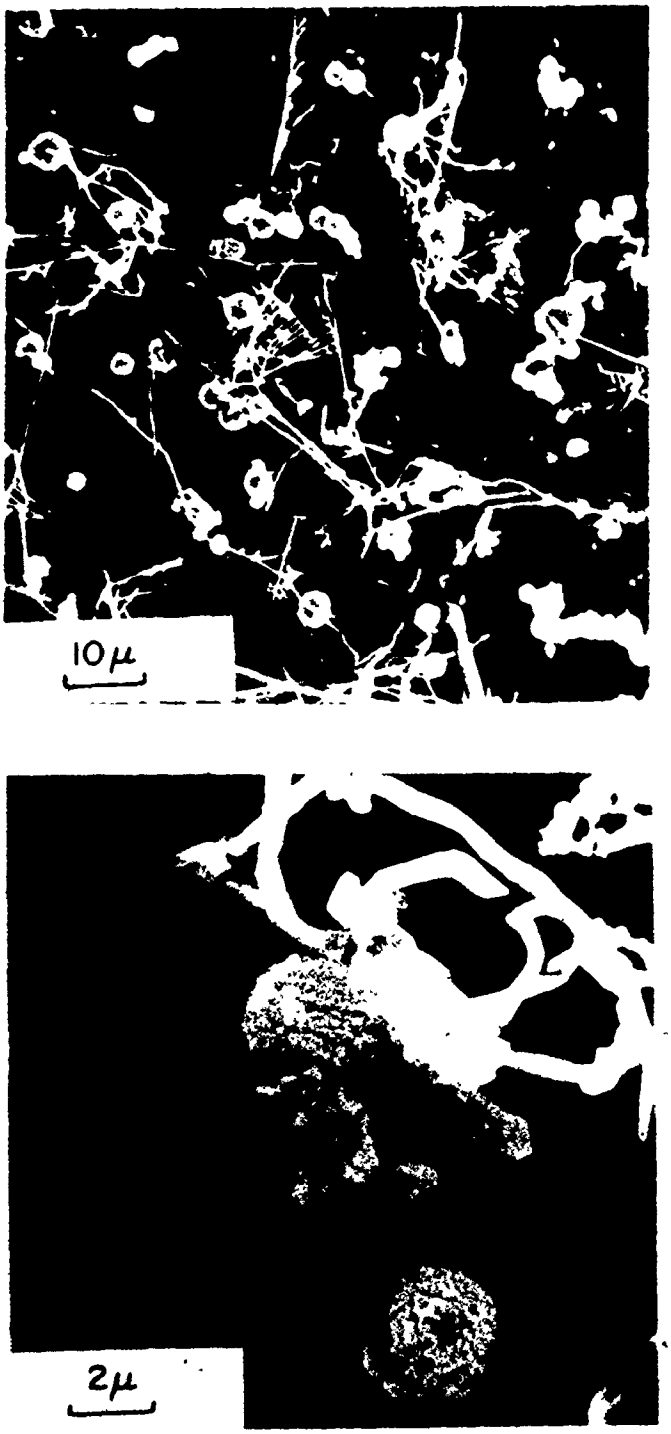

Figure 4.8 Morphology of inclusions in the Fe-Nb-O system

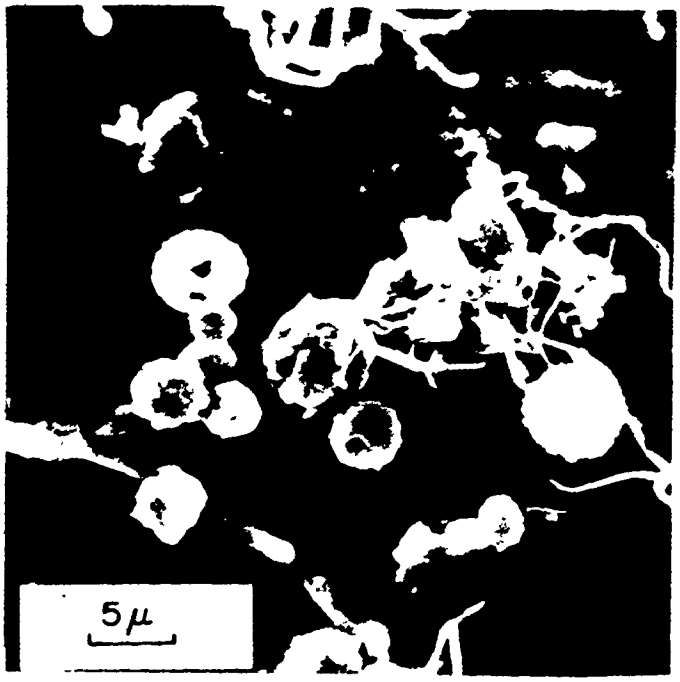

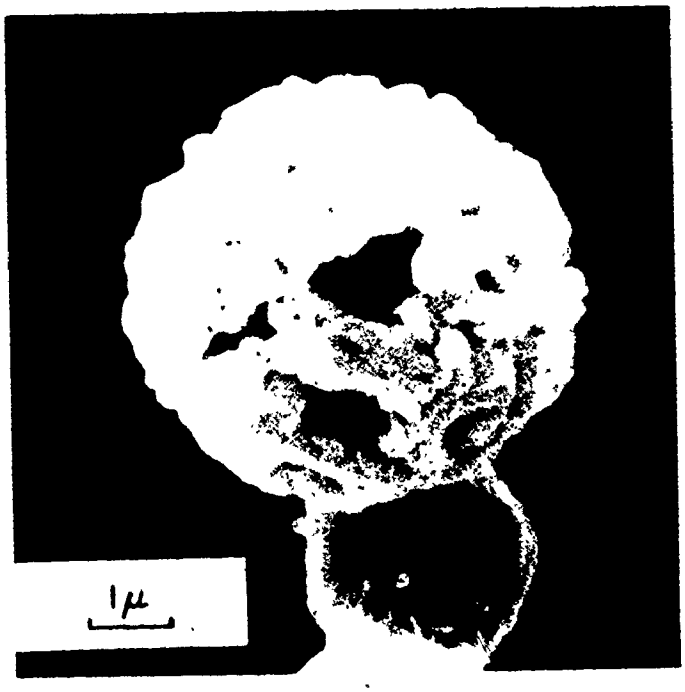

Figure 4.9 Morphology of inclusions in the Fe-Nb-O system

those in which NbO_2 was the only product. This is in agreement with the hypothesis[1] that higher oxides do not separate easily from the melt due to their lower interfacial tension with molten iron. The iodine etching technique discussed in Chapter 3 was used, and the samples after etching were examined in a scanning electron microscope. The inclusions were identified as niobates but their exact composition could not be determined as their small size, and the inability of the microprobe (Acton) to analyse for oxygen, made a quantitative examination impossible.

In Fig. 4.8 and 4.9 the morphology of these inclusions is shown. They look like spheres formed by the collision of numerous smaller particles some of which are of tetragonal or orthorhombic shape. Although these spheres look as if they were solid during the experiment, the thin filaments that accompany them could be formed as secondary deoxidation products during solidification.

4.4 Results in the Fe-Al-O system

(a) Transition point equilibrium

The experimental runs in the Fe-Al-O system are shown in Figures 4.10 to 4.14. $Mo|MoO_2$ was not used as a reference electrode in this study and no reducing runs were performed. It was apparent that the higher oxide, later identified as $FeAl_2O_4$, was very corrosive because in most cases the crucible failed, just at the beginning of the plateau. It was very difficult to obtain a run as shown in

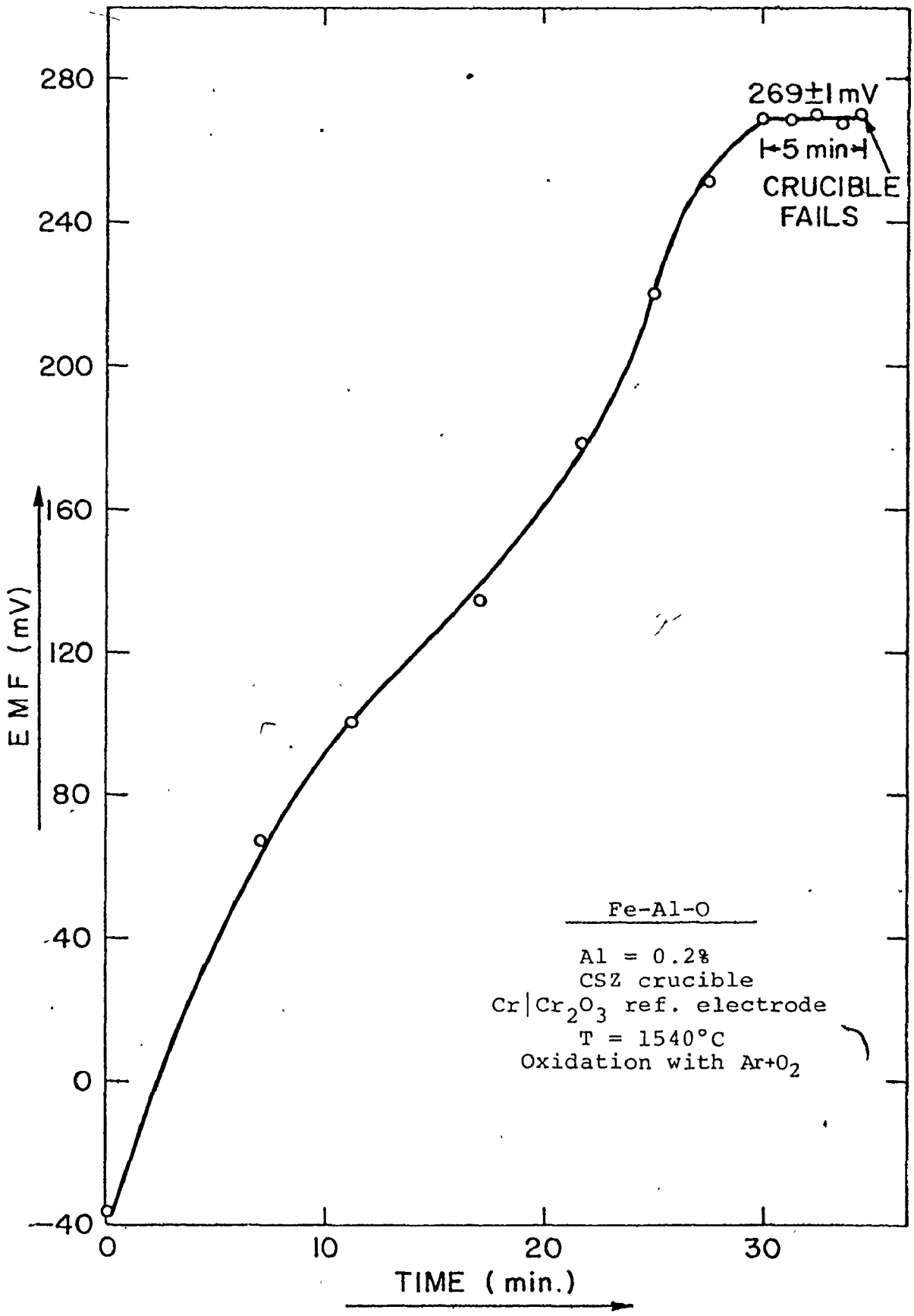

Figure 4.10 Experimental run in the Fe-Al-O system

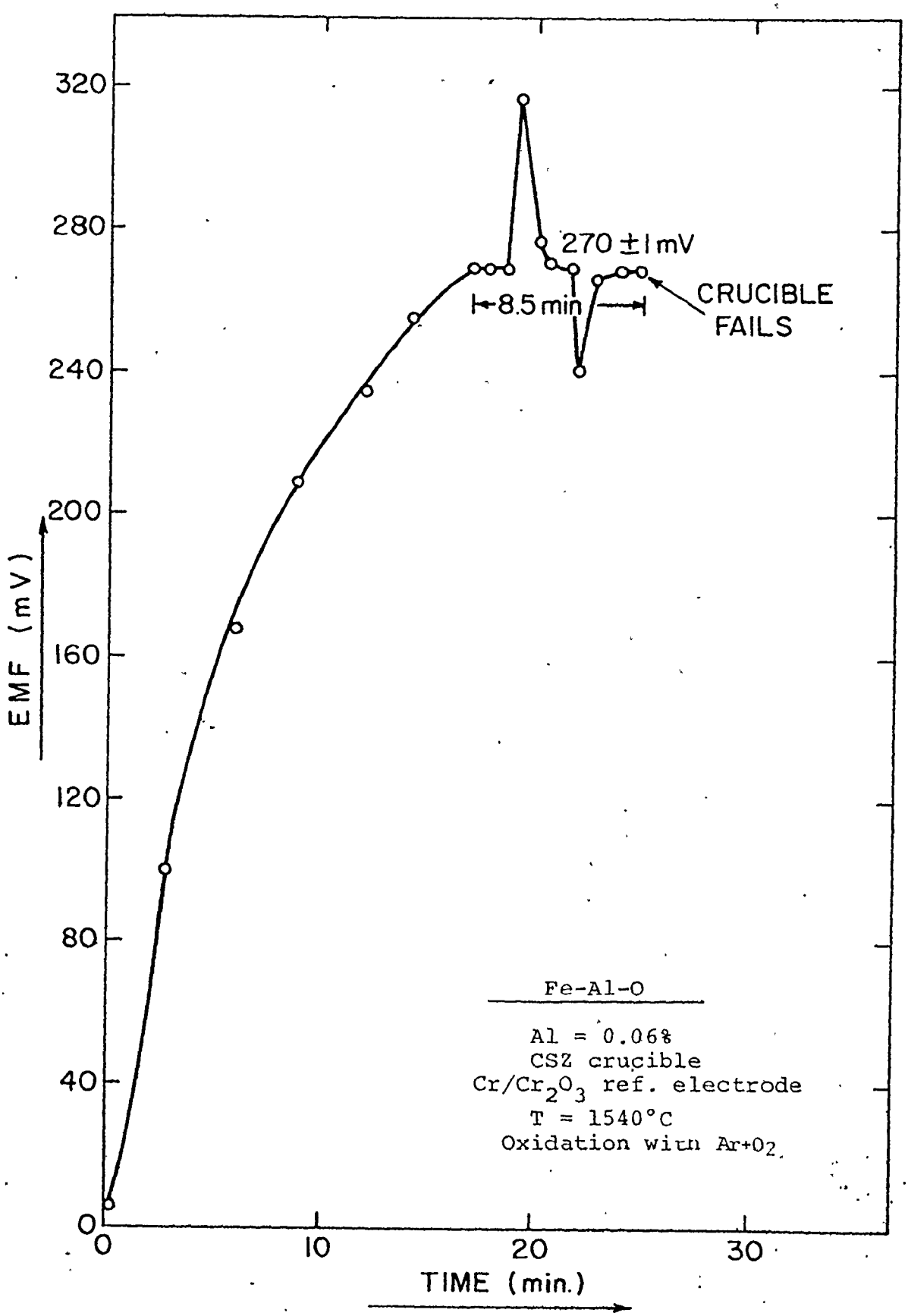

Figure 4.11 Experimental run in the Fe-Al-O system

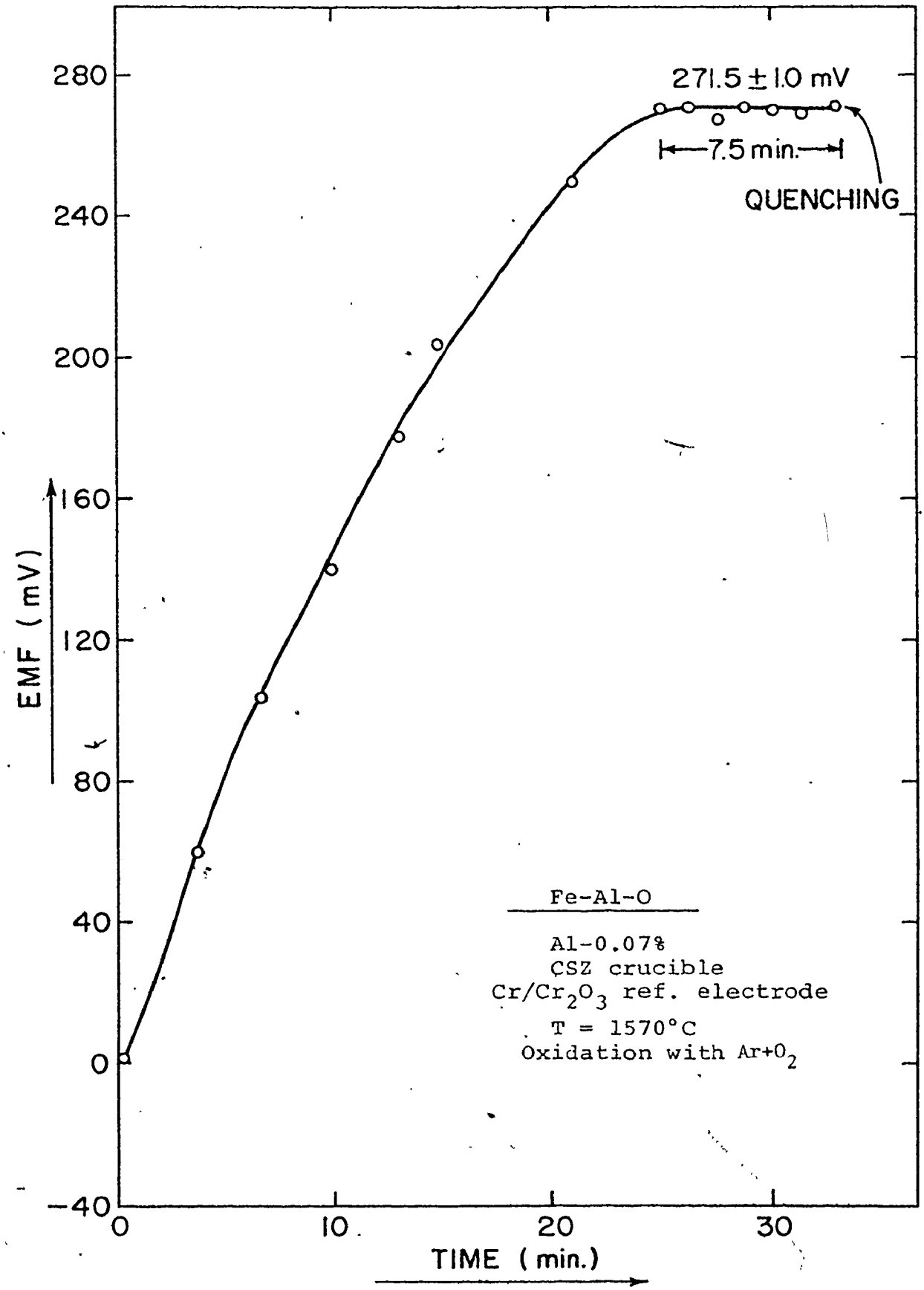

Figure 4.12 Experimental run in the Fe-Al-O system

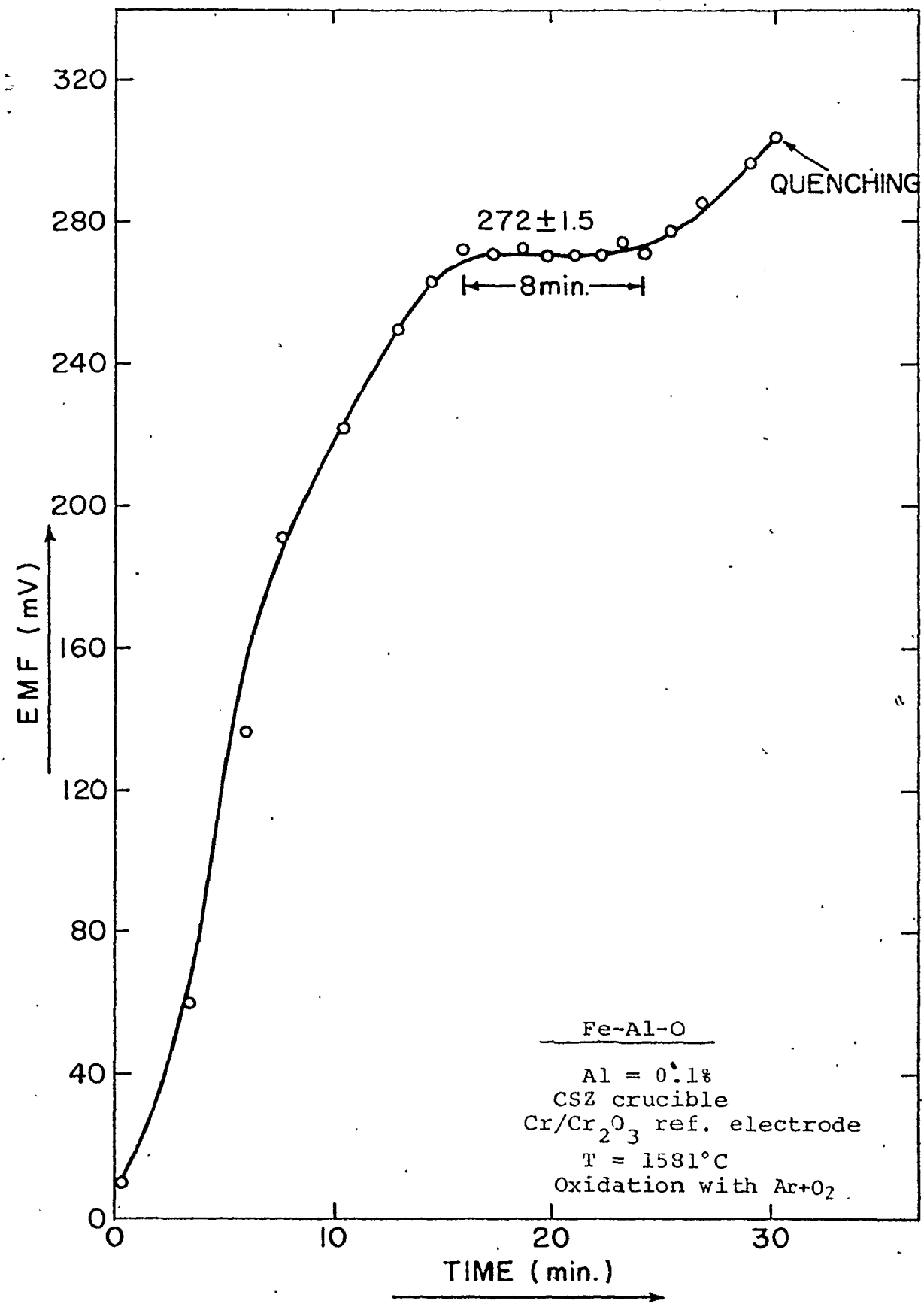

Figure 4.13 Experimental run in the Fe-Al-O system

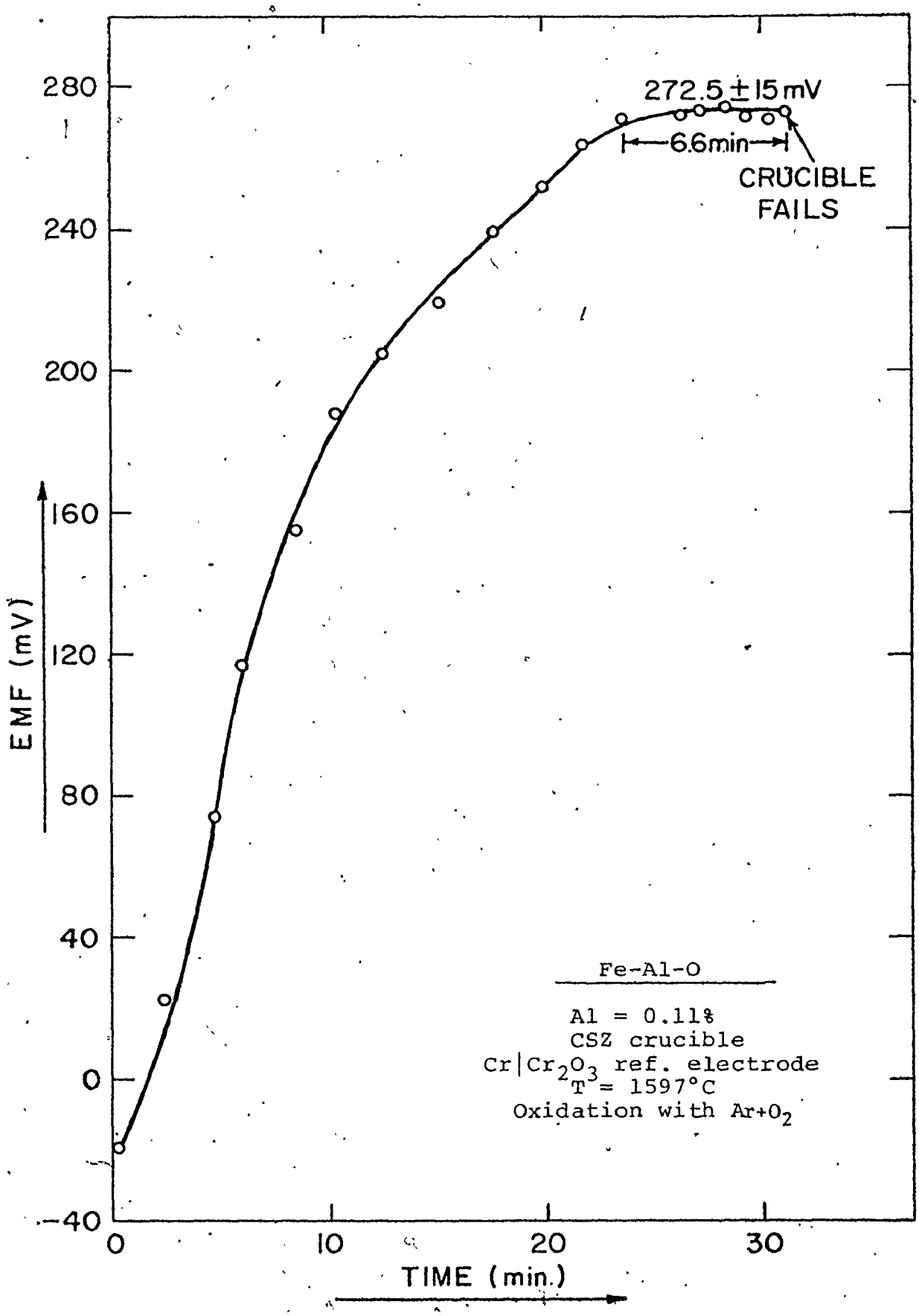

Figure 4.14 Experimental run in the Fe-Al-O system

Fig. 4.13 because of crucible failure. Understandably reducing experiments starting from an oxidised melt could not be performed. Again the plateaus are very well defined and very stable, the scatter in the measurements during the plateau, never exceeding ±1.5 mV.

The deoxidation products were identified, as is described below, as Al_2O_3 and $FeAl_2O_4$.

The reaction in equilibrium at the plateau can therefore be written as:

$$FeAl_2O_{4(s)} \rightleftarrows Fe_{(\ell)} + Al_2O_{3(s)} + \underline{O}_{\text{1w/o}} \qquad (4.16)$$

In Table 4.3, values of $\log h_O$ and ΔG°_T for reaction (4.16), as calcualted from the experimental results, are shown: In the same table, ΔG°_T for the reaction:

$$FeAl_2O_{4(s)} \rightleftarrows Fe_{(\ell)} + Al_2O_{3(s)} + \frac{1}{2} O_{2(g)} \qquad (4.17)$$

calculated by combining ΔG°_T for reaction (4.16) with equation (2.21), is also given. In Fig. 4.15, $\log h_O$ for the transition point, versus $\frac{1}{T}$ is plotted. Least square analysis of the experimental points, yields the following equation:

$$\log h_O = 4.70 - \frac{10910}{T} \qquad (4.18)$$

the estimated value of $\log h_O$ being in excellent agreement with the experimental results.

From equation (4.18) we can get ΔG°_T for reaction (4.16)

$$\Delta G^\circ_{(4.16)} = -RT\ell nh_O = 49910 - 21.50\ T \text{ cal} \quad (1540\text{-}1600^\circ C) \qquad (4.19)$$

TABLE 4.3

Experimental Results on the Fe-Al-O System

T°C	$\frac{1}{T} \times 10^4$ ($°K^{-1} \times 10^4$)	EMF (mV)	$\log h_O$	$\Delta G°_{T(4.16)}$ (cal/mole)	$\Delta G°_{T(4.17)}$ (cal/mole)
1540	5.516	269	-1.32	10950	40200
1540	5.516	270	-1.32	10900	40720
1570	5.426	271	-1.21	10240	39510
1581	5.394	272	-1.18	9960	39240
1597	5.348	272.5	-1.12	9610	38900

4.16: $FeAl_2O_{4(s)} \rightleftarrows Fe_{(\ell)} + Al_2O_{3(s)} + \underline{O}$ lw/o

4.17: $FeAl_2O_{4(s)} \rightleftarrows Fe_{(\ell)} + Al_2O_{3(s)} + \frac{1}{2} O_{2(g)}$

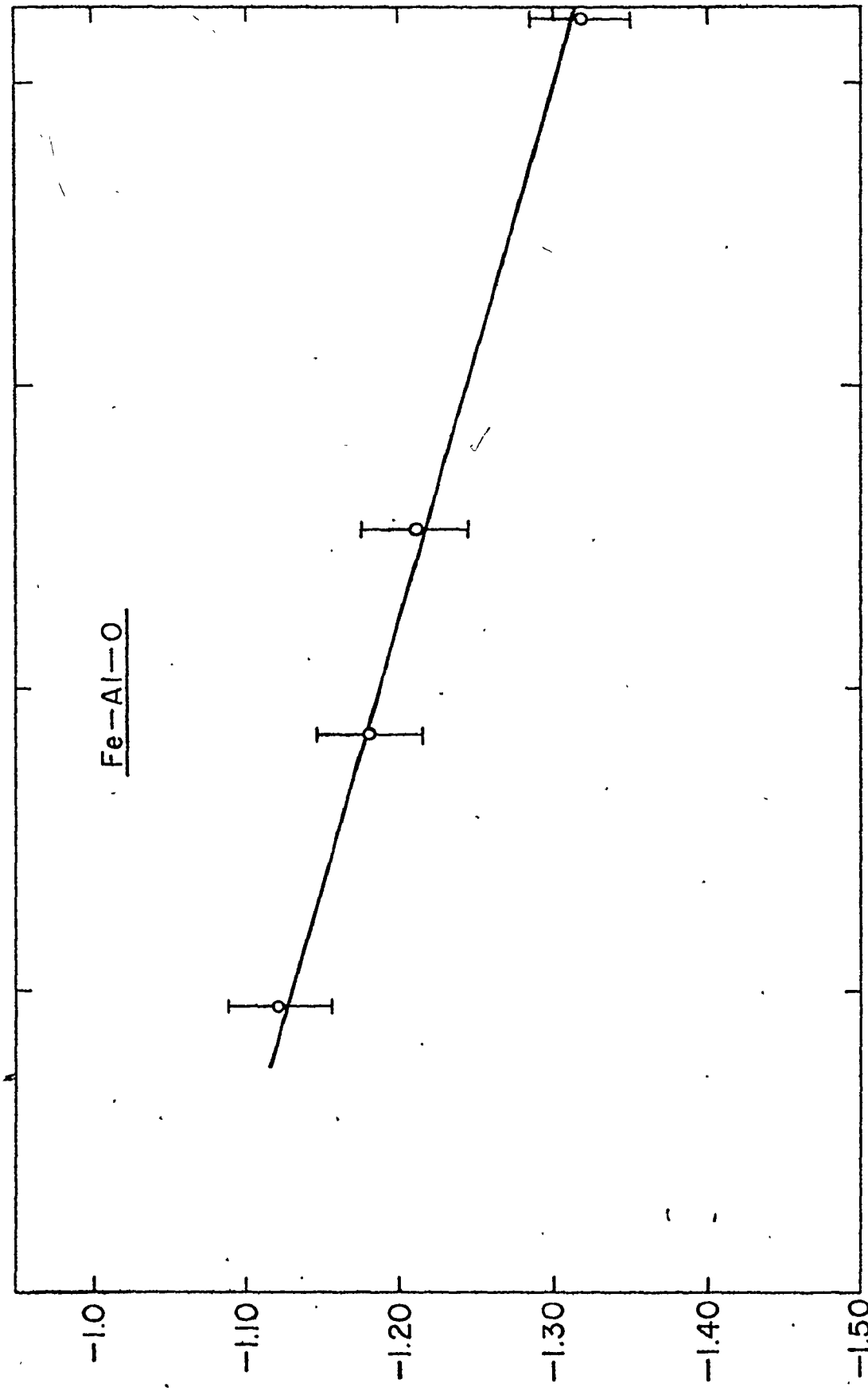

Figure 4.15 Logh_o versus $\frac{1}{T}$ for the reaction: $FeAl_2O_{4(s)} \rightleftarrows Fe_{(\ell)} + Al_2O_{3(s)} + \underline{O}$ lw/o

Combining (4.19) with (2.21) we may write for reaction (4.17):

$$\Delta G^{\circ}_{T(4.17)} = \Delta G^{\circ}_{T_{(4.16)}} - \Delta G^{\circ}_{T_{(2.20)}} \qquad (4.20)$$

$$\Delta G^{\circ}_{(4.17)} = 77910 - 20.12\ T \text{ cal } (1540\text{-}1600^{\circ}C) \qquad (4.21)$$

(b) Third law analysis of data

For a better evaluation of the results in the Fe-Al-O system, a third law analysis was carried out in the following way.

Considering reaction (4.17) the Gibbs energy function, gef_T, given by:

$$gef_T = \frac{(G^{\circ}_T - H^{\circ}_{298})}{T} \qquad (4.22)$$

was determined for alumina, iron and oxygen using JANAF Tables[141] and the corresponding data for hercynite[108]. ΔH°_{298} was then calculated from the free energy experimental data using the equation:

$$\Delta H^{\circ}_{298} = \Delta G^{\circ}_T - T\Delta gef_T \qquad (4.23)$$

where

$$\Delta gef_T = gef_T(Al_2O_3) + gef_T(Fe) + \tfrac{1}{2}gef_T(O_2) - gef_T(FeAl_2O_4) \qquad (4.24)$$

The results of the calculations for the change in the Gibbs energy function (Δgef_T) and ΔH°_{298} are given in Table 4.4. The average value of ΔH°_{298} obtained is 71730 cal/mole $FeAl_2O_4$, the standard deviation of the data being 300 cal/mole $FeAl_2O_4$.

TABLE 4.4

Third Law Analysis of Data for Reaction 4.17

T°K	ΔG°_T (cal/mole) experimental	$T_x \Delta gef_T$ cal/mole	ΔH°_{298} cal/mole	$\Delta H^\circ_{298} - (\Delta H^\circ_{298})_{av}$ cal/mole
1813	40200	-31530	-71730	0
1813	40720	-31530	72250	+520
1843	39510	-32100	71610	-120
1854	39240	-32310	71550	-180
1870	38900	-32620	71520	-210

Note: $(\Delta H^\circ_{298})_{av}$ = 71730 cal/mole $FeAl_2O_4$

In Fig. 4.16 the values of ΔH°_{298} are plotted against the experimental temperature and in the same figure, the average ΔH°_{298} and the 95% confidence limits have been indicated. Having found the average ΔH°_{298} from the present data, ΔG°_T for reaction 4.17 was recalculated using the relation:

$$\Delta G^\circ_T = \Delta H^\circ_{298} + T\Delta gef_T \quad (1540\text{-}1600°C) \qquad (4.25)$$

In Figure 4.17 the $\Delta G^\circ_{T(4.17)}$ thus obtained is plotted versus temperature. The points obtained can be represented by the equation:

$$\Delta G^\circ_{T(4.17)} = 74840 - 19.11T \text{ cal/mole} \quad (1540\text{-}1600°C) \qquad (4.26)$$

determined by least square analysis. In the same figure the intial equation representing $\Delta G^\circ_{T(4.17)}$ is plotted to indicate the order of the correction using the third law analysis.

Results obtained by Chan et al.[134], Pillay et al[132] McLean and Ward[133] and Kim and McLean[173] are also indicated in Fig. 4.17 for comparison. Results[133,173] have been taken from Table 2.5 and combined with equation (2.21) to give ΔG°_T for reaction (4.17). The results of Chan et al. and Pillay et al. have been directly taken from Table 2.5.

(c) Data for the reaction: $FeAl_2O_{4(s)} \rightleftarrows Fe_{(\ell)} + 2\underline{Al}_{\text{1w/o}} + 4\underline{O}_{\text{1w/o}}$

Having determined by third law analysis the relation between $\Delta G^\circ_{T(4.17)}$ and temperature (equation 4.26) $\Delta G^\circ_{T(4.16)}$

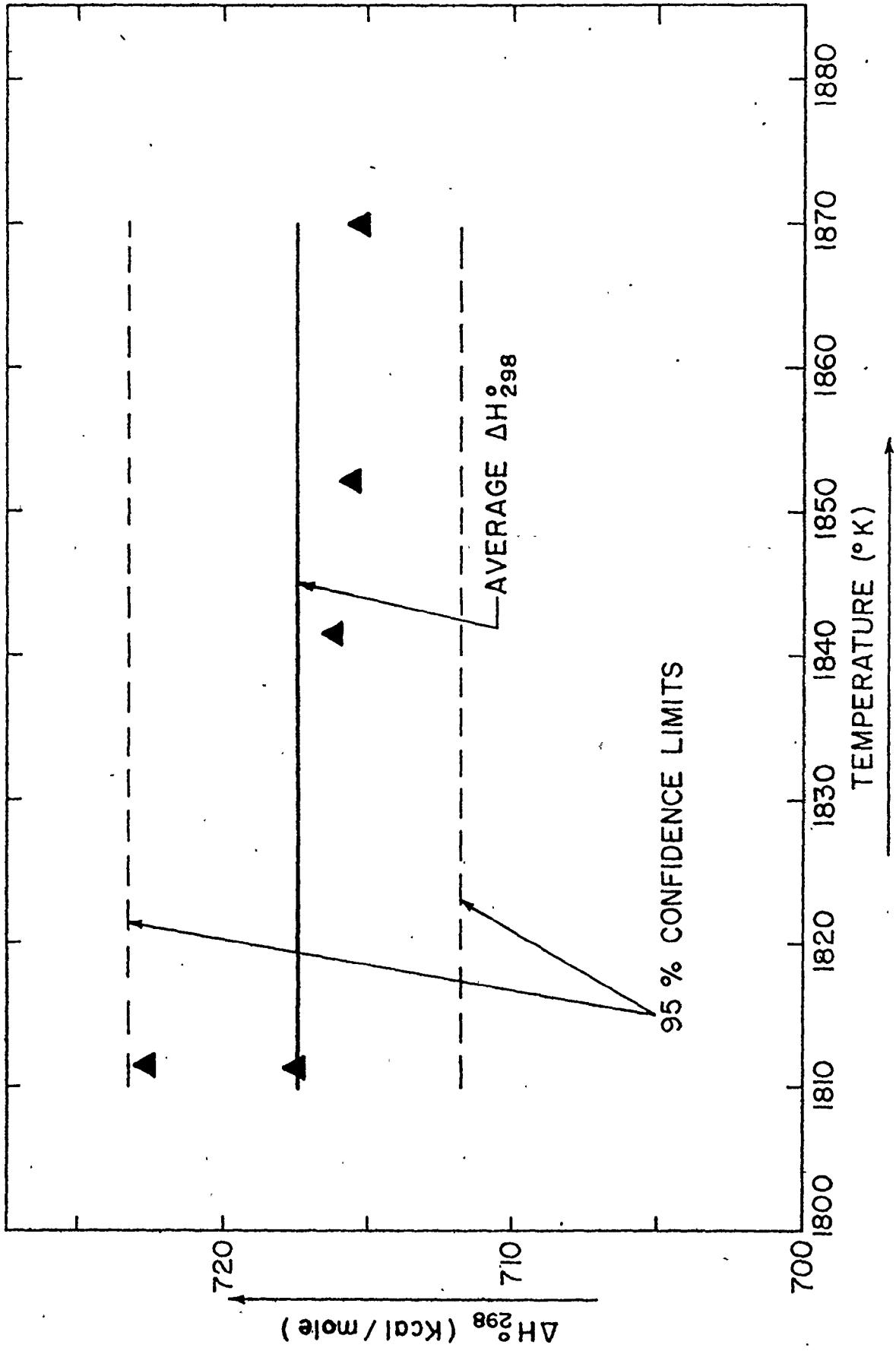

Figure 4.16 ΔH°_{298} for the reaction: $FeAl_2O_4 \rightarrow Fe + Al_2O_3 + \frac{1}{2}O_2$, calculated by third law analysis

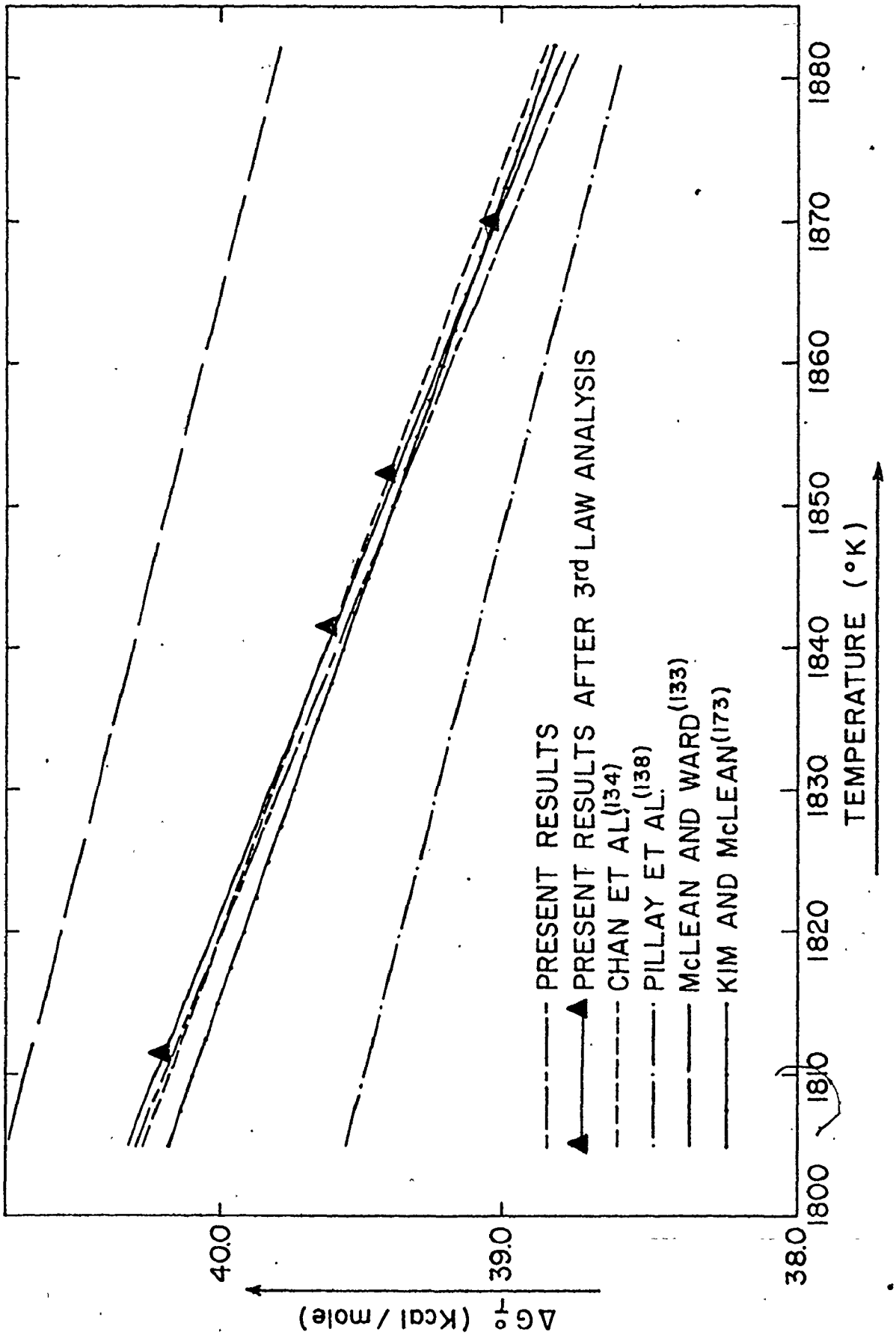

Figure 4.17 ΔG_T^o versus T for the reaction: $FeAl_2O_{4(s)} + Fe_{(\ell)} + Al_2O_{3(s)} + \underline{O}$ 1w/o

as a function of temperature may be recalculated by combining (4.26) with (2.21):

$$\Delta G^{\circ}_{T_{(4.16)}} = 46840 - 19.80\ T \text{ cal/mole } (1540\text{-}1600^{\circ}C) \quad (4.27)$$

ΔG°_{T} for the reaction:

$$FeAl_2O_{4(s)} \rightleftarrows Fe_{(\ell)} + 2\underline{Al}_{\text{1w/o}} + 4\underline{O}_{\text{1w/o}} \quad (4.28)$$

may be calculated from equation (4.27) using the relation

$$\log[h^2_{Al}.h^3_O] = -\frac{62160}{T} + 20.86 \quad (2.92)$$

given by Ghosh[111].

The resulting equation is:

$$\Delta G^{\circ}_{T_{(4.28)}} = 331220 - 115.23T \text{ cal } (1540\text{-}1600^{\circ}) \quad (4.29)$$

In Fig. 4.18, values of $\Delta G^{\circ}_{T(4.28)}$ taken from equation (4.29) are plotted versus temperature. In the same figure, the equations from study by Chan et al., Pillay et al., McLean and Ward and Kim and McLean, taken from Table 2.5, are given for comparison.

From equation (4.29)

$$\log K_{(4.28)} = -\frac{72400}{T} + 25.19 \quad (4.30)$$

Since $\log K_{(4.28)} = \log[h^2_{Al}.h^4_O]$

values of h_O from equation (4.27) may be used to find the relation of $\log h_{Al}$ versus temperature for the transition point:

$$\log h_{Al} = -\frac{15720}{T} + 3.94 \quad (4.31)$$

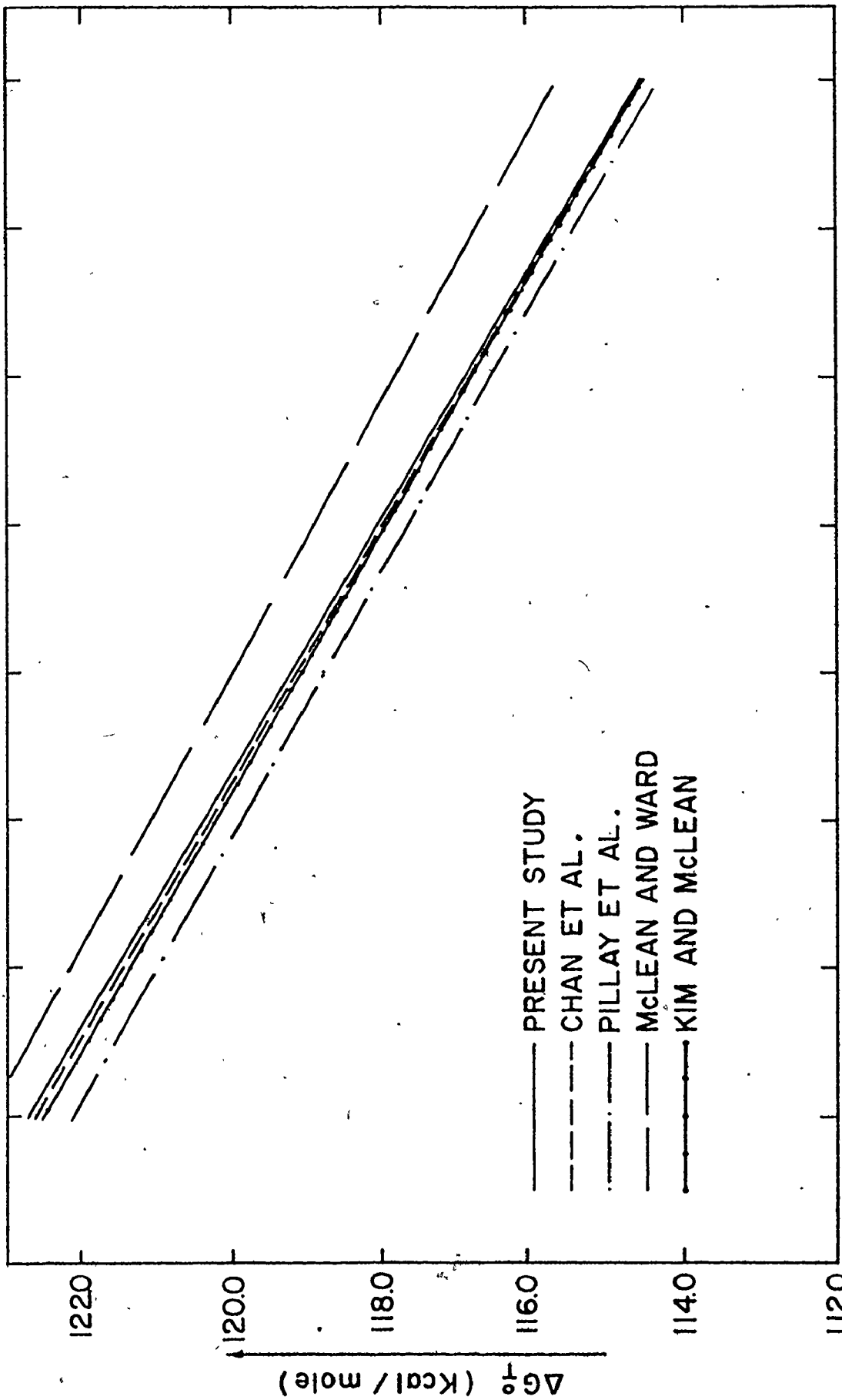

Figure 4.18 ΔG°_{T} versus T for the reaction: $FeAl_2O_4(s) \pm Fe_{(\ell)} + 2\underline{Al}$ 1w/o + 4$\underline{O}$ 1w/o

TABLE 4.5

X-ray Diffraction Pattern from Fe-Al-O Deoxidation Products

Line	d	Intensity	d due to Al_2O_3*	d due to $FeAl_2O_4$**	Choice
1	2.866	S		2.87	$FeAl_2O_4$
2	2.554	m	2.552		Al_2O_3
3	2.466	vS		2.45	$FeAl_2O_4$
4	2.396	m	2.379		Al_2O_3
5	2.092	vS	2.085		Al_2O_3
6	2.034	W		2.02	$FeAl_2O_4$
7	1.738	W	1.740		Al_2O_3
8	1.606	m	1.601		Al_2O_3
9	1.574	mS		1.56	$FeAl_2O_4$
10	1.445	vS		1.43	$FeAl_2O_4$
11	1.407	W	1.404		Al_2O_3
12	1.374	W	1.374		Al_2O_3
13	1.241	m		1.23	$FeAl_2O_4$
14	1.175	vW	1.189		Al_2O_3
15	1.148	vW	1.1470		Al_2O_3

* ASTM powder file card 10-133

** ASTM powder file card 3-0889

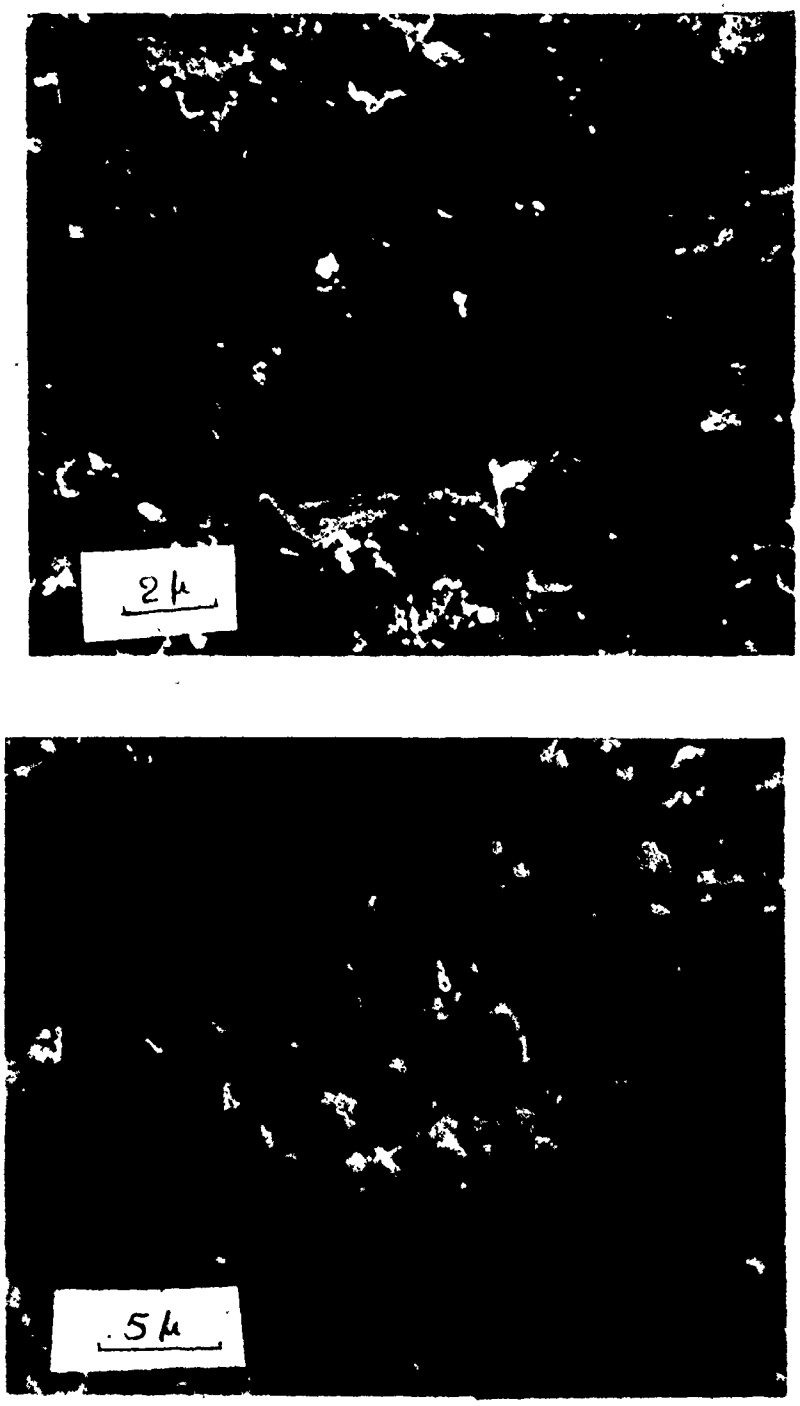

Figure 4.19 Morphology of inclusions in the Fe-Al-O system

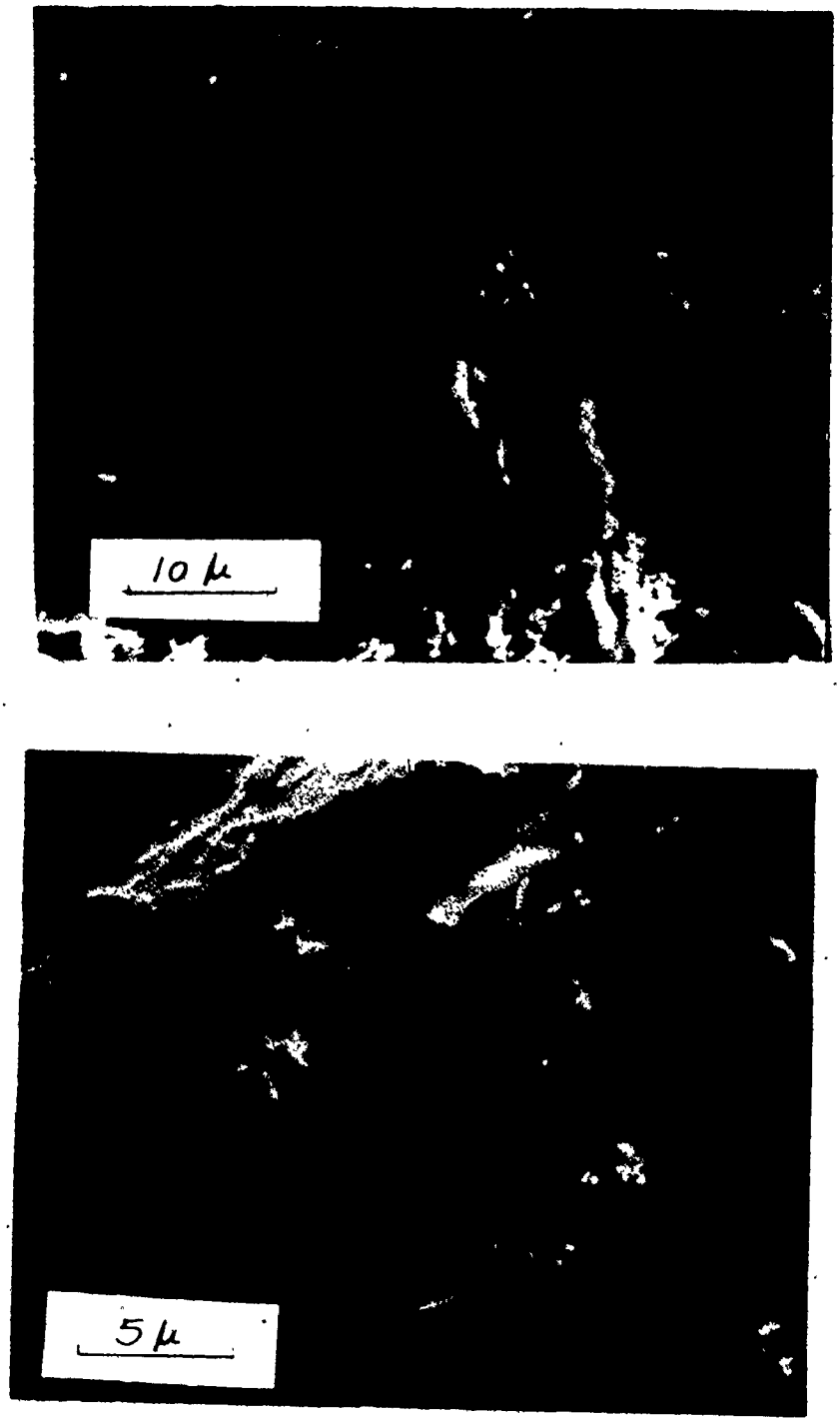

Figure 4.20 Morphology of inclusions in the Fe-Al-O system

(d) Deoxidation products

For the identification of the deoxidation products in the system Fe-Al-O, a similar procedure to that described for the Fe-Nb-O system was used. In this case X-ray diffraction data for Al_2O_3 and $FeAl_2O_4$ was available and, therefore, identification was easier.

A typical X-ray diffraction pattern from a sample taken after quenching from the plateau, is given in Table 4.5.

The iodine etching technique was used again to determine the morphology of surface inclusions and examples of scanning electron micrographs are shown in Fig. 4.19 and 4.20. The familiar shape of alumina and hercynite inclusions described by Turkdogan[21] and other workers[1] can be easily recognized.

4.5 Results in the Fe-Al-Mn-O system

The effect of Mn on the Fe-Al-O system was studied by determining the change in the oxygen potential of the transition point, as a function of the Manganese content in the melt, at a temperature of 1550°C. The results of the experimental runs are shown in Figures 4.21 to 4.24.

Analysis for manganese presented a problem as it was difficult to separately determine the manganese content in solution and that in the form of iron-manganese aluminates. However, according to the basic theory of the present technique, and assuming that under the experimental condition, the melt was never far from equilibrium, at the beginning of

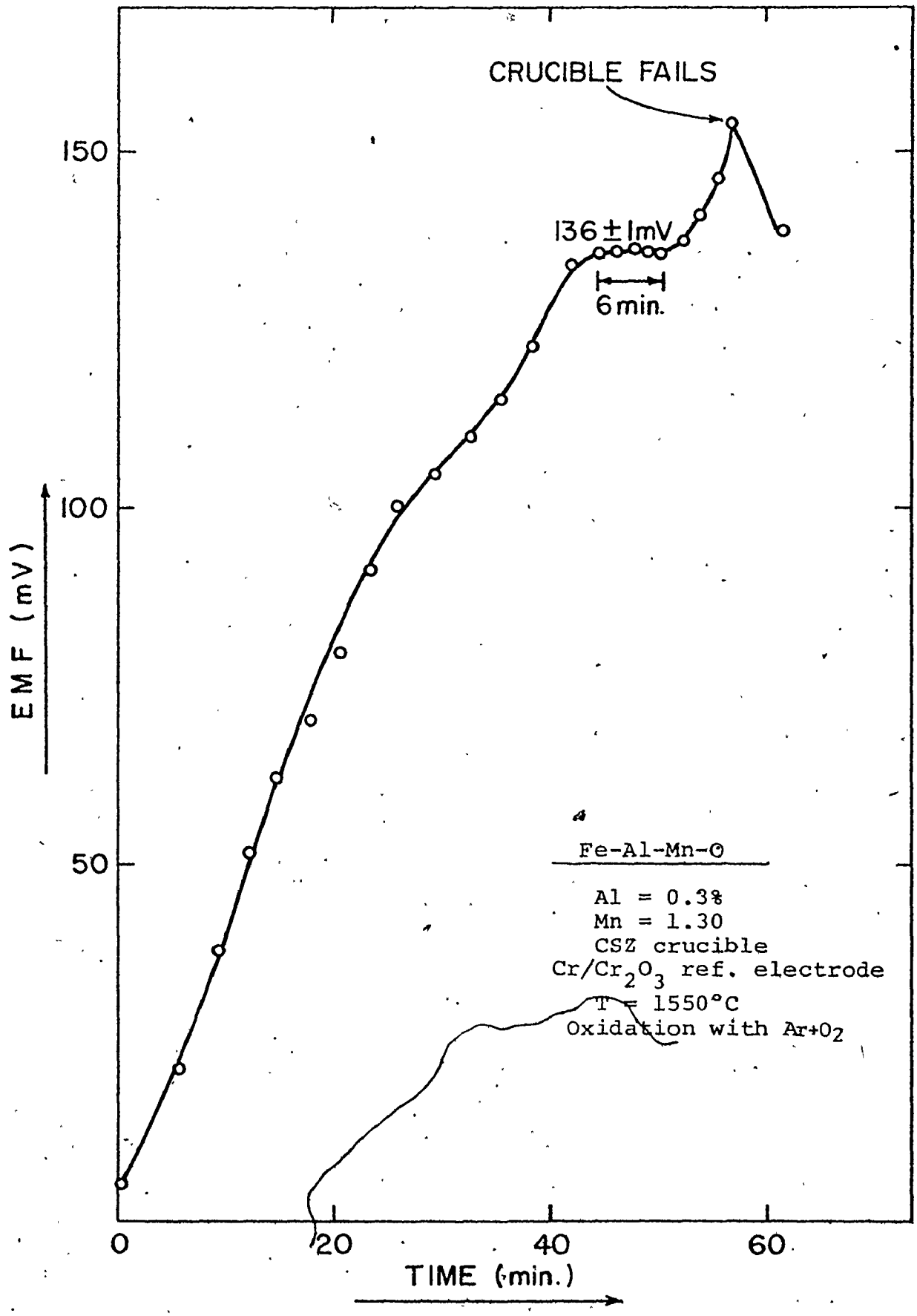

Figure 4.21 Experimental run in the Fe-Al-Mn-O system

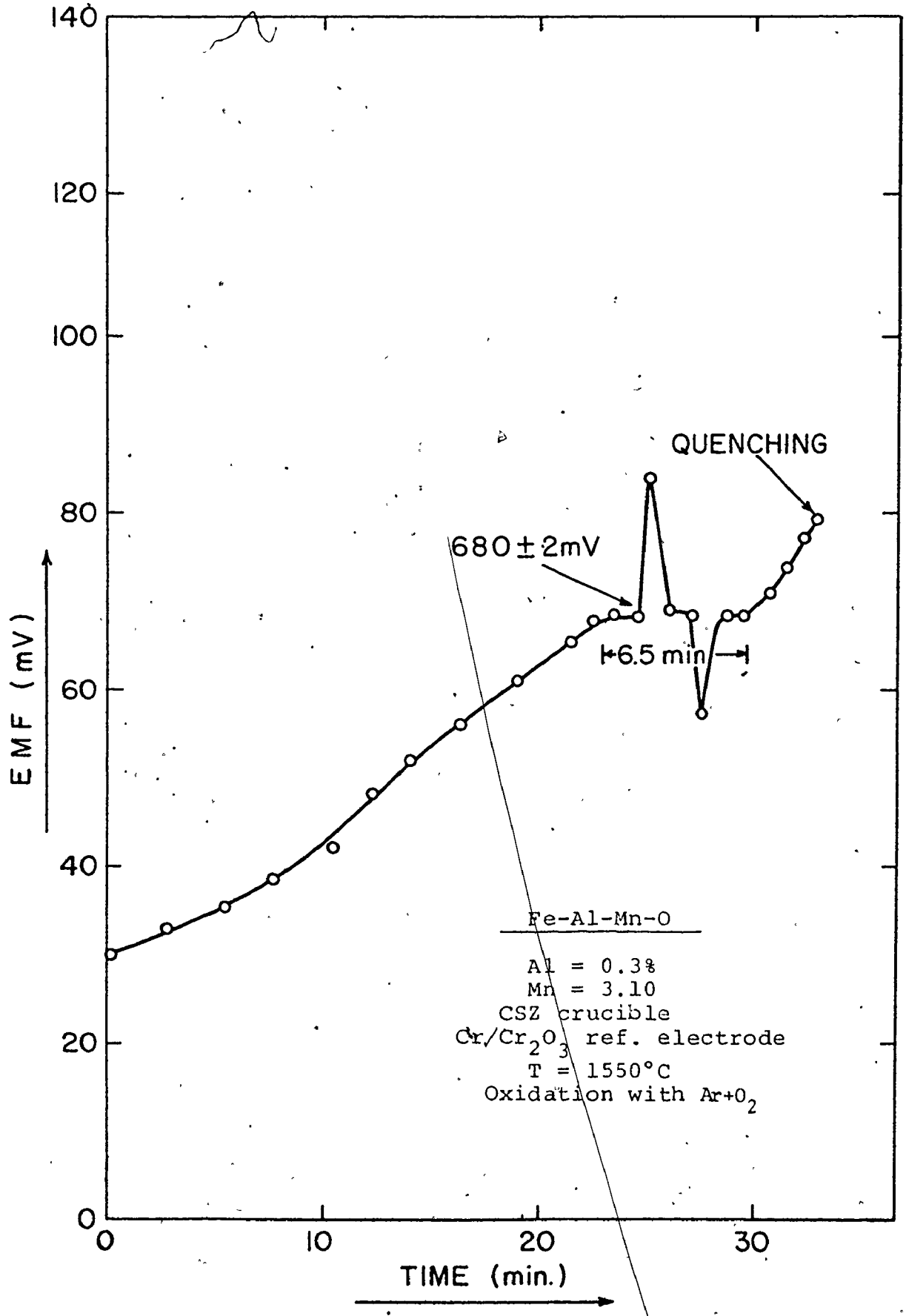

Figure 4.22 Experimental run in the Fe-Al-Mn-O system

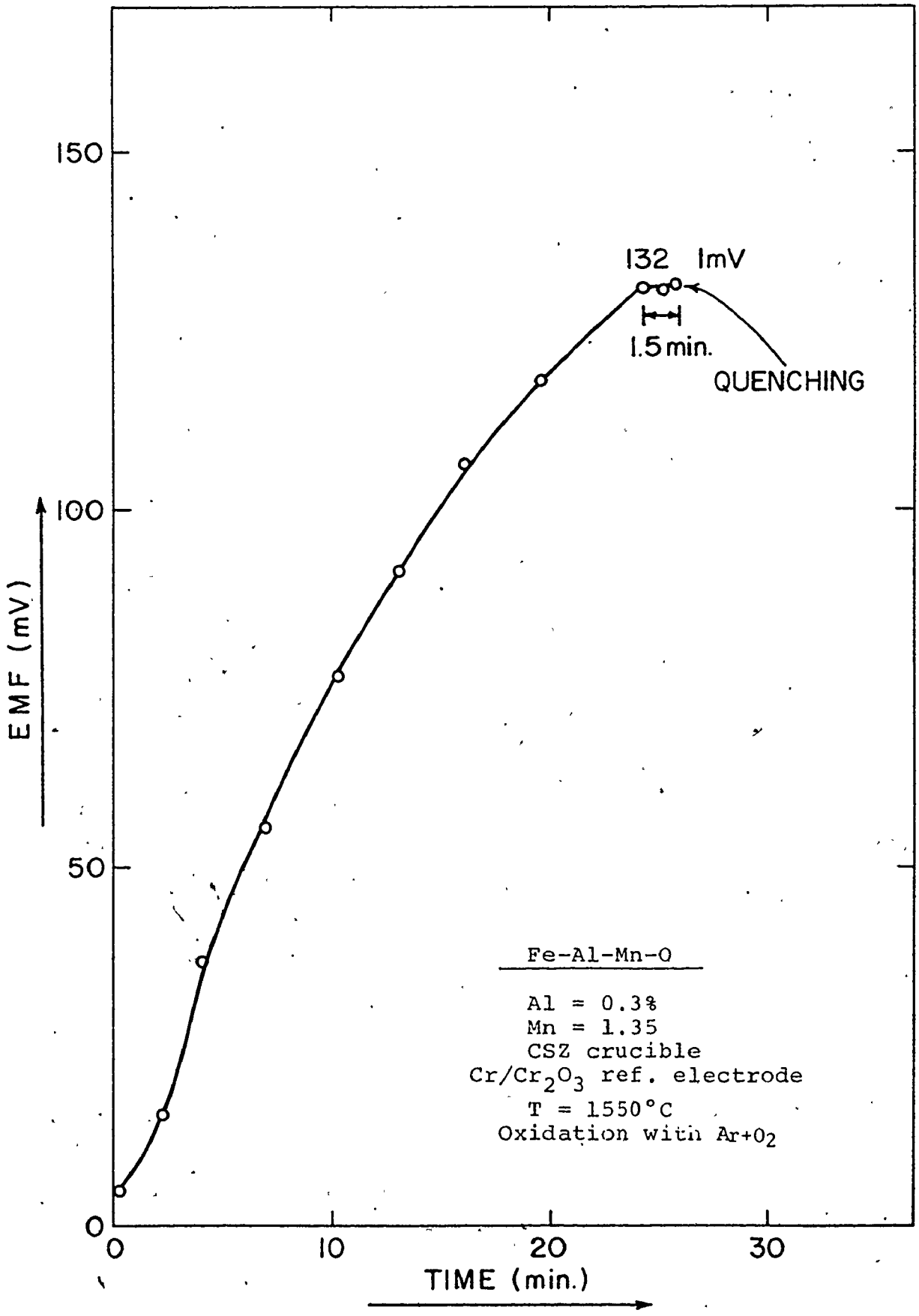

Figure 4.23 Experimental run in the Fe-Al-Mn-O system

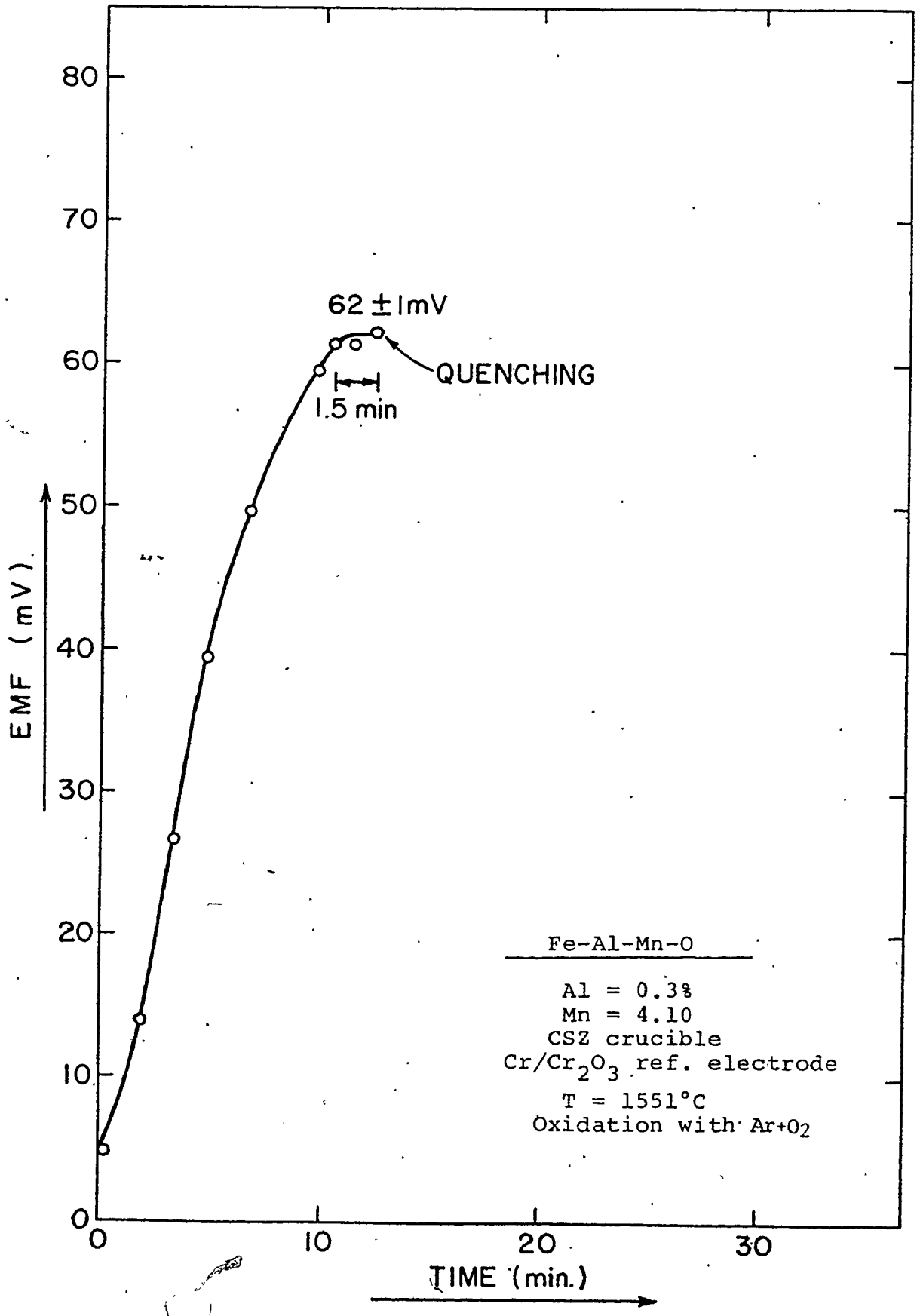

Figure 4.24 Experimental run in the Fe-Al-Mn-O system

a plateau only alumina is present, the whole manganese content being in solution. As the oxidation proceeds, the manganese combines with iron and alumina to produce iron-manganese aluminates, thus decreasing the content in solution in the melt. Analysis for total manganese, in melts quenched from any oxidation state, gives therefore the manganese content in solution at the beginning of the plateau. In the present study, the total Mn was determined either in melts quenched from the superoxidised state, Fig. 4.21 and 4.22 or in melts quenched just at the beginning of the plateau, Figs. 4.23 and 4.24.

The results, together with values of $\log h_O$ at the plateaus observed, are given in Table 4.6. In the same table, values of $\log h_{Al}$ for the plateaus, calculated using $\log h_O$ of the present experiments and Ghosh's[111] data for $[h_{Al}^2 . h_O^3]$, are given. In Fig. 4.25, values of $\log h_O$ and $\log h_{Al}$ of the plateaus, are plotted versus the manganese content of the melt at the beginning of iron-manganese aluminate formation. It is apparent that the effect of Mn, in decreasing the value of $\log h_O$ at the plateau, is decreasing with increasing manganese and becomes insignificant at manganese contents of more than 3.5%.

In Fig. 4.26 the deoxidation product morphology in the system Fe-Mn-Al-O is shown. The samples were iodine etched and examined by a scanning electron microscope.

TABLE 4.6

Effect of Mn on Al_2O_3-(Fe,Mn)O.Al_2O_3 transition point

T	Mn wt%	EMF (mV)	$logh_O$	$logh_{Al}$
1550	0	270*	-1.28*	-4.70
1550	1.30	136	-2.02	-3.59
1550	1.35	132	-2.05	-3.54
1550	3.13	68	-2.40	-3.02
1550	4.10	62	-2.43	-2.97

*calculated from equation 4.18

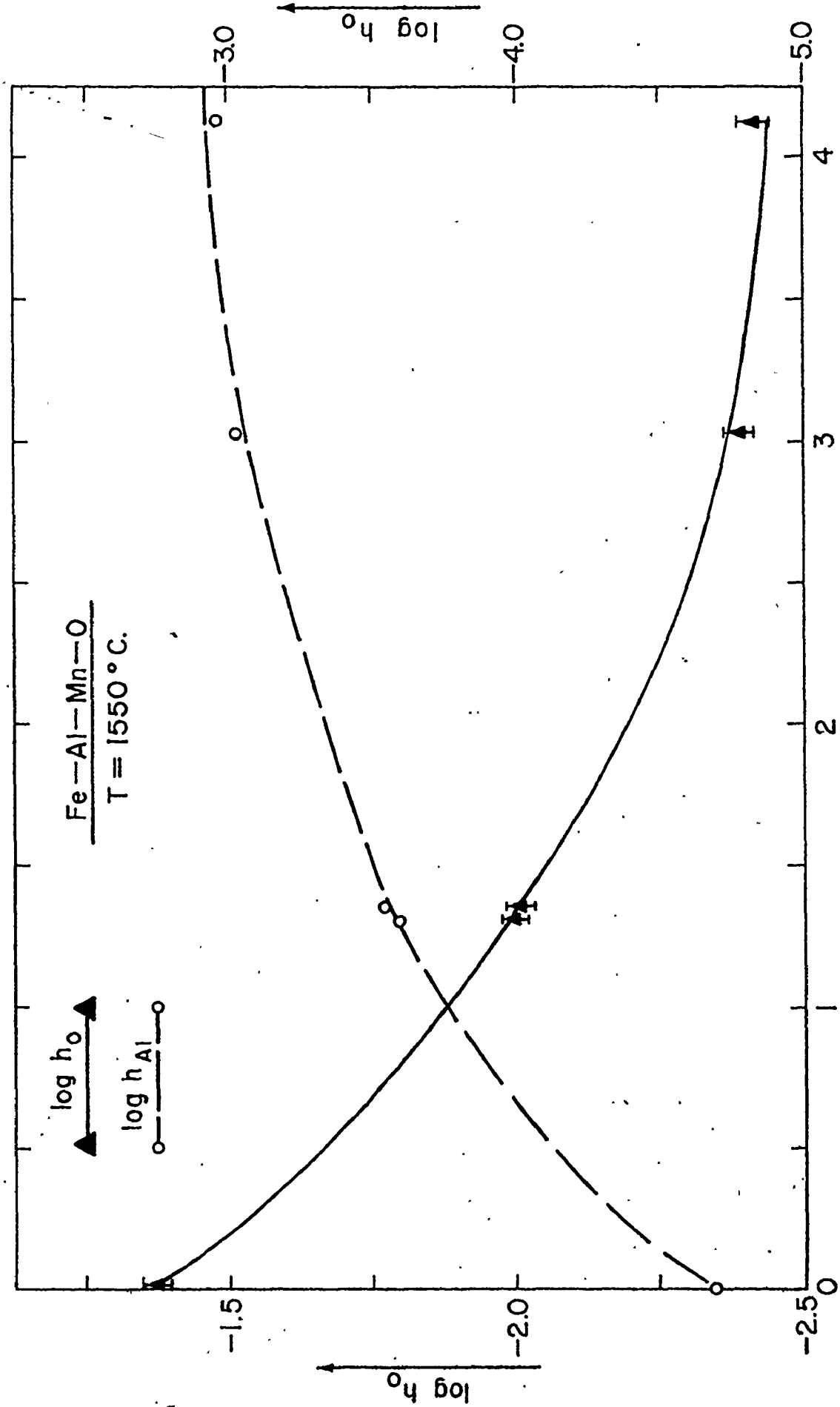

Figure 4.25 Logh_O and logh_{Al} versus [%Mn] at 1550°C, for the transition Al_2O_3 -(Fe,Mn)O.Al_2O_3

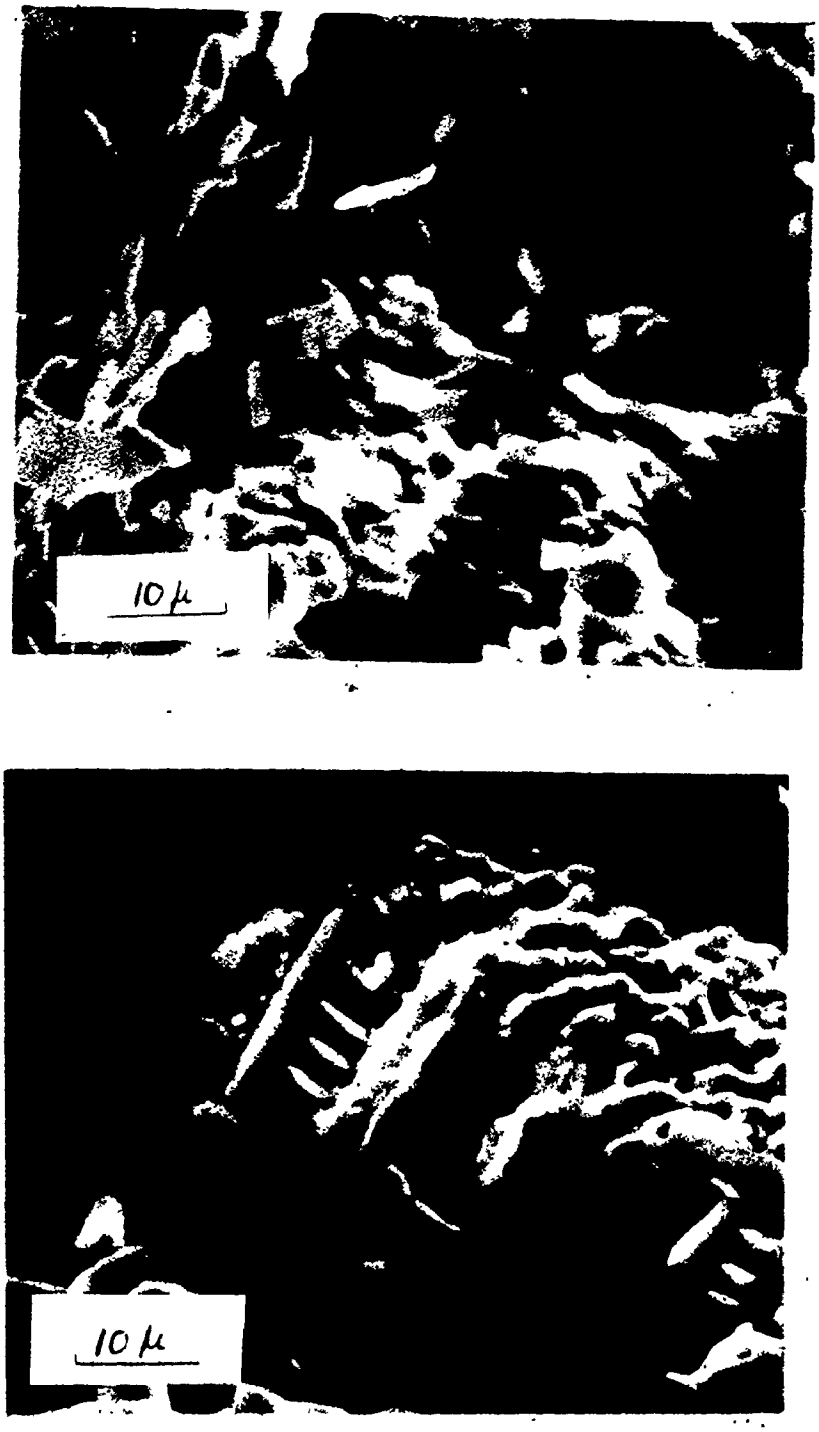

Figure 4.26 Inclusion morphology in the Fe-Al-Mn-O system

CHAPTER V

DISCUSSION

5.1 Introduction

In this chapter, the present experimental technique is discussed and the precautions taken to avoid any possible sources of error are described.

The uncertainty in the experimental results is also discussed in this chapter.

A detailed discussion of the results for the different deoxidation systems is given, and comparisons made with results of previous investigations.

5.2 The concentration cell

In Chapter 3, the concentration cell used in this experimental study is described. The main advantage in using such a cell is that measurements can be made continuously, in contrast with oxyprobe measurements where only one measurement is possible. The accuracy of the results produced by this technique is believed to be superior than conventional electrochemical techniques for the following reasons:

a) The solid electrolyte is the crucible itself, thus eliminating any interaction of the melt with less stable crucible material, such as alumina for example.

b) The cermet lead eliminates any Mo dissolution in the melt, thus avoiding contamination of the melt as occured in other studies[3,6]. Some of the melts were analysed for Mo, using the atomic absorption technique and the analysed Mo contents were never greater than 0.02%.

c) The deoxidation products were not artificially imposed on the melt, but were actually produced during the course of the experiment. At the transition point there exists a thermodynamic equilibrium with phases which are undoubtedly stable under the given experimental conditions. Another point to be stressed here is the fact that undetermined intermediate deoxidation products, can be identified using the present technique, provided of course, that the cell is behaving reliably at the corresponding ranges of oxygen potentials.

To make sure that the cell gave correct results, the following precautions were taken:

a) The alundum cement sealing the reference electrode compartment, was applied in two layers. After the first layer was relatively dry, the second was applied in order to eliminate the existence of any continuous porosity connecting the furnace atmosphere with the Cr/Cr_2O_3 reference electrode. After the experiment, the cell was examined for any possible oxidation of the reference electrode, but apart from a very thin oxidation layer on top of the metal/metal oxide mixture formed by reaction with water from the alundum cement, no other oxidation was observed.

b) In order to ensure good contact between the electrolyte and the reference electrode mixture, care was taken in compacting the metal/metal oxide mixture between the two crucibles, i.e. the inner solid electrolyte crucible and the outer alumina crucible. The molten metal of the metal electrode provided excellent contact with the solid electrolyte crucible.

c) The Mo wire lead was placed as close to the electrolyte crucible as possible in order to eliminate any oxygen activity gradient without the reference electrode. In the metal electrode, stirred by the gas jet impinging to the metal surface, and by vertical movement of the cermet. Measurements taken with the cermet in different positions in the melt, did not show any appreciable difference in the EMF.

d) To test whether the furnace current was having any effect on the measured EMF, measurements were taken with the furnace on and off, but there was no measurable difference in the values of the EMF.

e) The temperature gradient effect is believed to be insignificant. The crucible is small and it is placed in the hot zone of the furnace where the temperature variation is not more than ±2°C.

Moreover, for the reactions studied, dE/dT is almost zero i.e. the entropy change in the cell reaction is small, as can be seen from the values of the EMF plateaus, recorded at different temperatures.

f) To ensure that no polarisation was taking place, a small current was passed in both directions in some of the runs during the plateau. The EMF subsequently stabilised to the original value. (See experimental runs in previous chapter.) For the Fe-Nb-O system, the reversibility of the cell is apparent from the run given in Fig. 4.4, where the plateau appeared at essentially the same EMF during oxidation and during reduction. The gas flow rate was also changed during the plateau period, but no effect on the measured EMF was observed.

g) The electrolyte crucible was examined after the experiment, to see whether there was any chemical attack by the reference or metal electrodes. While such an attack was minimal in cases where the cell was quenched before failing, considerable attack, mainly by the reference electrode, was observed in cases where the experiment was stopped because of cell failure.

In using $Mo|MoO_2$ as reference electrode, attack was rapid and a shiny metallic layer could be observed in the outer side of the electrolyte crucible. This is believed to be caused by the reduction of MoO_2 by chemical reaction between the reference electrode and metal of low oxygen potential in the metal electrode, through cracks in the electrolyte. Although $Mo|MoO_2$ has been suggested for use as reference electrode, because it shows better reversibility than Cr/Cr_2O_3, it gave unsatisfactory results in experiments with the present technique. Cr/Cr_2O_3 worked very satisfac-

torily for EMFs greater than 30-35 mV, i.e. for values of $\log h_O$ in the metal electrode greater than -2.40 at 1600°C. ($P_{O_2} > 2.3 \times 10^{-12}$ atm). For EMFs lower than 30-35 mV, the readings were unstable, indicating non reversible behaviour. Obviously the lower limit in oxygen potential was not set by the properties of the Cr/Cr_2O_3 mixture, but by the limit for purely ionic conduction in the electrolyte. It appeared that as long as the metal electrode did not have a very low oxygen potential, the electrolyte behaved reliably, even though, the Cr/Cr_2O_3 compartment had a lower P_{O_2} equilibrium pressure (9.77×10^{-13} atm at 1600°C).

The use of ThO_2-Y_2O_3 solid electrolyte crucibles would enable determination to be made at lower oxygen potentials and study reactions between lower oxide phases (see section 5.4). ThO_2-Y_2O_3 crucibles were purchased from ZIRCOA for this purpose.

While a few of them passed the usual tests before use (leak testing, metallographic examination and bulk density measurements), no successful runs could be carried out, as they failed under the experimental conditions.

Thus, only calcia stabilised zirconia crucibles were successfully used, and hence the lower limit in oxygen partial pressure in equilibrium with the melts in this study, was around 10^{-12} atm.

Consequently, reactions with lower oxides of the deoxidising metals used could not be studied.

Apte[7] managed to study transition points between lower oxides in the Fe-V-O and Fe-Cr-O systems because these reactions take place under oxygen potentials within the range of the solid electrolyte used.

5.3 Levels of uncertainty

The uncertainties in the present study have two sources of origin, namely the experimental errors and uncertainties in the activity of oxygen in the reference electrode.

The two independently measured quantities in this study are the temperature and the cell EMF. Uncertainty in temperature measurements would be realistically set to ±5°C as there is a variation of ±2°C in the hot furnace zone, and also an error in thermocouple measurements of ±3°C.

Uncertainty in the EMF measurement could be set at ±2 mV, ±0.5 mV due to the potentiometer measurement and ±1.5 mV due to the maximum scatter in the recorded plateau EMF.

These combined errors lead to an uncertainty in the cell reaction, of the order of ±200 cal/g atom of oxygen. The uncertainty in the values reported by Jeannin et al[171] for the free energy of formation of Cr_2O_3 has been estimated to ±200 cal/mole O_2. Hence, for the transition point reactions, the combined uncertainty is of the order of ±300 cal/g atom of oxygen.

In Figures 4.6, 4.15 and 4.25 the error bars given are based on this uncertainty. In view of the internal

consistency of the results it can be said that the uncertainty discussed above is actually overestimated.

5.4 The Fe-Nb-O system

a) Thermodynamic data.

The results in this system have been presented in section 4.3.

According to the discussion in section 5.3 the uncertainty for the ΔG°_{T} values for reaction 4.7 is of the order of ±600 cal/mole $FeNb_2O_6$.

The precision of the data obtained in this study is very high as it can be deduced from the excellent fit with the linear relationship shown in Fig. 4.6. The result obtained using $Mo|MoO_2$ as a reference electrode does not agree very well with the rest of the data. Even though this result was not considered in the least squares analysis, it represents the only "successful" experimental run with $Mo|MoO_2$ as a reference electrode. It is believed, however, especially in view of the different tests carried out on the rest of the experiments to check reversibility, that the data obtained using Cr/Cr_2O_3 as a reference electrode are more reliable.

It should be noted, that because of the narrow range of the experimental temperature, the accuracy that can be attributed to the recorded temperature variation is not high (equation 4.9 and 4.11). It is the values of $\log h_O$ or ΔG°_{T} for the reaction (4.7), rather than their temperature dependence, that should be considered.

Experiments at higher temperatures were not possible because of the rapid failure of the CSZ crucible. Because of this narrow temperature range and the small number of successful experimental runs, the significance of statistical analysis of the data would be limited. A third law analysis would certainly give a better indication of the temperature variation, but it could not be performed because there are no data concerning the Gibbs' energy functions for $FeNb_2O_6$ in the literature.

Comparison of the present data for the reaction (4.7) with other studies in the literature, is not easy as most of the investigators identified only NbO_2 as a deoxidation product and consequently they present data only for the reaction:

$$NbO_{2(s)} \rightleftarrows \underline{Nb}_{\text{lw/o}} + 2\underline{O}_{\text{lw/o}} \qquad (2.54)$$

Although the transition point between NbO_2 and $FeNb_2O_6$ studied here, is the intercept for the lines representing $\log[h_{Nb}^2 h_O^6]$ and $\log[h_{Nb} h_O^2]$ (Fig. 2.1), nothing can be said about the two individual equilibria without a knowledge of h_{Nb}. Since the purpose of the present investigation was to define only the transition point, determinations of h_{Nb} were not attempted. However, Narita and Koyama[101] have studied reactions (2.54) and (2.58). Therefore a comparison was made between their data for the transition point, as obtained by combining their expressions for the equilibrium constants for reactions (2.54) and (4.7), and the results of the present work. The resulting equation was presented in the previous chapter

(Eqn. 4.13) and is shown in Fig. 4.7 with results from the present study. The temperature variation of this study is almost identical to the one presented by Narita and Koyama. This is evidence that, in spite of the narrow temperature range of this study, the correct temperature dependence was obtained. However, as Narita's study was only done in the temperature range 1550°C - 1650°C, no definite conclusions can be drawn.

The almost constant difference of 1.6 Kcal in ΔG°_{T} for reaction (4.7) cannot be accounted for by the uncertainties in the present work. A higher error must exist in Narita's and Koyama's study as can be seen in the scatter of their results[101]. Moreover, their method is inherently less accurate than the present technique, as it involves equilibration and chemical analysis, techniques involving relatively high uncertainties. However, the agreement is still very good. If we use the expression for the equilibrium constant given by the same authors for the reaction (2.58), and combine it with the present data for the transition point (reaction 4.7), an expression for the equilibrium constant for reaction (2.54) is obtained:

$$\log K_{(2.54)} = -\frac{32580}{T} + 13.72 \qquad (5.1)$$

At 1600°C, $K_{(2.54)} = 2.1 \times 10^{-4}$.

This value, which incorporates errors from both the present as well as Narita's and Koyama's studies, is however in good agreement with values reported by different investigators (see Table 2.2).

b) The transition point between NbO-NbO_2

An attempt was made to study the transition point between NbO and NbO_2 in liquid iron. The reaction taking place is:

$$NbO_{2(s)} \rightleftarrows NbO_{(s)} + \underline{O}_{1w/o} \qquad (5.2)$$

If the equation given by Ignatovicz and Davies[109] for the free energy of formation of NbO is combined with equations (2.21), (2.49) and (2.53), ΔG°_T for the reaction:

$$NbO_{(s)} \rightleftarrows \underline{Nb}_{1w/o} + \underline{O}_{1w/o} \qquad (5.3)$$

can be obtained:

$$\Delta G^\circ_{T(5.3)} = 71230 - 33.72\ T \text{ cal} \qquad (5.4)$$

and

$$\log K_{(5.3)} = -\frac{15570}{T} + 7.37 \qquad (5.5)$$

Combination of equation (5.5) with equation (2.55) given by ref. (99) gives ΔG°_T for the reaction (5.2):

$$\Delta G^\circ_{T(5.2)} = 60370 - 20.38\ T \text{ cal} \qquad (5.6)$$

and

$$\log K_{(5.2)} = -\frac{13200}{T} + 4.45 \qquad (5.7)$$

At 1600°C:

$$\log K_{(5.2)} = \log h_O = -2.60$$

After substitution of the expression (5.7), for $\log h_O$ at the transition point between $NbO_{(s)}$ and $NbO_{2(s)}$, into equation (4.5) an expression of EMF versus T using Cr/Cr_2O_3 as a reference electrode, can be obtained:

$$E_{(mV)} = 9.92 - 6.94 \times 10^{-3}\ T \qquad (5.8)$$

At 1600°C:

$$E_{(mV)} = -3\ mV$$

According to our discussion in section (5.2), calcia stabilised zirconia does not behave purely ionically at such a low oxygen activity in the metal electrode. Obviously equation (5.6) involves a high uncertainty, as it is obtained by combining five different sets of data, each one of them adding to the uncertainty level. It is however an indication of the cell EMF expected for the transition point between NbO and NbO_2.

In this study some experiments were performed to determine whether a plateau exists for the reaction (5.2) within the purely ionic range of the CSZ electrolyte. Although there was evidence of a plateau at 20 mV at 1567°C, the measurements were not conclusive as the cell performed irreversibly and the EMF values recorded were unsteady.

It is therefore concluded that ThO_2-Y_2O_3 electrolytes are necessary for a study of reaction (5.2).

c) The morphology of the reaction products

The shape of the inclusions in the Fe-Nb-O system, Fig. 4.8 and 4.9, suggests the existence of numerous small solid particles that agglomerated to form spheres. In a recent publication by Kawawa et al.[172] similar shapes were observed in the case of a rapidly cooled steel ingot.

It appears that the deoxidation products grow initially by diffusion and subsequently by collision during flotation in the melt. Although Turkdogan[21] suggests that a collision mechanism cannot be very efficient, i.e. not many collisions occur between the deoxidation particles during flotation, in the present case, it seems that collision is a major mechanism in inclusion growth. It should be mentioned here that the photographs shown were obtained from a well stirred melt which was quenched from the transition plateau. Thus the condition for collision between small deoxidation particles could have been favorable.

The filaments which are present with the spherical inclusions, do not appear to have been solid during the course of the experiment. Although they could not be analysed due to their small diameter, it is believed that they are secondary products formed during solidification.

5.5 The Fe-Al-O system

a) Thermodynamic data

The results of studying the transition point between Al_2O_3 and $FeAl_2O_4$ are given in section 4.4.

Remarks concerning the precision of results in the system Fe-Nb-O, also apply here. The excellent internal agreement of the results can be seen in Fig. 4.15.

Although the temperature dependence of the derived equations (4.18) and (4.19) cannot be considered to be accurate because of the narrow experimental temperature range, there is good supporting evidence that this dependence

does not substantially differ from the true value.

Third law analysis gives an equation for $\Delta G^{\circ}_{T(4.17)}$ which is very close to that derived from the least square analysis of the experimental results (Fig. 4.17). Moreover, the results of the present investigation, are almost coincident with those of Chan et al.[134] and Kim and McLean[173], and lie in between the results obtained by McLean and Ward[133] and Pillay et al.[132] Once again the agreement is very good. The coincidence of the present results with those presented by Chan et al.[134] is a strong indication that electrochemical studies give more reproducible results than conventional studies.

The expression derived for ΔG°_{T} for the reaction (2.92), equation 4.29, obviously incorporates the errors of the present technique as well as the errors involved in Ghosh's[111] study. However, it can be considered as a realistic estimation of the true value of ΔG°_{T} for hercynite in liquid iron in view of the accuracy of the present study, and also because the determination by Ghosh[111] of the free energy of formation of Al_2O_3, is considered to be accurate. Ghosh himself gives convincing evidence supporting his data and a detailed discussion will not be given here. Speaking in brief, one can only mention the internal consistency of his results, the inherent accuracy of his technique and the independent confirmation of his results from mineralogical studies.

Again the temperature dependence of ΔG°_{T} for reaction (4.28) cannot be considered to be accurate, because of the narrow range of experimental temperatures. The value of ΔH°_{298} for the reaction (4.17) determined by the present study (71730 cal/mole $FeAl_2O_4$) is 2.3 Kcal lower than that calculated from JANAF[141] tables and Barin and Knacke[108] (74±1.5 Kcal/mole $FeAl_2O_4$).

In ref.(140), a value of 73.2±1.3 Kcal/mole $FeAl_2O_4$ is reported which is in reasonable agreement with the present value. However, considering the accuracy of the present technique and the excellent agreement of the present results with other investigators, the present value of ΔH°_{298} = 71730 cal/mole $FeAl_2O_4$ could be considered as the most reliable.

b) The deoxidation products

The deoxidation products of the Fe-Al-O system are shown in Figures 4.19 and 4.20.

The alumina clusters mentioned by Turkdogan[21] and other workers were also observed in the present study.

In the same pictures, some more compact inclusions can be seen. They are similar to the ones reported as spinels by McLean[1] and they are considered to be hercynite inclusions.

In contrast to the Fe-Nb-O inclusions, they are not spherical and they do not indicate that collision between particles is a major mechanism of inclusion growth. Apart from the difference in surface properties of the inclusions

themselves, this could partly be attributed to the fact that they were extracted from an Fe-Al-O melt less well stirred than these in the Fe-Nb-O system.

5.6 The Fe-Al-Mn-O system

a) Thermodynamic and structural considerations.

The results of studies in the Fe-Al-Mn-O system are shown in Figures 4.21 to 4.25.

As was expected, the values of $\log h_O$ for the transition point decrease with decreasing rate, as the Mn content of the melt increases. This is because[150] Mn tends to substitute for Fe in $FeAl_2O_4$ to form a complex spinel $(Fe,Mn)Al_2O_4$. Once all the Fe in the spinel is replaced by Mn to form the spinel galaxite ($MnAl_2O_4$), further additions of Mn will not have any effect on the transition point.

The difference in free energy of formation of FeO and MnO, $\Delta G^\circ_T FeO - \Delta G^\circ_{MnO}$, is approximately 23000 cal/mole at 1550°C. Assuming that the free energy of solution of MnO and FeO into liquid iron and the free energy of formation of hercynite and galaxite from their respective oxides do not substantially differ, it can be predicted that the oxygen activity of the transition point between Al_2O_3 and $MnO.Al_2O_3$ is around 10^{-4} at 1550°C, ($\log h_O \approx -4.0$). Under these circumstances, calcia stabilised zirconia is not suitable as a solid electrolyte, and ThO_2-Y_2O_3 should be used to study reactions in iron melts of such a low oxygen activity.

Following arguments presented by McLean et al.[1,150]

the iron-manganese-aluminate equilibrium in melts containing oxygen and aluminum, should always be represented by a line of slope $=-\frac{2}{4}$ in a diagram of h_O versus h_{Al}. Hence, knowing values of the alumina equilibrium constant and $\log h_O$ for the transition point at different Mn contents, the line representing the equilibrium:

$$(Fe_{1-x}Mn_x)O.Al_2O_{3(s)} \rightleftarrows (1-x)Fe_{(\ell)} + Al_2O_{3(s)} + x\underline{Mn}_{1w/o} + \underline{O}_{1w/o} \qquad (5.9)$$

can be easily constructed in a diagram of $\log h_O$ versus $\log h_{Mn}$.

In Fig. 5.1, such a diagram is presented using the data from the present study. The results are similar to the ones given in ref. (150), but the oxygen activities recorded for the transition point, are somehwat lower for the same manganese content.

As the oxygen content of the melt was actually measured in the work of Kim and McLean[173] and then transformed into oxygen activities using interaction parameters given in the literature, such a difference is understandable due to the large uncertainties in the values of these parameters, particularly that for e_O^{Al}. Thermodynamic considerations can explain the change in the oxygen activity at the transition point with increasing Mn content.

For a system with four components, such as the Fe-Mn-Al-O system, the transition point is no longer a univariant point as in the ternary system. Applying Gibbs'

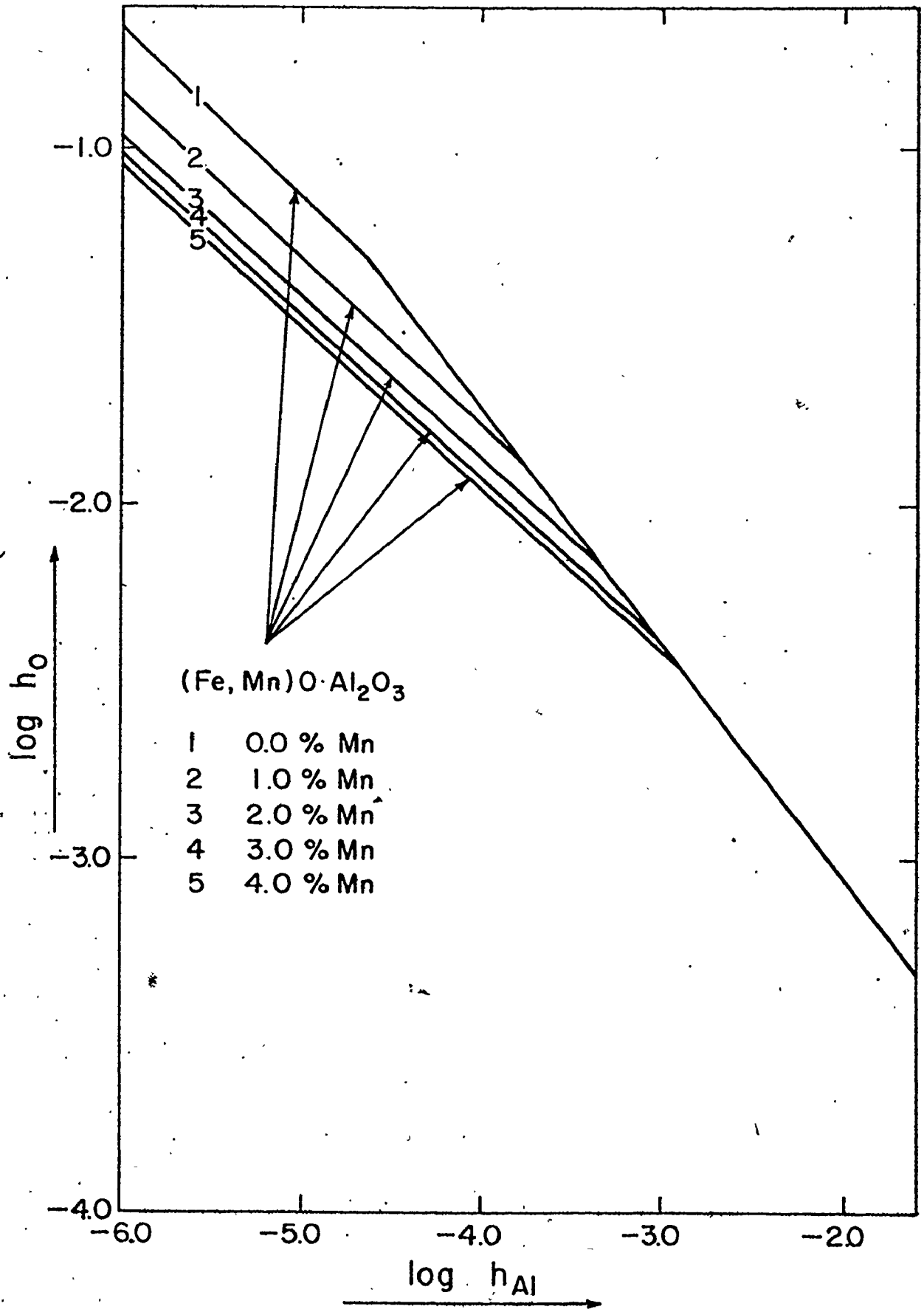

Figure 5,1 Logh_O versus logh_{Al} for the Fe-Al-Mn-O system

phase rule for 4 phases (gas, metal, alumina and complex spinel) in equilibrium, and four components, it can be seen that there are two degrees of freedom. This means that for a fixed temperature, the oxygen activity at which (Fe,Mn)O.Al_2O_3 coexists in equilibrium with Al_2O_3, can depend on the manganese content in the melt. The activity of aluminum at the same point is fixed accordingly. This can easily be seen in Fig. 5.1 and the effect of Mn on the critical aluminum activity is shown in Fig. 4.25.

The structure of $FeAl_2O_4$ is cubic with a_o = 8.119 Å while $MnAl_2O_4$ has also a cubic structure with a_o = 8.258 Å. Hence their X-ray diffraction patterns are almost identical with only a slight displacement of the characteristic lines. The complex oxide $(Fe,Mn)Al_2O_4$ would therefore be expected to have a cubic structure with cell dimensions lying in between those of hercynite and galaxite. It would be also expected that the lattice dimensions would change according to the ratio $\frac{Mn}{Fe+Mn}$ in the spinel. Therefore careful crystallographic examination should reveal the real chemical composition of the complex spinel. In this study, such an examination was not carried out mainly due to limited quantities of the inclusion sample. X-ray patterns taken from surface oxides after magnetic separation, gave lines in between the ones for hercynite and galaxite. This confirms the existence of the complex spinel but it could not possibly be used to determine its chemical composition, because the accuracy required can only be achieved with high precision

techniques, much beyond the scope of this study.

b) Steelmaking considerations

The importance of the study of the Fe-Al-Mn-O system, lies on the fact that the present experimental technique was used to study more complex and therefore more realistic, deoxidation systems.

The experimental results by Kim et al.[150] show that the oxygen concentration in a melt containing aluminum and manganese, remains practically constant for additions of Mn greater than 1.2%. In the present study the oxygen activity of the transition point remains practically constant for Mn contents greater than 3.5%. This can be explained, assuming that almost pure galaxite is produced, and therefore further manganese addition does not substantially affect the equilibrium (5.9).

Manganese increases the deoxidising power of aluminum only when aluminates exist as deoxidation products. If the product is alumina, manganese has no effect in aluminum deoxidation and simply remains in solution.

Another aspect that should be mentioned here is the sequence of deoxidation reactions when aluminum is added as a deoxidiser. For a given manganese content in the melt, iron-manganese aluminates will be formed if the metal oxygen activity is higher than the corresponding transition point. Thus the existence of spinel inclusions at oxygen activities lower than that corresponding to the $FeAl_2O_4$-Al_2O_3 transition, can be explained. Spinel type inclusions are less

readily removed by flotation from steel melts than alumina, and provide a continuous source of oxygen which "buffers" the effect of aluminum increasing the oxygen level substantially above that predicted by thermodynamics.

CHAPTER VI

SUMMARY AND CONCLUSIONS

(1) A new electrochemical technique has been developed to continuously monitor the oxygen activity in molten melts, under oxidising or reducing atmospheres. It basically consists of an oxygen concentration electrochemical cell of the type:

$$Mo|Cr,Cr_2O_3|CSZ|Fe_{(\ell)},\ \underline{O},\underline{M}\ |^{ZrO_2,Mo}_{cermet},Mo \qquad (6.1)$$

where the solid electrolyte is used as a crucible to hold the melt.

The thermodynamic data obtained by this technique are believed to be of high accuracy.

The technique can be used not only to determine the thermodynamics of deoxidation reactions at steelmaking temperatures, but also to reveal the existence of naturally occurring deoxidation products and the conditions governing their transformation to higher or lower oxides.

In this investigation, studies of the Fe-Nb-O, Fe-Al-O and Fe-Al-Mn-O systems have been carried out in the temperature range 1550°C - 1600°C, using the above technique.

(2) In the Fe-Nb-O system, the reaction:

$$FeNb_2O_{6(s)} \rightleftharpoons Fe_{(\ell)} + 2NbO_{2(s)} + \underline{O}_{1w/o} \qquad (6.2)$$

was studied and $\Delta G^\circ_{T(6.2)}$ was determined:

$$\Delta G^\circ_{T(5.6)} = 105870 - 42.64\ T\ (\pm 600)\ \text{cal/mole}_{FeNb_2O_6}$$

$$[1550°C\text{-}1600°C] \qquad (6.3)$$

The deoxidation products NbO_2 and $FeNb_2O_6$ were identified using X-ray diffraction, and their morphology was studied by scanning electron microscopy.

(3) In the Fe-Al-O system, the reaction:

$$FeAl_2O_{4(s)} \rightleftharpoons Fe_{(\ell)} + Al_2O_{3(s)} + \underline{O}_{1w/o} \qquad (6.4)$$

was studied and $\Delta G^\circ_{T(6.4)}$ was determined:

$$\Delta G^\circ_{T(6.4)} = 49910 - 21.50\ T(\pm 300)\ \text{cal/mole}_{FeAl_2O_4}$$

$$[1550°C\text{-}1600°C] \qquad (6.5)$$

Third law analysis was used to give a more accurate temperature dependence of $\Delta G^\circ_{T(6.4)}$:

$$\Delta G^\circ_{T(6.4)} = 46840 - 19.80\ T\ \text{cal/mole}_{FeAl_2O_4} \qquad (6.6)$$

For the experimental temperature range, Eqn. (6.6) is in excellent agreement with Eqn. (6.5).

The deoxidation products Al_2O_3 and $FeAl_2O_4$ were identified and their morphology studied using the same

techniques as in Fe-Nb-O system.

Equation (6.6) was used together with data for alumina formation by Ghosh[111], to calculate ΔG°_{T} for the reaction

$$FeAl_2O_{4(s)} \rightleftarrows Fe_{(\ell)} + 2\underline{Al}_{1w/o} + 4\underline{O}_{1w/o} \qquad (6.7)$$

The resulting equation:

$$\Delta G^{\circ}_{T(6.7)} = 331220 - 115.2T \text{ cal/mole } FeAl_2O_4$$

$$[1540°C\text{-}1600°C] \qquad (6.8)$$

agrees well with previously published data[132-134,173]

(4) In the Fe-Mn-Al-O system, the effect of manganese on the transition point between alumina and iron-manganese aluminates was studied. It was found that increasing the manganese content in the melt decreases the value of $\log h_O$ for the transition point. The reaction at the transition point is:

$$(Fe_{1-x}Mn_x)Al_2O_{4(s)} \rightleftarrows (1-x)Fe_{(\ell)} + x\underline{Mn}_{1w/o} + Al_2O_{3(s)} + \underline{O}_{1w/o} \qquad (6.9)$$

In the present work, the reaction (6.9) was studied for values of x lower than unity because of limitations in the electrochemical cell used.

(5) The main limitation of the present technique is due to the limiting oxygen activity at which calcia stabilised zirconia can perform as a purely ionic conductor. As this

limit is rather high ($\log h_O \simeq -2.40$ at 1600°C), the use of CSZ solid electrolytes is limited in studies in steelmaking.

In the present study equilibria between the oxides $NbO-NbO_2$, $TiO-Ti_2O_3$, $Ti_2O_3-Ti_3O_5$ could not be studied using calcia stabilised zirconia.

Commercial $ThO_2-Y_2O_3$ crucibles did not perform satisfactorily and the manufacture of more reliable $ThO_2-Y_2O_3$ products will therefore enable the extension of the present technique to lower oxygen potentials.

(6) Similar studies of non-ferrous systems are also possible using the present electrochemical technique.

APPENDIX I

Results in the Fe-Ti-O system

a) Experimental

An attempt was made to study some reactions involving titanium oxides in liquid iron.

According to Smellie and Bell[161], the only transition point that could be studied using calcia stabilised zirconia, is the one for the equilibrium between Ti_3O_5 and TiO_2. The transition points corresponding to equilibria between Ti_3O_5 and Ti_2O_3 or Ti_2O_3 and TiO, occur at too low oxygen activities, $\log h_O$ being equal to -2.92 and -5.63 at 1625°C respectively.

The attempt in this study was therefore to establish the thermodynamics of the equilibrium:

$$3TiO_{2(s)} \rightleftarrows Ti_3O_{5(s)} + \underline{O}_{1w/o} \qquad (AI.1)$$

The first successful experimental run is shown in Fig. AI.1. The measurements were taken with the Croydon potentiometer and it appeared that apart from the final plateau, many other plateaus of very small duration occurred at lower oxygen potentials. Hence in subsequent runs, the potentiometric recorder was used to continuously record EMF measurements versus time.

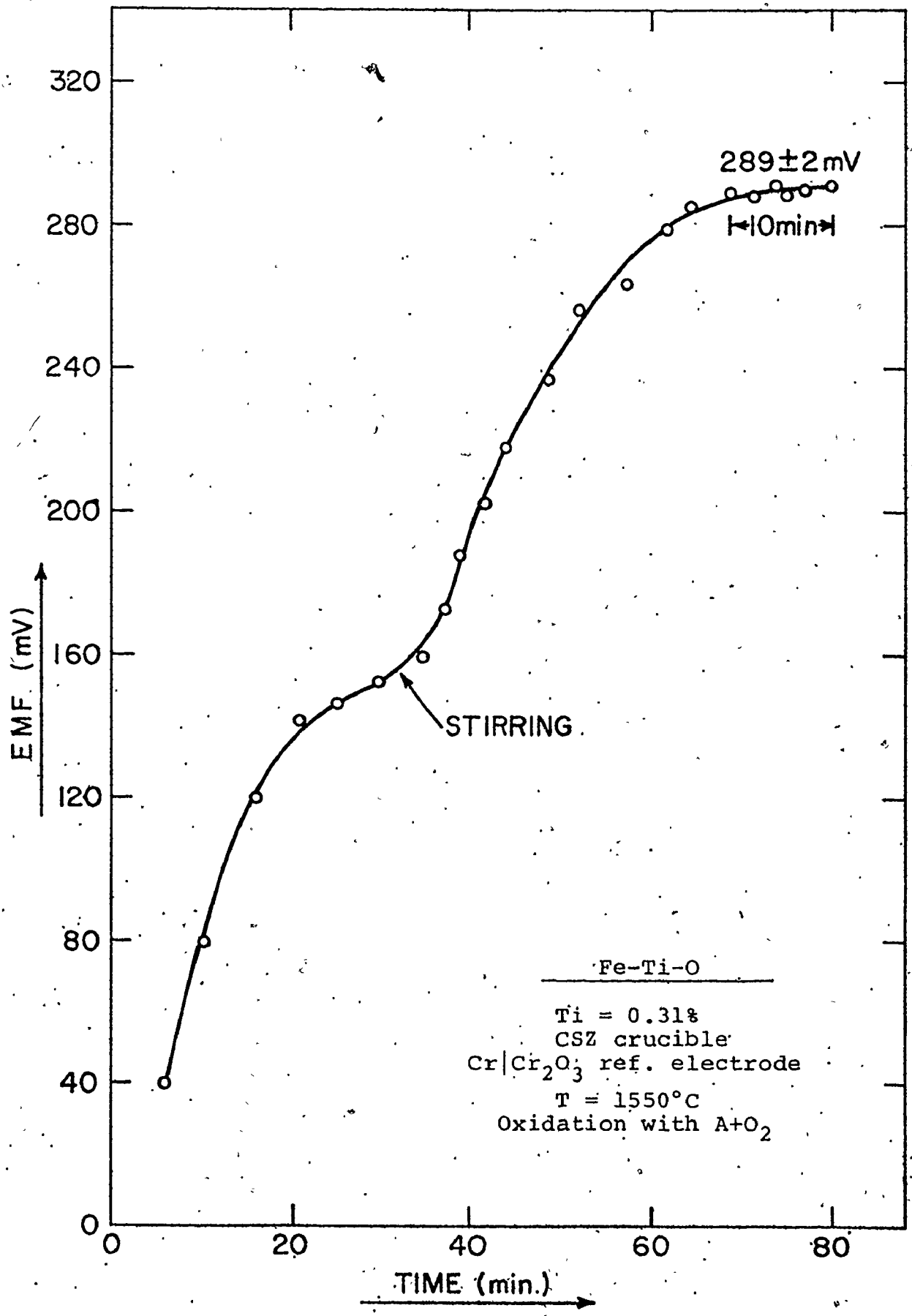

Figure AI.1 Experimental run in the Fe-Ti-O system

A typical graph is shown in Fig. AI.2. The final plateau was always well defined and of a longer duration than those shown in Fig. AI.2.

To make sure that the plateaus were not caused by variations in the oxidising gas flow rate or by a decrease in the oxidation rate due to the creation of a surface oxide layer, the oxidising gas was blown very near to the melt surface at a constant rate. There were no other disturbances of the melt, apart from some occasional vertical movement of the cermet. The plateaus in the EMF vs. time curve, consistently appeared at comparable positions in different runs.

The solid electrolyte crucible always failed at the upper plateau.

In Table AI.1, values of $\log h_O$ for the upper plateaus obtained from different experimental runs, are given. In Table AI.2, values of $\log h_O$ for the plateaus shown in Fig. AI.2 are given. It is apparent that these plateaus occur in a narrow range of oxygen potentials, close to that of the upper plateau. There was evidence of the existence of more plateaus at lower oxygen activities but they are not reported here as they were not as well defined as the ones in Fig. AI.2.

Because of the short duration of these plateaus, no reversibility tests could be carried out. Their consistent appearance in subsequent experiments is the only evidence that they represent a natural phenomenon.

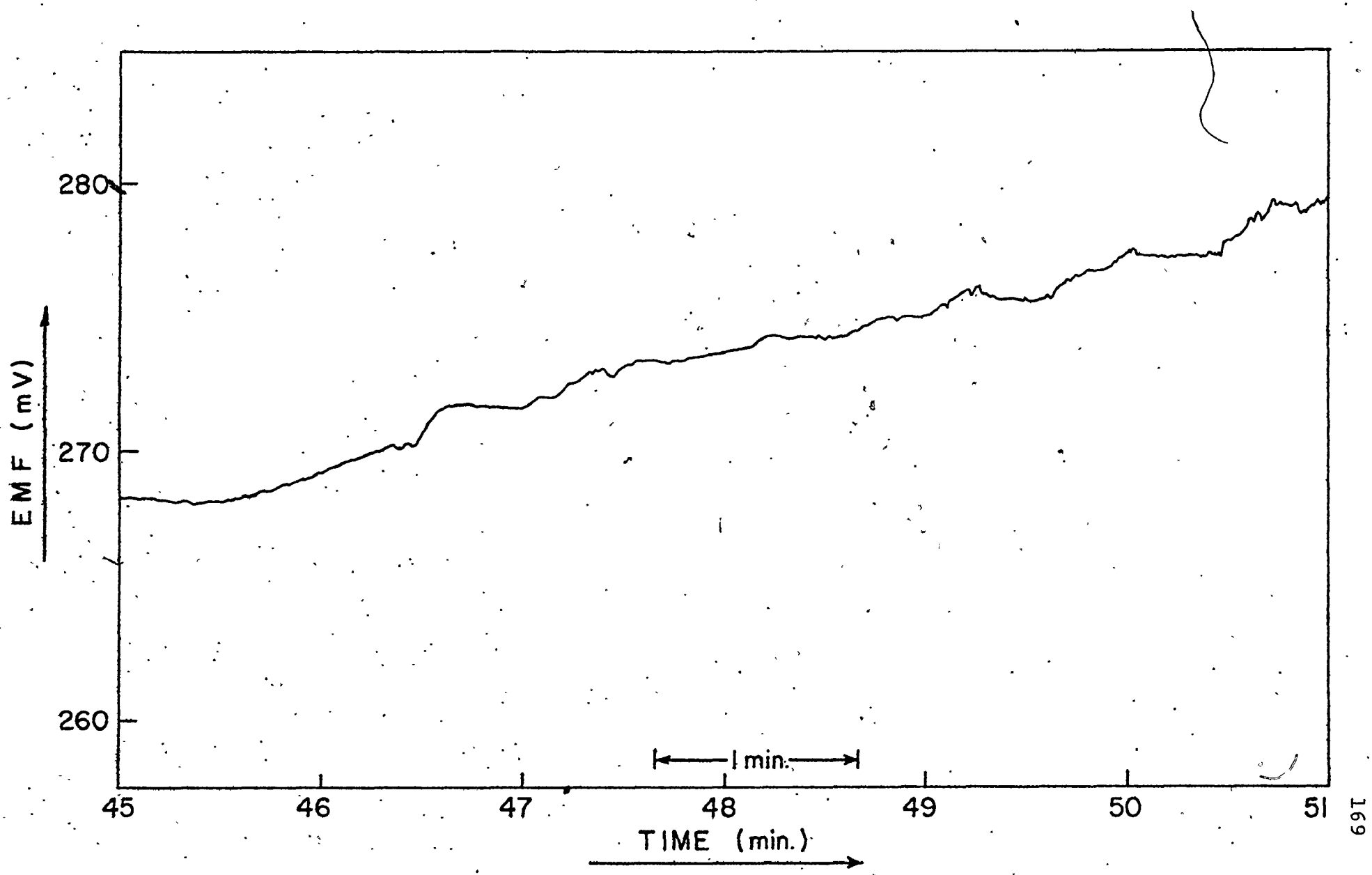

Figure AI.2 Plateaus of short duration in the Fe-Ti-O system

TABLE AI.1

Upper plateaus in the Fe-Ti-O system

T °C	EMF (mV)	Duration (min.)	$\log h_O$	Ti%
1545	281.5	8	-1.24	0.3
1550	262.5	1.5	-1.32	1.0
1550	289	10	-1.23	0.3
1565	287.6	2.5	-1.14	0.3

TABLE AI.2

Intermediate plateaus in the Fe-Ti-O system (Fig.AI.2)

Number	EMF (mV)	Duration (sec)	$\log h_O$	Comments
1	268.0	85	-1.25	
2	272.0	25	-1.22	T = 1565°C
3	273.5	20	-1.22	
4	274.2	25	-1.21	Ti content
5	275.0	15	-1.21	= 0.3%
6	275.7	25	-1.20	
7	277.2	25	-1.20	
8	279.0	20	-1.19	

Once the EMF began to decrease, an indication that the cell had failed, the melt was quenched and the oxide layer on the top of the melt was scraped off for X-ray diffraction analysis as in the previous systems studied. The diffraction patterns did not correspond to either Ti_3O_5 or TiO_2.

b) Possible explanations

One way of explaining the existence of many plateaus is to consider kinetic factors during oxidation in the melt. It might be, that at relatively high oxygen potentials, a non-equilibrium oxide is locally formed, thus hindering further oxidation of the melt. The EMF therefore remains constant for a short time, sufficient for the oxide to dissolve in the melt, the EMF subsequently increasing due to further melt oxidation. This phenomenon is repeated until the final plateau is reached.

Another possible explanation is the formation of Magneli phases in the region between Ti_3O_5-TiO_2 which would result in the appearance of a series of smaller plateaus in the EMF versus time trace.

It is not possible to decide which is the correct explanation of the phenomenon, at the present stage. Evidence in favor of the first explanation, is the fact that subsequent plateaus occur at oxygen potentials higher than those reported for Magneli phases, and the difference in the values of $\log h_O$ for these plateaus is unusually small.

However, the evidence for appearance of similar plateaus at lower potentials could be used to support the second explanation. The plateaus in Fig. AI.2 could be the ones representing the Ti_nO_{2n-1} series of Magneli phases where n is a large number i.e. oxides near the TiO_2 composition. Although in the Ti-O system the value of n for the Ti_nO_{2n} series is reported to vary from 3 to 10, the number of phases stable in the presence of iron could be substantially larger. The upper plateaus reported in Table AI.1, correspond to much lower values of $\log h_O$ than that reported by Smellie and Bell. Indeed, if the evidence of the X-ray diffraction patterns is discarded and the reaction

$$TiO_{2(s)} \rightleftarrows Ti_3O_{5(s)} + \underline{O}_{lw/o} \qquad (AI.1)$$

is considered to take place at the upper plateau, the value of $\Delta G^\circ_{(AI.1)}$ from the present work is about 4 Kcal less than that predicted by Smellie and Bell. It seems unlikely that such a large difference is due to errors, either in the present results or in Smellie and Bell's calculations. It can however, be explained using the following hypothesis:

Let us first assume that in the oxidation of the iron melt from low oxygen potentials, the equilibrium (AI.1) occurs without the existence of any Magneli phases. In Fig. AI.3, this equilibrium occurs at point B, corresponding to h_{O_B}.

Let us now assume that equilibrium (AI.1) does not

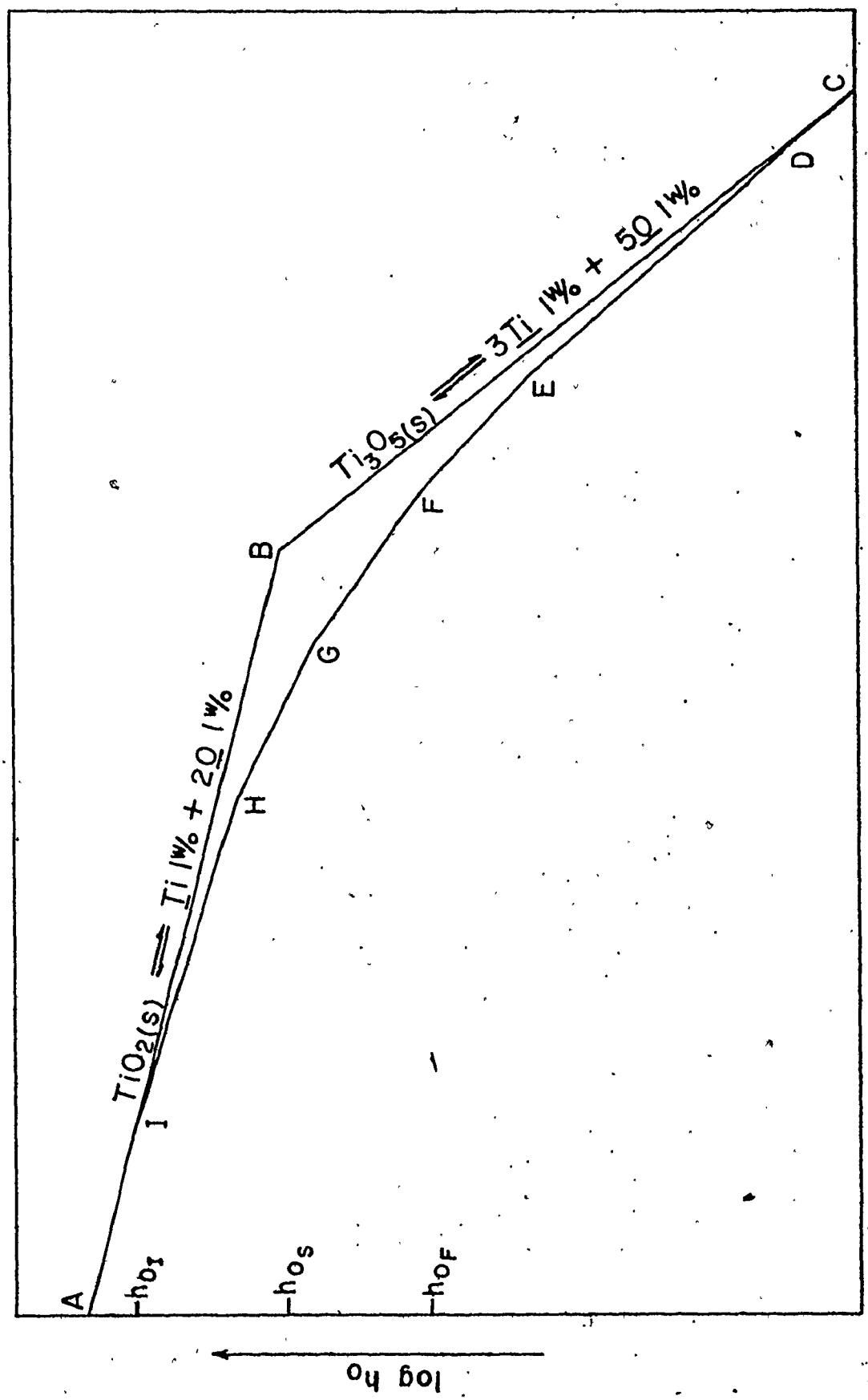

Figure AI.3 Logh_O versus Logh_{Ti} (not to scale)

take place, but that Magneli phases occur, in a series of equilibria of the type:

$$n\ Ti_{(n+1)}\ O_{2(n+1)-1(s)} \rightleftarrows (n+1)Ti_nO_{2n-1(s)} + \underline{O}\ lw/o \qquad (AI.2)$$

These equilibria have to be represented in the same diagram (AI.3), by points such as D,E,F,G,H,I. The number of the points depends on the number of phases occurring. It is obvious that TiO_2 and Ti_3O_5 cannot coexist and also that the oxygen activity over which TiO_2 is stable (h_{O_I}) is much higher than h_{O_B}. It is therefore apparent that the upper plateaus of this study could be intermediate between TiO_2 and Ti_3O_5. The large difference between the values of $\Delta G°$ corresponding to these plateaus and that predicted by Smellie and Bell for equilibrium (AI.1), can easily be explained by assuming that the CSZ crucibles failed at an intermediate oxidation state, possibly at point F. Thus TiO_2 and Ti_3O_5 could not be identified by X-ray examination in samples taken from the upper plateaus of this study.

The fact that the upper plateau was never exceeded in EMF vs. time measurements can be explained by assuming that one of the intermediate phases was detrimental to the CSZ crucible.

The arguments presented above are not conclusive and further research is obviously needed to clarify the observed phenomenon.

REFERENCES

1) A. McLean, J. of Metals 20, (1968) 96

2) A. McLean and R. G. Ward, J. of Metals 17, (1965) 526

3) A. Kontopoulos, Ph.D. Thesis, McMaster University (1971)

4) J. Chipman and M. Dastur, TMS-AIME 191 (1951) 111

5) K. Narita and S. Koyama, Trans. I.S.I.J. 9, (1969) 53

6) A. Vahed, M. Eng. Thesis, McMaster University (1972)

7) P. Apte, Ph.D. Thesis, McMaster University (1977)

8) A. Jacquemont, C. Gatellier and M. Olette, I.R.S.I.D. Re 109-3, January 1975

9) G. K. Sigworth and J. F. Elliott, Metal Science 8, (1974) 298

10) J. Chipman, J. Am. Chem. Soc. 55 (1933) 3131

11) M. G. Fontana and J. Chipman, Trans. ASM 24, (1936) 313

12) J. Chipman and A. M. Samarin, TMS-AIME 125 (1937) 331

13) M. N. Dastur and J. Chipman, TMS-AIME 185 (1949) 441

14) V. V. Averin, A. Y. Polyakov and A. M. Samarin, Izv. Akad. Nauk. SSSR, Otd. Techn. Nauk(Metally) 8 (1955) 90

15) N. A. Gokcen, TMS- AIME 206 (1956) 1558

16) T. P. Floridis and J. Chipman, TMS-AIME 212 (1958) 549

17) E. S. Tankins, N. A. Gokcen and G. R.Belton, TMS-AIME 203 (1964) 820

18) S. Matoba and T. Kuwana, Tetsu-to-Hagane 5 (1965) 187

19) H. Schenck and E. Steinmets, Arch. Eisenhutten.38 (1967) 813

20) J. Chipman, Basic Open Hearth Steelmaking, (G. Derge, Ed.) AIME (Pub.) (1964) 640

21) E. T. Turkdogan, Proceedings of "International Symposium on Metallurgical Chemistry - Applications in ferrous metallurgy" Sheffield (1971) Pub. by I.S.I. London (1973) 153

22) R. J. Fruehan, TMS-AIME 245 (1969) 1215

23) R. J. Fruehan, Metall. Trans. 1, (1970) 2083

24) R. J. Fruehan, Metall. Trans. 1, (1970) 3403

25) J. F. Elliott et al. "Thermochemistry for steelmaking" (I) and (II) 1963, Reading, Addison-Wesley

26) V. W. A. Fischer and D. Janke, Arch. Eisenhutten.42 (1971) 691

27) K. Narita and S. Koyama. Trans. Iron and Steel Inst. of Japan 9, (1969) 52

28) V. H. Schenck, E. Steinmetz and M. Gloz, Archiv. Eisenhutten.39 (1968) 69

29) V. V. Averin and A. M. Samarin, Izv. Akad. Nauk. SSSR, Metallurgia i Toplino 5 (1961) 3

30) G. R. St.Pierre and R. D. Blackburn, TMS-AIME 242 (1968) 2

31) M. Hone, S. Houot and M. Rigaud, Can. Metall. Quarterly 13 (1974) 619

32) P. N. Smith and J. S. Kirkaldy, A. Samarin Memorial Symposium, Academy of Sciences, Moscow (1972)

33) S. E. Feldman and J. S. Kirkaldy, Can. Metall. Quarterly 13 (1974) 625

34) U. Lindborg and K. Torsell, TMS-AIME 242 (1968) 94

35) E. T. Turkdogan, Sulfide Inclusion in Steel, ASM (pub) P.1

36) W. G. Wilson, D.A.R. Kay and A. Vahed, J. of Metals 26 (1974) 14

37) W-K. Lu and A. McLean, Ironmaking and Steelmaking 1 (1974) 228

38) A. Vahed and D.A.R. Kay, Metall. Trans. 7B (1976) 374

39) A. McLean and D.A.R. Kay, Paper presented at Micro-Alloying Conference at Washington, DC, October 1975

40) K. Kuikkola and C. Wagner, J. Electroch. Soc. 104 (1957) 379

41) C. Wagner, Z. Physik. Chem. B21 (1933) 25

42) R. A. Rapp and D. A. Shores, Physiochemical Measurements in Metals Research Vol. IV Part 2 (edited by R. A. Rapp), Interscience Publishers (pub) (1970) 123

43) H. Schmalzried, Z. Electrochem. 66 (1962) 572

44) J. W. Patterson, J. Electrochem. Soc. 118 (1971) 1033

45) W. L. Worrell, Ceramic Bulletin 53 (1974) 425

46) T. H. Etsell and S. N. Flengas, Chemical Reviews 70 (1970) 339

47) H. Ullmann, Z. Phys. Chem. 237 (1968) 274

48) K. Schwerdtfeger, TMS-AIME 293 (1967) 1277

49) R. Baker and J. M. West, J.I.S.I. (1966) 212

50) M. F. Lasker and R. A. Rapp, Z. Physik. Chem. N.F. 49 (1966) 198

51) C. Ilschner-Gench and C. Wagner, J. Electrochem. Soc. 105 (1958) 198

52) G. H. Meier and R. A. Rapp, Study reported at ref [illegible] p.155

53) H. Reinhold, Z.Anorg. Allgem.Chem. 171 (1928) 181

54) L. R. Bidwell, J. Electroch. Soc. 114 (1967) 28

55) R. Taylor and H. Schmalzried, J. Phys. Chem. 66 (1964) 2444

56) Y. D. Tretyakov and H. Schmalzried, Ber. Bunsenges Phys. Chem. 70 (1966) 180

57) R. Benz and C. Wagner, J. Phys. Chem. 65 (1961) 1308

58) T. N. Rezukhina et al., Russ. J. of Phys. Chem. 35 (1961) 671

59) T. N. Rezukhina et al., Russ. J. of Phys. Chem. 37 (1963) 359

60) R. A. Rapp and F. Maak, Acta Met. 10 (1962) 63

61) T. C.Wilder and W. E. Gallin, TMS-AIME 245 (1969) 1287

62) R. J. Fruehan, TMS-AIME 242 (1968) 2007

63) R. Ruka and J. Weissbart, J. Electroch. Soc. 109 (1962) 723

64) H. F. Rizzo et al., J. Electroch. Soc. 116 (1969) 267

65) H. G. Sockel and H. Schmalzried, Ber. Bunsenges Phys. Chem. 72, (1968) 745

66) C. B. Alcock, S. Zador and B.C.H. Steele, Proc. Brit. Ceram. Soc. 8 (1967) 231

67) T. L. Markin, R. J. Bones and V. J. Wheeler, Proc. Brit. Ceram. Soc. 8 (1967) 51

68) S. Mrowec and H. Rickett, Z. Physik Chem. 28 (1961) 422

69) H. Rickett, Werkstaffe und Korrosion 19 (1968) 869

70) H. Rickett, Ber. Bunsenges Physik. Chem. 65 (1961) 463

71) S. Mrowec and H. Rickett, Ber. Bunsenges, Physik.. Chem. 66 (1962) 14

72) H. Schmalzried and C. Wagner, TMS-AIME 227 (1963) 539

73) H. Schmalzried, Arch. Eisenhutten. 39 (1968) 531

74) R. L. Pastorek and R. A. Rapp, TMS-AIME 245 (1969) 1711

75) H. Rickett and R. Steiner, Z. Physik. Chem. N.F. 49 (1966) 9

76) A. Fischer and W. Ackermann, Arch. Eisenhutten. 36 (1965) 643

77) A. Fischer and D. Janke, Arch. Eisenhutten. 40 (1969) 707

78) A. Fischer and D. Janke, Arch. Eisenhutten. 41 (1970) 1027

79) G. R. Fitterer, J. of Metals August (1966) 962

80) G. R. Fitterer, J. of Metals Sept. (1967) 92

81) G. R. Fitterer, C. D. Cassley, V. Vierbicky, J. of Metals June (1968) 74

82) R. J. Fruehan, C. J. Martovik and E. T. Turkdogan, TMS-AIME 245 (1969) 1501

83) P. Catoul et al. C.R.M, No. 35 (1973) 33

84) C. B. Alcock and S. Zador, Can. Metall. Quart. 13 (1974) 321

85) T. A. Ramanarayanan and W. L. Worrell, Can. Metall. Quart. 13 (1974) 325

86) H. W. den Hartog and B. Slangen, Ironmaking and Steelmaking (1976) 64

87) R. C. Garvie, "High Temperature Oxides", Part II Allen M. Alper (Edit.) Academic Press (pub) New York (1970) p.117

88) C. B. Alcock and J. C. Chan, Can. Metall. Quart. 11 (1972) 559

89) P. A. Cerkasor, W. A. Fischer and C. Pieper, Arch. Eisenhutten.42 (1971) 1

90) B. C. H. Steele and C. B. Alcock, TMS-AIME 233 (1965) 1359

91) J. D. Tretyakov and A. Muan, J. Electroch. Soc. 116 (1969) 331

92) J. W. Patterson, E. C. Borgen and R. A. Rapp, J. Electroch. Soc. 114 (1967) 752

93) W. A. Fischer and D. Janke, Arch. Eisenhutten.39 (1968) 89

94) B. C. H. Steele, "Electromotive Force Measurements in High Temperature Systems" C. B. Alcock (Edit) American Elsevier (pub) (1968) 3.

95) J. P. Coughlin, U.S. Bureau of Mines Bull. No. 542 (1954)

96) J. D. Tretyakov and H. Schmalzried, Ber. Bunsenges. Phys. Chem. 69 (1965) 396

97) L. A. Pugliese and G. R. Fitterer, Met. Trans. 1 (1970) 1997

98) R. D. Pehlke, F. N. Mazadavany and R. H. Radzilowski Geochimica and Cosmochimica Acta 39 (1975) 833

99) M. Elle and J. Chipman, TMS-AIME 221 (1961) 701

100) Y. Sato, K. Suzuki, Y. Omori and K. Sonnbongi, Tetsu to Hagane 54 (1968) 330

101) K. Narita, Transactions J.S.I.J. 15 (1975) 145

102) W. A. Fischer and D. Janke, Archiv. Eisenhutten.42 (1971) 695

103) E. B. Teblitsky and L. P. Vladimirov, Izv. A.N. SSSR Metally 4 (1972) 51

104) Z. Buzek, M. Mącoszek and J. Szlauer, Hutn. Listy 27 (1972) 547

105) R. P. Elliot, Constitution of Binary Alloys, First Supplement, McGraw Hill (pub) N.Y. (1965)

106) R. N. Blumenthal, J. B. Moser and D. H. Whitmore, J. of Amer. Cer. Soc. 48 (1965) 617

107) C. E. Wicks and F. E. Block, U.S. Bureau of Mines Bulletin 605, Washington (1963)

108) I. Barin and O. Knacke, Thermochemical Properties of inorganic Substances, Springer-Verlag, Berlin (1973)

109) S. Ignatowicz and M. W. Davies, J. of Less Common Metals 15 (1968) 100

110) W. L. Worrell, Thermodynamics, IAEA, Vienna (1966) (STI/PUB/109) p.131

111) D. Ghosh, Ph.D. Thesis, McMaster University (1975)

112) M. W. Hassenbruch, Rev. Met. 26 (1929) 93

113) C. H. Herty et al. Co-op Bull. no. 46, U.S. Bureau of Mines, Met. Advisory Board and Carnegie Inst. Tech. (1930)

114) H. Wentrup and G. Hieber, Arch. Eisenhutten. 13 (1940) 39

115) D. C. Hilty and W.Crafts, TMS-AIME 188 (1950) 414

116) D. Repetylo et al. J. of Metals, May (1967) 45

117) J. H. Swisher, TMS-AIME 239 (1967) 123

118) N. A. Gocken and J. Chipman TMS-AIME 197 (1953) 173

119) J. C. d'Entremont, D. L. Guernsey and J. Chipman TMS-AIME 245 (1969) 1501

120) W. Geller and K. Dicke, Arch. Eisenhutten. 16 (1943) 431

121) W. Geller, Arch. Eisenhutten. 15 (1942) 479

122) Z. Shibata and T. Yagihashi, Tetsu-to-Hagane 39 (1953) 393

123) A. McLean and H. B. Bell, J.I.S.I. 203 (1965) 123

124) Z. Buzek, Chemical Metallurgy of Iron and Steel, ISI London (pub) (1973) 173

125) H. Schenck et al. Arch. Eisenhutten. 41 (1970) 131

126) L. E. Rohde et al. Arch. Eisenhutten. 42 (1971) 165

127) T. B. Braun et al. as quoted by A. Vahed and D.A.R. Kay Met. Trans. B. 6B (1975) 285

128) J. Chipman and F. C.Langenberg, The Physical Chemistry of Steelmaking, J. F. Elliott (ed.) (1958) 46

129) H. Sawamura et al. Fac. of Eng. Mem 19 207, Kyoto University, Japan (1957)

130) A. Jaquemont et al., C.R. Acad. Sc. Paris 277 (1973) Sec. C 271

131) H. Schmalzried, Z. Phys. Chem. 38 (1963) 87

132) T.C.M. Pillay et al. J. of Amer. Cer. Soc. 43 (1960) 583

133) A. McLean and R. G. Ward, J.I.S.I. January 1966, 8

134) J. C. Chan et al. Can. Met. Quart. 12 (1973) 439

135) I. A. Novokatsky and B. F. Belov, Izv. Ak. Nauk SSSR Metally 1 (1966) 38

136) W. D. Treadwell and L. Terebesi, Helv. Chim. Acta. 16 (1933) 922

137) J. Chipman, Trans. ASM 30 (1942) 817

138) M. de Kay Thompson "The Total and Free Energies of Formation of the Oxides of Thirty Two Metals" Electroch. Soc. (pub.) N.Y. (1942)

139) F. D. Richardson and J.H.E. Jeffes, J.I.S.I. 160 (1948) 261

140) O. Kubaschewski et al. "Metallurgical Thermochemistry" (4th ed.) Pergamon Press (1967)

141) D. R. Stull and H. Prophet (Ed.) JANAF Thermochemical Tables, (2nd ed.) U.S. Dept. Comm. (1971)

142) J. Chipman, Trans. ASM 22 (1934) 385

143) J. Chipman and T. P. Floridis, Acta Met. 3 (1955) 456

144) R. Hultgren et al. Selected Values of Thermodynamic Properties of Metals and Alloys", Wiley (pub.) N.Y. 1963

145) T. C. Wilder and J. F. Elliott, J. Electrochem. Soc. 107 (1960) 628

146) F. Vachet et al. C. R. Acad. Sc. Paris, 260 (1965) 453

147) F. Woolley and J.F. Elliott, TMS-AIME 239 (1967) 1872

148) G. R. Belton and R. J. Fruehan, TMS-AIME 245 (1969) 113

149) W. Oelsen and G. Heynert, Arch. Eisenhutten. 26 (1955) 567

150) C. K. Kim, A. McLean and I. Murray "Deoxidation Reaction in Silicon Free Aluminum Semi-killed steel" Paper presented at the 15th Annual Conference of Metallurgists of C.I.M. in August 1976, Ottawa, Ont.

151) H. Wentrup and G. Hieber, Arch. Eisenhutten. 13 (1939) 69

152) E. L. Evans and H. A. Sloman, J.I.S.I. 174 (1953) 318

153) R. L. Hadley and G. Derge TMS-AIME 203 (1955) 55

154) B. K. Liaudis and A. M. Samarin, Dok. Ak. Nauk. SSSR 101 (1955) 325

155) J. Chipman, TMS-AIME 218 (1960) 767

156) H. Chino et al. Trans. I.S.I.J. 6 (1960) 107

157) K. Suzuki, Y. Omori and K. Sambongi, Bull. Res. Inst. Min. Dress. Met. Tohoku Univ. 23 (1967) 137

158) C. Gatellier, K. Torsell and M. Olette, C.R.A.S. Paris 266 (1968) 1753

159) Y. Kojima, M. Inouye and J. I. Ohi, Arch. Eisenhutten. 40 (1969) 667

160) W. A. Fisher and D. Janke, Arch. Eisenhutten. 42 (1971) 695

161) A. M. Smellie and H. B. Bell, Can. Met. Quart. 11 (1972) 351

162) K. Suzuki and K. Sanbongi, Tetsu-to-Hagane 58 (1972) 1594

163) R. C. De Vries and R. Roy, Am. Cer. Soc. Bull. 33 (1954) 370

164) H. Nishimura and H. Kimura, J. Japan Inst. Metals 20 (1956) 524

165) P. G. Wahlbeck and D. W. Gilles, J. of Amer. Cer. Soc. 49 (1966) 180

166) I. E. Grey, C. Li and A. F. Reid, J. of Solid St. Chem. 11 (1974) 120

167) S. Asbring and A. Magneli, Acta Cryst. 12 (1959) 575

168) J. Sticher and H. Schmalzried, Report fur Theoretische HuttenKunde und Angewandte Physikalische Chemie der Technischen Universitat Clausthal, May 1975

169) L. A. Bursill and B. G. Hyde Progress in Solid State Chemistry 7 H. Reiss and J. O. McCaldin (Ed.) Pergamon Press (Pub.) London 1972 p.177

170) T. Kitikawa, University of Toronto, Private communication

171) Y. Jeannin, C. Mannerskantz and F. D. Richardson, TMS-AIME 227 (1963) 300

172) T. Kawana et al. Can. Metall. Quart. 15 (1976) 129

173) C. K. Kim and A. McLean, "Metal-Slag-Gas Reactions and Processes" Edited by Z. A. Foroulis and W. W. Smeltzer, New Jersey (1975) p.284